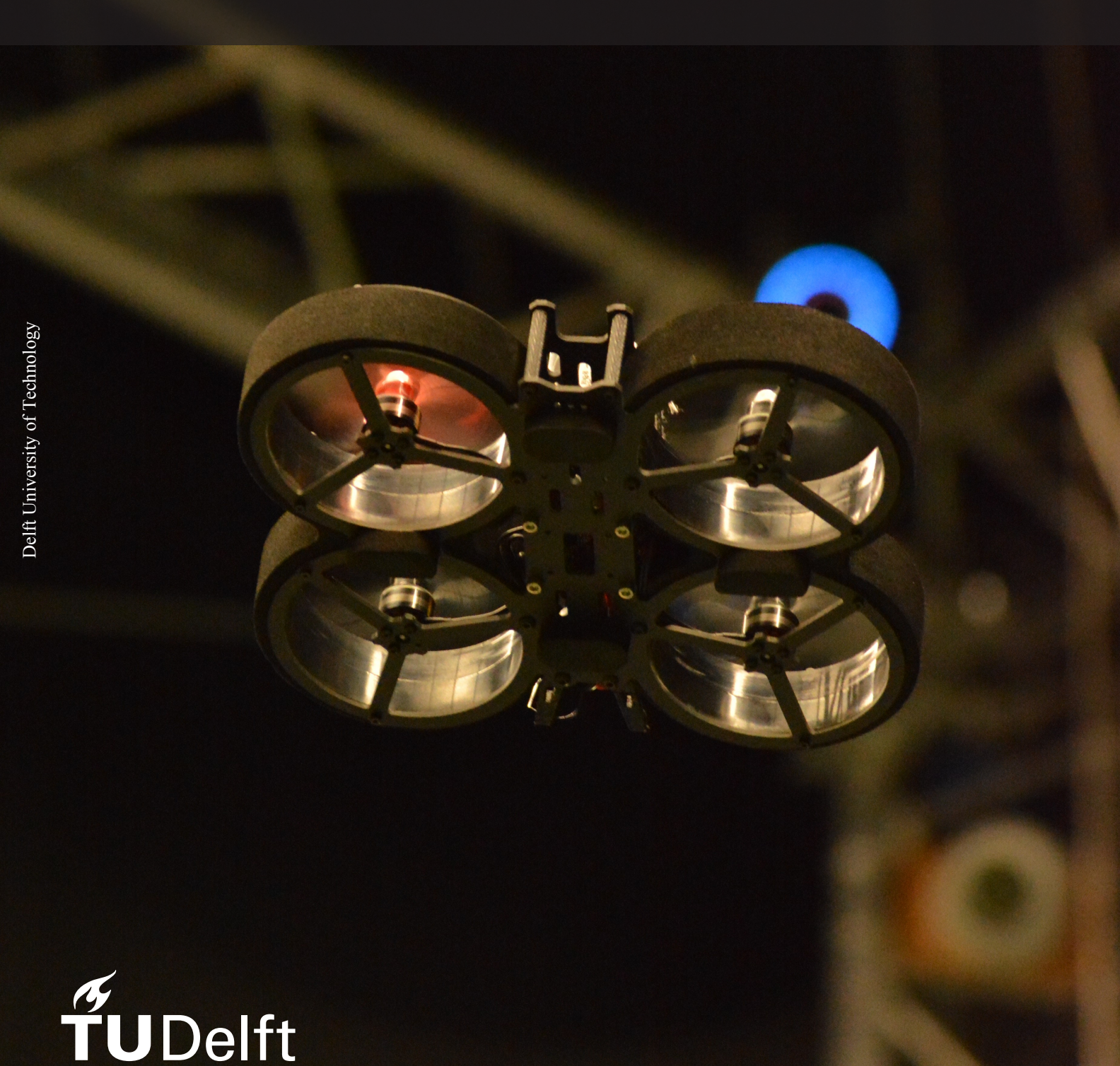
MSc Thesis Report

System Identification of Quadrotors Inflicted with Asymmetric Blade Damage

Burhanuddin Saify





MSc Thesis Report

System Identification of Quadrotors Inflicted with Asymmetric Blade Damage

by

Burhanuddin Saify

to obtain the degree of Master of Science at the Delft University of Technology to be defended publicly on February 8, 2023, at 09:30

Student number: 4669428

Project Duration: 01 February 2022 - 08 February 2023

Thesis committee: Dr.ir. C.C. de Visser TU Delft, Control & Operations

Dr.ir. E.J.J. Smeur TU Delft, Control & Operations

Dr.ir. E. Mooij TU Delft, Space

An electronic version of this dissertation is available at: http://repository.tudelft.nl/.



Acknowledgements

The MSc thesis has been one of the most challenging endeavors of my academic career so far, and it would not have been possible if not for the support of several people. From the early stages of the thesis to its completion, my supervisor, Dr. ir. Coen de Visser provided crucial insights and helped guide me in the right direction when the path seemed murky. Through his positive attitude, I felt motivated to navigate all difficulties, leading to the valuable results of this research.

I would also like to thank my friends and flatmates who helped me take my mind off things when times were stressful. I have thoroughly enjoyed and will cherish the joyous moments we spent together. Finally, I would like to thank my parents, who have helped me tremendously through encouraging words that allowed me to stay positive and persevere.

Contents

I	Introduction	1
II	Scientific Paper	4
Ш	I Preliminary Report	45
1	Introduction	46
2	Quadrotor Dynamic Model2.1 Reference Frames2.2 Dynamic Model2.3 Aerodynamic Effects	48
3	Quadrotor Blade Damage 3.1 Blade Damage Detection 3.2 Fault tolerant control in the presence of blade damage	
4	Safe Flight Envelopes 4.1 Safe Flight Envelope Estimation Techniques	
5	Quadrotor System Identification5.1 Polynomial Models5.2 Advanced Modelling Techniques5.3 State Estimation	61
6	Conclusion and Research Proposal	64
Re	eferences	69
IV	Conclusion and Recommendations	70
\mathbf{V}	Book of Appendices	74
A	Aerodynamic Models	75

Part I Introduction

Introduction

Unmanned aerial vehicles (UAVs) have gained tremendous popularity over the past two decades both in the recreation and commercial sectors. The quadrotor is a particularly popular and versatile UAV configuration that finds several applications. With the ever-increasing prevalence of these vehicles in our airspace, it has become a priority to increase the reliability, and more importantly, the safety of these systems both from a legislative and technological standpoint. With better technology comes safer, and more reliable operability of UAVs, which should further ease legislative burdens which constrain the applications of these platforms.

One important area to focus on when trying to improve the safety of a system is to understand how it performs and behaves in impaired conditions which may impact normal operation, and therefore increase the risk of catastrophic damages to the system and its surroundings. By understanding the behavior of an impaired system, better strategies for controlling the system in this state can be developed that account for the limited capability. However, to understand impaired behavior, a model of the impaired system must be obtained.

In the case of quadrotors, several faults are plausible including, but not limited to, sensor failures, actuator failures, and structural damage. It is reasonable to assume, however, that faults that have the highest impact on performance and safe operability, are those which directly affect the propulsion system, which is simultaneously responsible for maintaining stability and control. Physical damage to the propeller blades is one of the fault scenarios which has received considerable attention in the literature in terms of diagnosis and fault tolerant control, but not from a modeling point of view. Therefore, this gap in the literature was considered an important one to bridge through data-driven modeling of quadrotors subject to physical damage to the propeller blade. Particularly, asymmetric blade damage was considered the more important damage scenario, because the symmetric damage cases often found in the literature do not seem representative of how propellers may be damaged in real-world scenarios.

With the aforementioned motivation, the following research objective was set along with a list of research questions.

"To obtain a dynamic model of a quad-rotor drone with asymmetric blade damage on one or two rotors by conducting system identification experiments through test flights of damaged quadrotors".

- 1. What are the effects of asymmetric blade damage on the dynamic model of a quadrotor?
 - (a) What model structure is required to capture the effects of asymmetric blade damage?
 - (b) Which model terms are most affected by asymmetric blade damage?
- 2. What function approximation method is best suited for modeling the high-frequency dynamic behavior in the presence of asymmetric blade damage?
 - (a) How well does the method allow for interpolating the dynamics at damage levels for which no training data is recorded?
 - (b) Are local non-linearities captured?
- 3. At what extent of asymmetric blade damage do problems caused by excessive vibrations become severe?
 - (a) What auxiliary IMU (with higher measurement ranges) will have to be appended to allow for flights where the standard IMU on the drone becomes saturated?
 - (b) What resonant frequencies of the quadrotor frame inhibit flight with asymmetrically damaged rotor blades?
- 4. Which flight maneuvers should be performed for system identification of a drone with blade damage?
 - (a) How do the maneuvers differ for the identification of aerodynamic models compared to those for the high-frequency phenomena?
 - (b) What are the challenges of covering the flight envelope of the quadrotor in an indoor environment through manual test flights?

5. What insights can be drawn regarding the diagnosis of asymmetric blade damage in quadrotors based on the models identified from experimental data?

The remainder of this report is structured as follows. The main outcomes of the research conducted are presented in the format of a scientific paper in Part II. The preliminary literature review which led to the formulation of the aforementioned research objective and research questions is presented in Part III. Finally, the outcomes of the research are concluded, and recommendations for further research are outlined in Part IV,

Part II Scientific Paper

Modeling Asymmetric Blade Damage in Quadrotors through System Identification Techniques

B. Saify* and Dr.ir. C.C. de Visser †

As quadrotors continue to become more popular for personal and commercial use, improving their safety is essential, especially in impaired operating states. With (asymmetric) blade damage (ABD) being a potentially dangerous type of impairment, it is beneficial to understand how it affects the dynamic behavior of a quadrotor. This research examines the effects of blade damage on the dynamic model of a quadrotor through system identification techniques. Time scale separation is used to split the low-frequency aerodynamic behavior and high-frequency (HF) dynamics. Aerodynamic models are identified using stepwise regression, and a novel approach for modeling HF dynamics –relying purely on on-board sensors– using spectral analysis and simplex B-splines has been developed. A majority of the aerodynamic models surpass \mathbb{R}^2 values of 0.95, and the HF models exceed \mathbb{R}^2 values of 0.90. The findings provide new insights and significant implications for diagnosing ABD in quadrotors.

I. Introduction

QUADROTORS are one of the most popular unmanned aerial vehicle (UAV) configurations in use, owing to their simplicity and versatility [1]. With these systems starting to gain traction in the commercial sector, safe operability has come under scrutiny. This is corroborated by the vast amount of research focused on improving the safety and reliability of these systems. Key areas of research include safe control algorithms in the event of system impairments [2–4], diagnosis of faults [5, 6], aerodynamic modeling [7–9] and safe flight envelope prediction [10].

Several fault scenarios can inflict quadrotors, with actuator faults being one of the most commonly researched due to the high impact of such faults on controllability. Actuator faults in quadrotors are split into two sub-categories; motor failures, and physical damage to the propeller blades. Control of quadrotors subject to complete motor failures has been treated thoroughly [2–4]. The diagnosis of partial losses in rotor effectiveness has also been researched [5, 11, 12]. The latter fault condition is characterized by physical damage to the propeller blades while the motor driving the damaged propeller remains in good health. Physical blade damage has also received considerable attention in the literature both in terms of robust control [13–15], as well as fault diagnosis [16–18].

Physical propeller damage is one of the important modes of structural failure which can adversely affect a quadrotor and is the focus of this paper. Physical damage on a single propeller is divided into two categories; symmetrical and asymmetrical. The former is characterized by equal extent and type of damage to each propeller blade. Naturally, asymmetric damage is characterized by different levels of damage to each propeller blade. It can be argued that asymmetric damage is worth investigating more than symmetric damage purely from the point of view that such a fault condition is more likely to occur, which is also confirmed to some qualitative extent through the experiments of Brown et al. [19].

Several approaches to the diagnosis of (a)symmetric blade damage have been proposed in literature [17, 18, 20–22]. Most of the approaches for diagnosing blade damage rely on data gathered using an Inertial Measurement Unit (IMU) which is a ubiquitous sensor found on quadrotors because it is essential for state estimation and therefore control. The most common approaches to ABD diagnosis involve transforming the time-series IMU data to the frequency domain. This of course makes intuitive sense because the circular –and therefore periodic– motion of the propeller blades results in salient features in the frequency domain. Many methods use features extracted directly from the time domain [18] or frequency domain [17, 23] to train neural-network based classifiers. Notably, Brown et al. [19] thoroughly examine a slew of potential sensors for blade damage diagnosis such as thermal measurements of the electronic speed controllers (ESC), accelerometer measurements, current sensors, and battery voltage to name a few. However, they determine that the accelerometer is one of the best options for ABD diagnosis.

While several papers focus on the diagnosis of ABD, no example was found where the effects of blade damage are modeled through system identification techniques. Neither the effects on the aerodynamics nor the high-frequency

^{*}Graduate student, Faculty of Aerospace Engineering Control&Simulation., TU Delft

[†] Associate Professor, Faculty of Aerospace Engineering Control&Simulation, TU Delft

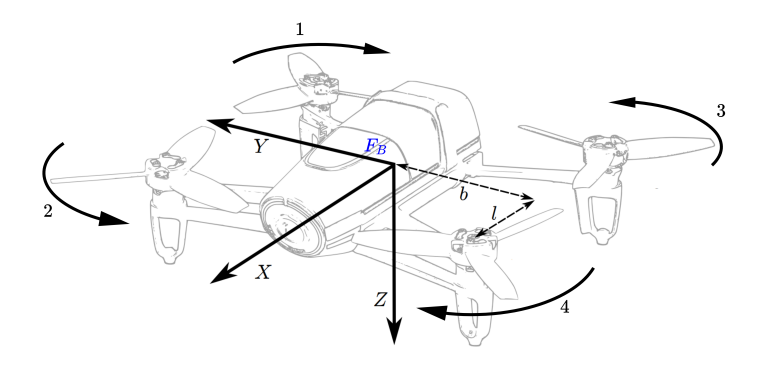


Fig. 1 Representation of a quadrotor body frame and rotation directions of rotors [24]

effects of ABD on quadrotors are thoroughly studied through data-driven analysis. This paper aims to bridge this gap in knowledge. This is achieved by performing experiments with quadrotor platforms subject to ABD at varying levels. Data gathered from these experiments is used to build aerodynamic models and hybrid mass-aerodynamic high-frequency models to capture the effects of ABD. The aim of these models is twofold; for one they allow for accurate simulations and therefore model-based prediction of safe flight envelopes of quadrotors afflicted with blade damage, and to examine the effects of varying locations and levels of blade damage on aerodynamic model parameters as well as the parameters of the models of the high-frequency phenomenon caused by mass and aerodynamic imbalances.

The paper outline is as follows. Fundamentals of the quadrotor platform are introduced in Sec. II, the methodology for experimentation, and modeling are outlined in Sec. III and the results are presented in Sec. IV. Section V provides a discussion of the findings, limitations, and potential of the methodology, followed by a conclusion in Sec. VI.

II. Quadrotor Fundamentals

A. First Principles Model

The kinematics and simplified dynamics of a quadrotor are introduced based on first principles and simple relations for propulsive force and moments. A quadrotor is 6 degree-of-freedom (DOF) system, in that it can control its position and attitude in 3D space. Two reference frames are used when defining the equations of motion of a quadrotor; the inertial frame and the body-fixed reference frame. The inertial frame \mathcal{F}_I is aligned with respect to the Earth such that the xy plane is parallel to the ground, and the xz plane contains the Earth's axis of rotation. The Earth is assumed locally flat and non-rotating (which is quite common for quadrotor analysis) resulting in the inertial frame being chosen arbitrarily as long as the z-axis is perpendicular to, and points into, the ground. The body frame \mathcal{F}_B is defined as depicted in Fig. 1 and is centered at the center of gravity of the quadrotor.

Let $p_I = [x \ y \ z]^T$ and $v_B = [u \ v \ w]^T$ represent the inertial position and body frame velocities of a quadrotor respectively. Similarly, let $q = [\phi \ \theta \ \psi]^T$ and $\omega_B = [p \ q \ r]^T$ represent the attitude of the quadrotor and angular rates in the body frame respectively. Note that the attitude vector q essentially describes the orientation of \mathcal{F}_B with respect to \mathcal{F}_I using Euler angles ϕ , θ , and ψ to represent roll, pitch, and yaw respectively. The matrix R_{IB} describes the transformation from the body frame velocities to the inertial velocities using the Euler angles. Similarly, K_{IB} kinematically relates body angular rates to inertial attitude rates. Constructions for these matrices can be found in [25].

With the aforementioned quantities defined, the equations of motion (EOM) of the quadrotor –split into the linear and rotational EOM– can be formally introduced. Linear motion is described by Eq. (1) and Eq. (2) while rotational motion is described by Eq. (3) and Eq. (4). The terms F_B and M_B represent the external forces and moments acting on the quadrotor in \mathcal{F}_B respectively which are influenced by the effects of gravity, propulsion, and aerodynamics. This simple model excludes the gyroscopic effects of the spinning rotors, and these effects are not included for the remainder of the paper because their contribution was found to be negligible compared to the aerodynamic moments.

$$\dot{p}_I = R_{IB} v_B \tag{1}$$

$$\dot{\mathbf{v}}_B = \frac{1}{m} \mathbf{F}_B + \omega_B \times \mathbf{v}_B \tag{2}$$

$$\dot{q} = K_{IB}\omega_B \tag{3}$$

$$\dot{\omega}_B = I^{-1} \left(M_B - \omega_B \times I \omega_B \right) \tag{4}$$

A simple model is added to the first principles model to account for the thrust force and propulsive control moments created by the 4 rotors. Equation (5) describes the propulsive thrust generated as a result of the rotational speed Ω_i of each rotor, and Eq. (6) describes the propulsive moments on each axis in \mathcal{F}_B as a function of rotor speeds and the geometry of the quadrotor (see Fig. 1 for rotor numbering, rotation direction, and geometrical definitions of parameters l and l). The parameters l0 are the thrust and torque constants of the propeller respectively.

$$\boldsymbol{F}_{B,p} = \begin{bmatrix} 0 \\ 0 \\ -\kappa_0 \sum \Omega_i^2 \end{bmatrix} \tag{5}$$

$$\mathbf{M}_{B,p} = \begin{bmatrix} b\kappa_0((\Omega_1^2 + \Omega_2^2) - (\Omega_3^2 + \Omega_4^2)) \\ l\kappa_0((\Omega_2^2 + \Omega_4^2) - (\Omega_1^2 + \Omega_3^2)) \\ -\tau_0 \sum \Omega_i^2 \operatorname{sign}(\Omega_i) \end{bmatrix}$$
(6)

B. Extensions to the Quadrotor Model

The simple quadrotor model is only applicable around the hovering flight condition and fails to capture quadrotor behavior in high-speed flight. Therefore, it has been extended in the literature by borrowing from helicopter theory [9, 26]. These extensions describe the aerodynamic forces and moments generated by a quadrotor in moderate to high-speed flight. The most important effects are identified to be thrust variance, blade flapping and induced drag [9, 25–28].

Thrust variance describes the dependence of thrust (of a single rotor) on the incoming flow velocity V and angle of attack α of the rotor plane with respect to the incoming flow. The thrust equation can be derived from both momentum theory and blade element theory to yield Eq. 7 and Eq. 8 respectively where A is rotor disk area, a the blade airfoil lift-slope, b the number of blades, c the chord, d the rotor radius, d the propeller rotational speed, and d the blade pitch angle. These relations were used by Sun et al. [7, 29] to inform candidate model regressor choices for quadrotor model identification.

$$T = 2\rho A v_i \sqrt{V^2 + 2V v_i \sin \alpha + v_i^2} \tag{7}$$

$$T = \frac{\rho a b c \omega^2 R^3}{2} \left(\frac{\theta}{3} + \frac{V^2 \cos^2 \alpha \theta}{2\omega^2 R^2} + \frac{V \sin \alpha + v}{2\omega R} \right)$$
 (8)

Blade flapping is another important phenomenon that affects quadrotors in translational flight and is not accounted for by the first principles model. Blade flapping occurs when the velocity field at a blade changes as a function of the azimuth angle of the blade, for example in forward flight where the advancing blade experiences a higher velocity than the retreating blade. The imbalance in the velocity field induces forces that cause the rotor plane, and thus the thrust vector, to tilt such that it is no longer perpendicular to the actuator (motor) axis. This effect has been analyzed thoroughly in helicopter literature [30] and has been adopted to explain quadrotor body forces that occur in the *xy* plane. The tilting of the thrust vector also induces aerodynamic pitching moments depending on how far the c.g. of the quadrotor is from the plane containing the 4 rotors.

The flap angle β of a blade is defined as a function of the azimuth Ψ using Eq. 9 where a_0 is the coning angle a_{1s} and b_{1s} are the tilt angles of the rotor plane orthogonal to, and along the in-plane velocity vector of the rotor. These

angles can be calculated using Eq. 10 and Eq. 11 [27]. The values of parameters A and B are determined by the physical characteristics of the propeller. With the known thrust and tilt of the rotor plane due to flapping, the thrust vector can be projected into the xy body plane of the quadrotor to predict drag forces and resultant moments. In addition to moments caused by in-plane drag-like forces at the rotor, the stiffness of the rotor blades also induces moments directly at the rotor axis. This moment is computed using Eq. 12 [27].

$$\beta = a_0 - a_{1s} \cos \Psi + b_{1s} \sin \Psi \tag{9}$$

$$a_{1s} = \frac{|V_p|}{\Omega R} A_{1c} + \frac{1}{\Omega} B_2 p - \frac{1}{\Omega} B_1 q \tag{10}$$

$$b_{1s} = -\frac{|V_p|}{\Omega R} A_{1s} + \frac{1}{\Omega} B_1 p - \frac{1}{\Omega} B_2 q \tag{11}$$

$$M_{bs} = k_{\beta} a_{1s} \tag{12}$$

III. Modeling Methodology

The presence of ABD is assumed to show effects in two separable frequency regions; the low-frequency region, and the high-frequency region. Damaged propellers experience a loss in thrust capability due to a decrease in blade surface area, which subsequently impacts the dynamic ability of the quadrotor. This loss of thrust affects the low frequency (<60 Hz) dynamic behavior of the quadrotor such as the ability to produce control moments, and accelerations in the z body axis.

The high-frequency effects of asymmetric damage are caused by imbalances in the mass, and aerodynamic forces acting on the damaged propeller. These effects are dominant in the frequency range of the motor rotational speed, which is roughly an order of magnitude higher than the dynamics of the quadrotor as a whole. For example, the hover frequencies of the propellers on the chosen experimental platforms are in the range of 280 Hz to 350 Hz and can go up to 550 Hz at the maximum throttle setting, which is much higher than the cut-off frequency of the slow-speed quadrotor dynamics when no blade damage is present. This assumption is further solidified by Sun et al. [31] who use a cut-off frequency of only 20 Hz for identifying aerodynamic models for a quadrotor comparable in size and mass to the experimental quadrotor platforms used in this research. Using the assumption of time-scale separation, the low-frequency aerodynamic effects, and high-frequency mass-aerodynamic imbalance effects occurring due to ABD are modeled separately.

This section outlines the techniques used to model the aerodynamic models, and high-frequency dynamics models for quadrotors with ABD. The damage cases tested in this research are defined in Sec. III.A. The experimental platforms used for the research are presented, and practical considerations are discussed in Sec. III.B. The methodology utilized to construct the low-frequency aerodynamic models and high-frequency models is explained in Sec. III.C and III.D respectively.

A. Damage Scenarios

1. Damage Case Definitions

Figure 2 shows propellers artificially inflicted with asymmetric damage. The damage is introduced as a straight cut along the blade chord (at each radial location). The damage level is defined as *the missing blade span as a percentage of propeller radius*. Only damage to a single blade was tested. Additionally, both the Beetle and Geyser use the same type of propeller.

Damage scenarios are described with respect to the damage level, and which propeller on the quadrotor is inflicted. The nomenclature 'level' location' is used to describe these damage scenarios. The location is a composition of abbreviations listed in Table 1 while level is the extent of the damage.

The *location* for a damage scenario where a single propeller is damaged is defined by combining the longitudinal location followed by the lateral location. For example, damage to the front-right propeller is defined by location identifier 'FR'. If there are two propellers damaged on the same side, then the location identifier is simply the abbreviation of that side. For example, 'F' would be the identifier for both front propellers being simultaneously damaged.



Fig. 2 Damage cases tested (left to right): Healthy - 10% - 15% - 20% - 25% - 30% - 40%

Table 1 Damage location abbreviations

Damage location	Front	Back	Right	Left
Abbrevitaion	F	В	R	L

The *level* is simply the percentage damage of the propeller(s). For example, 30% damage to the front-right propeller is represented as 30FR, while 30% damage to both front propellers is represented by 30F. It must be noted here that the nomenclature scheme defined here does not account for simultaneous damage to more than two propellers, damage to non-adjacent propeller pairs, or damage scenarios where adjacent propellers have different *levels* of damage. While these damage scenarios are possible, they are qualitatively assumed less likely, especially ones where diagonally opposite propellers are damaged. In addition to reducing the experimental costs, the aforementioned reasons are cited for the choice of tested damage scenarios.

2. Damage Cases Tested

The damage cases covered by the aerodynamic models and HF models of the Beetle quadrotor are listed in Table 2 and 3 respectively. Damage cases with simultaneous damage to two propellers are not covered by the HF models of the Beetle, while they are included in the aerodynamic models. The reason for this is further elaborated on in Sec. V. The aerodynamic models for the various damage cases are constructed both for hovering flights, as well as flights with a mean airspeed of 8 m/s to capture high-speed effects.

Table 4 shows the cases covered by the HF models of the Geyser drone. These cases are much more sparsely covered when compared to the HF models of the Beetle. The reason for this is that the Geyser drone was treated as a secondary platform to apply the HF modeling methodology which gave very good results on the Beetle. The aerodynamic models of the Geyser were not identified because it was only used to test the HF modeling approach and how it generalizes to different quadrotors.

Table 2 Damage scenarios tested for Beetle aerodynamic modeling

20

10

F

FL

BL

BR

10 15 20 25 30 FL FR

Table 3 Damage scenarios tested

for Beetle HF modeling

BL

BR

Table 4 Damage scenarios tested for Geyser HF modeling



B. Experimental Platform and Practical Considerations

30

1. Platform and Facilities

Two quadrotors were used for experimentation shown in Fig. 3a and 3b with their respective code names. These quadrotors are built using off-the-shelf hobby (kits and parts) and use open source flight control software Betaflight *. The inertia properties of the Beetle quadrotor are presented in Table 5. The inertia properties of the Geyser are not

^{*}https://github.com/betaflight/betaflight

Table 5 Inertia properties of the Beetle (including battery)

Mass [kg]	Moment of Inertia [kg m ²]							
	I_{xx}	I_{yy}	I_{zz}					
3.770E-01	8.998E-04	9.158E-04	1.467E-03					

presented because these were not required for HF model identification however they are in the same order of magnitude as the Beetle.

The experimental flights were conducted in the Open Jet Facility[†] and the CyberZoo[‡]. The former is a large low-speed wind tunnel that can produce steady wind at up to 35 [m/s] and features a nozzle with dimensions 2.85 x 2.85 m. The latter is a large caged arena used for testing robotic systems. These facilities are found at the Aerospace Engineering Faculty of the TU Delft. Both facilities feature an optical motion capture (mo-cap) system 'Optitrack' [§] which was used as an external data source to provide accurate measurements of the pose of the quadrotors. Looking at Fig. 3a, the special reflective tape used by the Optitrack system to track the quadrotor can be seen pasted at various locations around the frame.

2. Practical Limitations

One of the key practical limitations was the difficulty to gather the required sensor data. Construction of the aerodynamic models requires high-frequency sampling of the rotational speeds of each of the motors while modeling the high-frequency effects requires high-rate raw (unfiltered) data from the IMU. Betaflight is capable of logging high-rate motor speed data, raw accelerometer data, or raw gyroscope data simultaneously because of the inherent limitations of the firmware. However, concurrent logging of all three of these sources of data is required to simultaneously gather data for low-frequency and high-frequency modeling.

Alternatively to Betaflight, PX4 [¶] was compatible with the flight controllers used in both experimental quadrotors and provided the capability to log all required on-board data simultaneously. However, the motor speeds are measured in PX4 via the telemetry line connecting the ESC to the flight control board unlike Betaflight which uses the more advanced "bidirectional DShot". Therefore, the logging rate of motor speeds in PX4 is limited to 32 Hz while Betaflight can log motor speeds at up to 2 kHz.

Due to the unique data collection limitations of each of the flight firmware, a compromise was made. Data for low-frequency aerodynamic modeling was gathered using Betaflight, while that for high-frequency modeling was gathered using PX4. This is possible because these models are assumed, and observed to be, separable in the frequency domain as was explained earlier. One disadvantage to this approach is of course that double the flights have to be performed, however, this was a manageable limitation.

Another practical limitation comes from the fact that flying with ABD causes severe vibrations which tend to saturate the IMU, and also can cause the motors to fail over time. It was found that blade damage at or above 40% causes enough clipping in the accelerometer, that the attitude estimate gets biased over time, making the quadrotor very difficult to fly in angle mode. Motor failures were also observed to be more frequent at higher than 30% damage for the Beetle quadrotor. For these reasons, the highest used in the experimental flights was 30% for the Beetle, while the Geyser –having a higher mass, and better motors– could be reliably flown at 40% damage.

The clipping in the IMU also means that accelerations of the quadrotor caused by low-frequency aerodynamic forces —which we are trying to model— can not be measured accurately. Even at lower damage levels, where clipping is not present, the filtering of accelerometer data performed by Betaflight results in erroneous spikes in the accelerometer measurements. To resolve this, the pose measurements obtained from the Optitrack system were used to compute the accelerations in the body frame. Due to the exceptional position accuracy of the Optitrack system (< 1mm) and low measurement noise, double time-differentiation of the position measurements using a 2nd order Savitzky-Golay filter [32] gives accurate acceleration estimates. Surprisingly, the accelerations derived from Optitrack position measurements

[†]https://www.tudelft.nl/lr/organisatie/afdelingen/flow-physics-and-technology/facilities/low-speed-wind-tunnels/open-jet-facility

[†]https://tudelftroboticsinstitute.nl/labs/cyber-zoo

[§]https://optitrack.com/

[¶]https://github.com/PX4/PX4-Autopilot





(a) Beetle (b) Geyser

Fig. 3 The quadrotor platforms used for collecting experimental data.

show similar noise performance as IMU measurements. An advantage of using Optitrack-derived accelerations is that no filtering takes place. We however still cannot rely on these acceleration measurements for high-frequency modeling because the sampling frequency of 120 Hz is not nearly as high as the 8 kHz sampling rate of the IMU, and the oscillations in position and attitude resulting from the high-frequency forces and moments result in pose changes which cannot be detected by Optitrack system. Thus, the Optitrack system is used to measure the accelerations which are then used to build the low-frequency aerodynamic models while IMU-derived accelerations are used for modeling the high-frequency behavior.

Unlike the accelerometer, the gyroscope is much more resilient against the vibrations caused by ABD. The limits of the gyroscopes on both the Beetle and Geyser are 2400 o /s, while the oscillations caused by the worst-case vibrations are not more than around 400 deg/s in magnitude. Therefore, the flight controller, and standard PID-based flight control algorithms of Betaflight and PX4 are able to accurately control the angular rates around all three body axes of the quadrotor. The lack of clipping in the gyroscope also meant that the moments acting on the quadrotor body could be recovered directly unlike the accelerations which were derived from the Optitrack pose measurements. The moments M_B acting on the quadrotor are derived using Eq. 4 where $\dot{\omega}_B$ is computed through numerical differentiation of the measured angular rates using a 2^{nd} order Savitzky-Golay filter.

C. Aerodynamic Model Identification with Stepwise Regression

1. State estimation

In order to build accurate models, the states which are used as dependent variables are estimated. This is done using a Extended Kalman Filter (EKF) [33]. As explained in Sec. III.B, the accelerations of the quadrotor are measured using the external mo-cap system because of severe vibration-induced clipping of the on-board accelerometers rendering these measurements unusable. Similarly, velocity is also reconstructed from the Optitrack position measurements. This results in all measurements in terms of linear dynamics (Eq 1 and 2) coming from a single source. This essentially means that the measurements must be taken as ground truth, and no state estimation is performed here. This is assumed reasonable because of the exceptional position measurement performance of the Optitrack system.

Unlike linear accelerations and velocities, the angular rates and attitude can both be measured through independent sources of data. The IMU provides angular rate data, while the attitude is measured with the Optitrack system. These sources of data are fused together using rotational kinematics (Eq. 3). The measurement model for all three attitude angles and angular rates assumes additive white Gaussian noise, the statistics of which were determined through analysis of stationary IMU and Optitrack measurements.

2. Parameter estimation

Aerodynamic models were identified using the stepwise regression (SWR) technique [32] which was earlier used by Sun et al. [29]. A global linear-in-the-parameters polynomial model of the from shown in Eq. 13 is used to model the dependent variable $\mathbf{y} \in \mathbb{R}^n$ as a combinations of regressors $A = \begin{bmatrix} 1 & \boldsymbol{\xi}_1 & \boldsymbol{\xi}_2 & \dots & \boldsymbol{\xi}_p \end{bmatrix} \in \mathbb{R}^{n \times p}$ with model parameters $\boldsymbol{\theta} \in \mathbb{R}^p$ and residuals $\boldsymbol{\epsilon} \in \mathbb{R}^n$. The optimal parameters using an Ordinary Least Squares estimator $\hat{\boldsymbol{\theta}}$ are computed using Eq. 14.

$$y = A\theta + \epsilon \tag{13}$$

$$\hat{\boldsymbol{\theta}} = \left(A^T A \right)^{-1} A^T \mathbf{y} \tag{14}$$

The SWR approach, in addition to determining the optimal model parameters, also determines the set of regressors that best describe the dependent variable. The regressors are added and removed from a pool of regressors in a step-wise manner until a stopping criterion is met. An example of a candidate regressor pool of independent variables x_1 , x_2 , and x_3 to model dependent variable y is shown in Eq. 15 where $P_1^2(x_1, x_3)$ represents all second-order polynomials in x_1 and x_3 and $P_2(x_1, x_2)$ [1 x_3] represent all polynomials in x_1 and x_2 multiplied by 1 or x_3^2

$$y = P_1^2(x_1, x_3) + P_2(x_1, x_2) [1 x_3^2]$$
(15)

The SWR procedure is described next. First, the model is initialised with a bias vector $A = [1 \ 1 \dots 1]^T$. Then, the following algorithmic loop is entered:

- 1) The optimal OLS parameters are estimated using Eq. 14 and the residuals ϵ for this model are computed.
- 2) Each regressor ξ_i in the remaining pool of regressors is made orthogonal to the current model using Eq. 16.

$$\lambda_{i} = \xi_{i} - A \left(A^{T} A \right)^{-1} A^{T} y \tag{16}$$

- 3) The orthogonalized regressor λ_j with the highest correlation to the model residuals is found, and the corresponding regressor ξ_j is added to the model (A), and remove from the candidate pool.
- 4) The model regressors in A are statistically evaluated through an F test. Given q regressors in the current model, the partial F-ratio for the k_{th} regressor is calculated using Equation 17 where s^2 is the variance of the fit error computed using Equation 18 for N data points.

$$F_0 = \frac{SS_R(\hat{\theta}_q) - SS_R(\hat{\theta}_{q-k})}{s^2} \tag{17}$$

$$s^2 = \frac{\epsilon^T \epsilon}{N - q - 1} \tag{18}$$

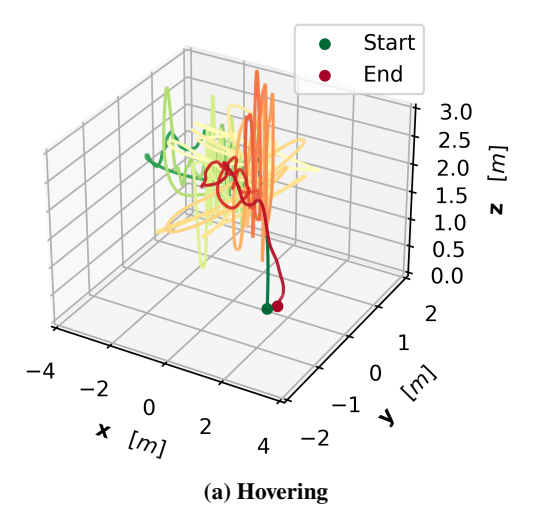
 $SS_R(\hat{\theta}_q)$ is the regression sum of squares for the current model, and $SS_R(\hat{\theta}_{q-k})$ is the same but with regressor ξ_k removed from the model. The SS_R value is computed using Equation 19 where \bar{y} is the mean of the observation vector.

$$SS_R = \hat{\boldsymbol{\theta}}^T A^T \mathbf{y} - N\bar{\mathbf{y}} \tag{19}$$

If the regressor with the smallest F_0 value has an F score below a constant threshold F_{out} , then that regressor is removed. The algorithm stops if the regressor removed was the same as that which was added in that loop. We use an F_{out} threshold of 4 as was done by Sun et al. [7]

5) A stopping criteria based on the Predict Square Error (PSE) (Eq. 20) is used to terminate the algorithm. The first term in this equation is the model residual mean squared error, and the second term penalises model redundancy where *q* is the number of regressors in the current model. Over-fitting leads to an increase in the PSE at which point the SWR algorithm is terminated.

$$PSE = \frac{1}{N} \epsilon^T \epsilon + \sigma_{max}^2 \frac{q}{N}$$
 (20)



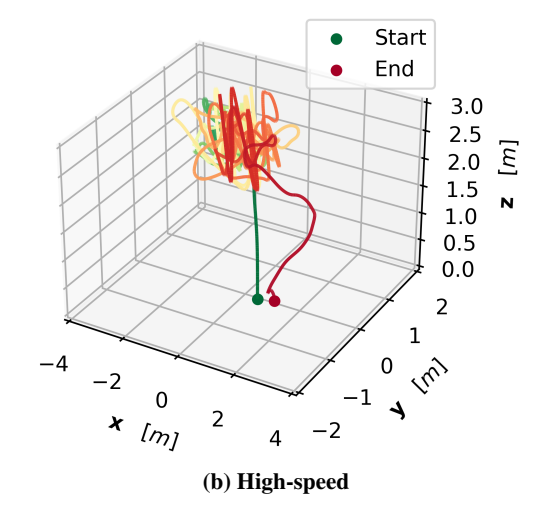
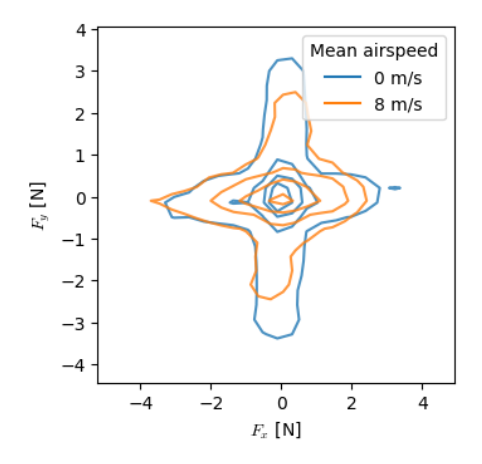


Fig. 6 Example trajectories of system identification test flights for hovering (left) and high-speed flight (right)

3. Flight Test Maneuvers

The system-identification test flights were flown manually. However, to ensure that the data gathered for all damage cases are similar, a set of identical pre-planned maneuvers were flown for each damage case. While the exact flight path followed during each maneuver cannot be kept consistent through this approach, the excitation of all forces and moments can be generated to cover similar envelopes.

The longitudinal flight and lateral flight maneuvers were kept largely separated by design, which means that forces and moments in the x and y body axes were seldom excited simultaneously. This was mainly because of difficulties in flying such maneuvers manually. This results in the '+' shape of the plot showing the kernel density estimates of the distribution of (F_x, F_y) and (M_x, M_y) in Fig. 4 and Fig. 5 respectively.



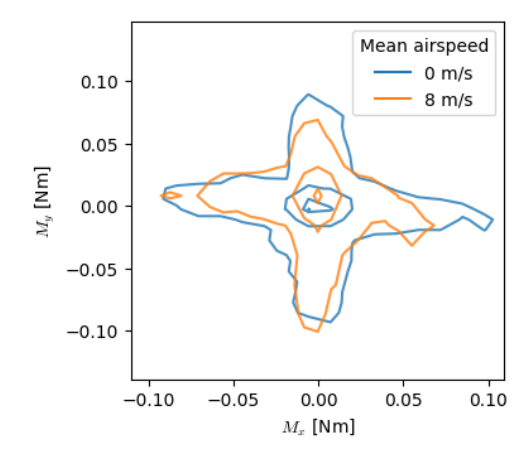


Fig. 4 Kernel density estimates of the force distributions in the xy body plane

Fig. 5 Kernel density estimates of the moment distributions in the xy body plane

Figure 6a and Fig. 6b show examples of the spatial trajectories followed for a flight without wind, and at a wind speed of 8 m/s respectively. The system identification flight maneuvers, consisting of fast pitch, roll, and throttle inputs, as well as slow (sustained) pitch, roll, and throttle inputs, are visible in the figures. While yaw maneuvers were tried for hovering flights, it was difficult to manually excite the yawing moments, which also lead to poor yawing moment models. In high-speed flight, only fast roll maneuvers were possible to execute while staying within the wind stream, and yawing maneuvers were not performed.

4. Model Candidates

With the goal of creating models for all three body forces, and all three body moments using SWR, first a set of candidate regressors is chosen. These sets include various measured states, such as body velocities, angular rates, attitude, as well as control inputs which are derived from measured motor speeds. The choice of candidate regressors is also influenced by the theoretical equations for thrust, and additional effects explained in Sec. II.B. A limit of 3 added regressors was imposed for all models because it was found that after this point, regressors become increasingly complex while offering insignificant improvements to model performance.

$$F_{x} = X_{0} + X_{1}u$$

$$+ P^{3}(u, w) \left[1, \omega_{tot}, q, u_{q}, \sin(\theta), \cos(\theta)\right]$$

$$+ P^{2}(\mu_{x}, \mu_{z}) \left[1, \omega_{tot}, q, u_{q}, \sin(\theta), \cos(\theta)\right]$$

$$+ P^{2}(q) \left[1, \omega_{tot}\right]$$

$$+ P^{2}(u_{q}) \left[1, \sin(\theta), \cos(\theta), \omega_{tot}\right]$$

$$+ P^{2}(\omega_{tot}) \left[\sin(\theta)\right]$$

$$F_{y} = Y_{0} + Y_{1}v$$

$$+ P^{3}(v, w) \left[1, \omega_{tot}, p, u_{p}, \sin(\phi), \cos(\phi)\right]$$

$$+ P^{2}(\mu_{y}, \mu_{z}) \left[1, \omega_{tot}, p, u_{p}, \sin(\phi), \cos(\phi)\right]$$

$$+ P^{2}(p) \left[1, \omega_{tot}\right]$$
(22)

$$F_{z} = Z_{0} + Z_{1}w$$

$$+ P^{3} (|u|, |v|, w) [1, \omega_{tot}, |p|, |q|, |u_{p}|, |u_{q}|]$$

$$+ P^{2} (|\mu_{x}|, |\mu_{y}|, \mu_{z}) [1, \omega_{tot}, |p|, |q|, |u_{p}|, |u_{q}|]$$

$$+ P^{2} (\omega_{tot}) [1]$$

$$+ P^{2} (|p|, |q|, |r|) [1, \omega_{tot}]$$
(23)

Equations 21, 22, and 23 show the model candidate structures for the x, y, and z body axis forces respectively. Equations 24, 25, and 26 show the model candidates for the x, y, and z body moments respectively. Note that coupling between F_x and F_y was largely eliminated while choosing these regressor sets because the flight test maneuvers were largely uncoupled in the longitudinal and lateral directions. The regressor $\omega_t ot$ is defined as the sum of the rotor speeds, and the input roll, pitch, and yaw control moments $-u_p$, u_q and u_r are defined according to the respective axis-specific rotor speed combinations defined in 6. The advance ratios, $\mu_{x,y,z}$, are added to capture the effects of thrust variance as well as blade flapping.

 $+P^{2}(u_{p})[1,\sin(\phi),\cos(\phi),\omega_{tot}]$

 $+P^{2}\left(\omega_{tot}\right)\left[\sin(\phi)\right]$

While the attitude angles are not necessarily a good regressor choice from a physical sense, they are found to improve model performance significantly, likely because these angles encode information about relative flow angles with respect to the rotors of the quadrotor. It is important to point out here that while the chosen model candidates are influenced by analytical models of the underlying physical phenomena, they do not necessarily capture cause-effect relationships, but rather also model correlations that describe reality from a phenomenological perspective. Nevertheless, when applied to quadrotors (and other aerospace systems), these models can still offer a reliable means to make predictions, even if the underlying physics is not exactly captured.

$$M_{x} = L_{0} + L_{1}p + L_{2}u_{p}$$

$$+ P^{3} (|u|, v, w) \left[1, \omega_{tot}, p, |r|, u_{p}, |u_{r}|, \sin(\phi), \cos(\phi) \right]$$

$$+ P^{2} (|\mu_{x}|, \mu_{y}, \mu_{z}) \left[1, \omega_{tot}, p, |r|, u_{p}, |u_{r}|, \sin(\phi), \cos(\phi) \right]$$

$$+ P^{2} (p, |q|, |r|) \left[1, \omega_{tot}, \sin(\phi), \cos(\phi) \right]$$

$$+ P^{2} (u_{p}, |u_{q}|, |u_{r}|) \left[1, \sin(\phi), \cos(\phi), \omega_{tot} \right]$$

$$+ P^{2} (\omega_{tot}) \left[\sin(\phi), \cos(\phi) \right]$$
(24)

$$M_{y} = M_{0} + M_{1}q + M_{2}u_{q}$$

$$+ P^{3}(u, |v|, w) \left[1, \omega_{tot}, q, |r|, u_{q}, |u_{r}|, \sin(\theta), \cos(\theta)\right]$$

$$+ P^{2}(\mu_{x}, |\mu_{y}|, \mu_{z}) \left[1, \omega_{tot}, q, |r|, u_{q}, |u_{r}|, \sin(\theta), \cos(\theta)\right]$$

$$+ P^{2}(|p|, q, |r|) \left[1, \omega_{tot}, \sin(\theta), \cos(\theta)\right]$$

$$+ P^{2}(u_{q}, |u_{p}|, |u_{r}|) \left[1, \sin(\theta), \cos(\theta), \omega_{tot}\right]$$

$$+ P^{2}(\omega_{tot}) \left[\sin(\theta), \cos(\theta)\right]$$
(25)

$$M_{z} = N_{0} + N_{1}r + N_{2}u_{r}$$

$$+ P^{3} (|u|, |v|, w) \left[1, \omega_{tot}, |p|, |q|, |r|, u_{p}, |u_{q}|, |u_{r}|, \sin(\theta), \cos(\theta), \sin(\phi), \cos(\phi) \right]$$

$$+ P^{2} (|\mu_{x}|, |\mu_{y}|, \mu_{z}) \left[1, \omega_{tot}, |p|, |q|, |r|, u_{p}, |u_{q}|, |u_{r}|, \sin(\theta), \cos(\theta), \sin(\phi), \cos(\phi) \right]$$

$$+ P^{2} (|p|, |q|, r) \left[1, \omega_{tot} \right]$$

$$+ P^{2} (|u_{q}|, |u_{p}|, u_{r}) \left[1, \omega_{tot} \right]$$

$$+ P^{2} (\omega_{tot}) \left[\sin(\theta), \cos(\theta), \sin(\phi), \cos(\phi) \right]$$

$$(26)$$

5. Model Simplification

Rather unsurprisingly, SWR often finds a different set of regressors (for each force and moment model) for different damage cases. However, these regressors tend to often be spurious and offer almost insignificant model improvement. Additionally, two regressors that are highly correlated may be picked somewhat randomly from one damage case to another.

To gain a better understanding of the variation of model parameters with the extent of blade damage, simplifications were made to the models found through SWR. In this way, the polynomial models for all damage cases have the same set of regressors, and only the parameter values for these regressors change for different damage cases.

The exact procedure for picking the fixed regressors was largely heuristic. The general rules-of-thumb are; to keep the regressors that appear most commonly for all damage scenarios, offer the most significant model improvements, and are not highly correlated with other regressors. Following these procedures, the models could be simplified without losing too much performance, but allow for better physical insights into how the impact of a given regressor change with blade damage, and if any clear patterns can be found.

D. High-Frequency Model Identification

1. General Approach

The goal of the High-frequency models is to be able to reproduce the IMU signals which are measured by a quadrotor inflicted with ABD. The base assumption used for constructing the high-frequency models is that the time series of each IMU measurement can be modeled as a sum of a few sinusoids. This assumption is physically motivated by the fact that force and moment imbalances created by an asymmetrically damaged propeller will be cyclic in nature, and visual examination of the measured IMU signals also shows that this is the case (see Fig. 21). Therefore, the model structure shown in Eq. 27 was chosen, where k is the number of harmonics of the frequency f, and d_l is the damage level of the propeller. To parameterize this model, the amplitude surface A_n of the n^{th} harmonic is constructed as a function of f and d_l .

$$y(t) = \sum_{n=1}^{k} A_n(f, d_l) \sin(2\pi n f t)$$
 (27)

The amplitude models were built assuming dependence only on the frequency and level of damage. Here, frequency refers to the rotational speed of the damaged propeller in Hz, and corresponding harmonics. This choice of dependent variables is again due to physical reasoning. For one, higher levels of damage result in larger mass imbalances as well as larger asymmetries in the aerodynamic forces and torques generated by the damaged propeller. It is straightforward to see that the mass imbalance of a damaged propeller induces a net centripetal force vector which oscillates in direction at the rotational frequency of the rotor. These forces can be quite high even with small mass imbalances because the

propellers of the quadrotor spin at very fast speeds. A first principles approach would be to model the centripetal forces as scaling with the square of the rotational speed of the propeller, but this ignores various physical interactions which can be captured through data-driven analysis.

A less obvious high-frequency effect comes from the aerodynamic imbalances of the damaged rotor. For example, in the presence of ABD, the thrust force is no longer aligned with the rotational axis of the propeller but is offset from this axis and also rotate around it in sync with the propeller. Due to its movement with respect to the center of gravity of the quadrotor, the thrust imbalance induces oscillatory pitching and rolling moments around the quadrotor c.g. Similar to the imbalance in thrust, there is also an in-plane drag force generated perpendicular to the rotation axis with some offset. The moment arm of this imbalanced drag force also oscillates sinusoidally with respect to the c.g., resulting in oscillatory yawing moments created around the quadrotor c.g. The spinning drag force vector, similar to the centripetal forces due to the mass imbalance, also causes oscillatory forces in the *x* and *y* body axes of the quadrotor.

The forces and moments described earlier do not consider the structural frame of the quadrotor, and how this frame affects the measurements taken at the IMU. The frames of both the Beetle and Geyser quadrotors are largely made of carbon composites, meaning they are quite stiff. However, no structure is infinitely stiff, and therefore as the oscillatory forces and torques of the damaged rotor are transmitted through the frame, they get altered due to structural resonance in the frame. Even the stand-offs which are used to mount the flight controller to the frame of the quadrotor affect the forces before they are measured by the IMU which is soldered on the flight control board. Clearly, there are complex interactions with the structural frame of the quadrotor which are very difficult to model from first principles. However, using a data-driven method, the effects of frame resonance get lumped along with all the other physical interactions which take place in the presence of ABD.

Finally, another kinematic consideration to keep in mind is that the IMU does not lie exactly at the c.g. of the quadrotor. This offset means that the IMU does not measure the accelerations of the c.g. of the drone, but rather the accelerations which are also corrupted by rotational rates and rotational accelerations about the c.g. While this effect can be analytically corrected, there is no good reason to do so. It is again re-emphasized that the goal of the high-frequency models is to accurately inject the lumped effects of oscillatory forces and torques arising due to ABD on the measurements made by the IMU, not to accurately model the forces and torques themselves. These models can then facilitate the accurate reproduction of high-frequency effects in simulations of quadrotors with damaged propellers.

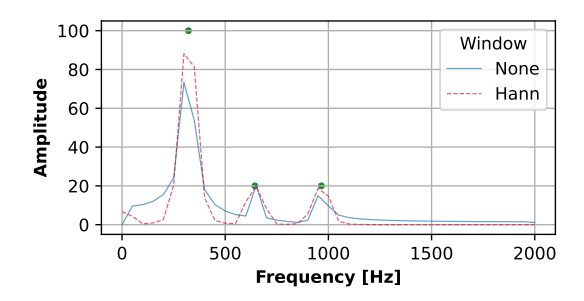
The flight maneuvers flown to sufficiently excite the high-frequency phenomenon described above were chosen with the simple requirement of making sure the damaged propeller goes through a large part of the rotational speed range of the motor. This essentially means that the maneuvers should be flown such that the full throttle range is covered. This proved challenging in an indoor environment because of the restricted space for mobility. This problem was overcome by performing short, yet aggressive successive throttle punches, as well as longer duration throttle pulses with lower maximum throttle input. In addition to the above, aggressive rolling and pitching maneuvers were also performed to again ensure that the damaged propeller covers a large part of the rotational speed range of the motor within a single flight. The cumulative distribution of motor frequencies over all the test flights of the Beetle is shown in Fig. 36.

2. Spectral Analysis

Before identifying a model to predict the amplitudes of sinusoidal oscillations measured by the IMU, the amplitudes and corresponding frequencies must be estimated from the time-series data of each IMU axis. This can also be interpreted as the 'state estimation' step of identifying the high-frequency models.

There are a handful of techniques that can be used to transform signals from the time domain to the frequency domain. However, for this application, some important constraints must be considered while choosing a method. For one, the IMU time series signal generated during a flight will be non-stationary, therefore an evolutionary spectrum must be computed. Another practical constraint is that the sampling times of the IMU are not perfectly constant, which may pose additional challenges. With these constraints, a spectrogram constructed using the short-time Fourier transform (STFT) was used. The SciPy implementation of the STFT was used for the analysis presented in this paper [34]. Even though this technique assumes evenly sampled data, the amount of sampling jitter observed in the experimental data was not severe enough to significantly impact the results. This was also numerically verified by computing STFTs of artificially generated sinusoidal signals with greater amounts of jitter than what was observed in the experimental data. A detailed analysis of the noise and jitter properties of IMU measurements is presented in Appendix A.

Two important parameters of the spectrogram are the window length (n_s) , and the number of samples (n_{fit}) used to compute the STFT at each time slice. The window length, in combination with the sampling frequency f_s , sets the frequency resolution (f_r) of the spectrogram, while (n_{fit}) essentially sets the amount of zero-padding applied to each



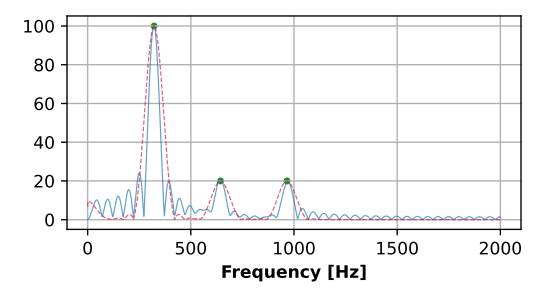


Fig. 7 Comparison of STFT computed without zero padding (left) to that with zero-padding (right) where the circular markers show the true underlying frequencies and associated amplitudes of the time-series signal.

time slice of the signal being analyzed. While zero-padding does not surpass the frequency resolution limit, it does generate more frequency bins in the STFT. The resulting frequencies are no longer orthogonal to each other, however, which means that two sinusoids with frequency separation within the frequency resolution of the STFT cannot be resolved perfectly. The IMU signals are comprised mainly of a few dominant sinusoids which are separated by several multiples of the frequency resolution. Thus, zero-padding allows for better recovery of the properties of the sinusoids comprising the signal compared to the no-zero-padding case.

To visualize the effect of zero padding, a numerical example is shown in Fig. 7. Here, a 0.02 s long signal ($f_r = 50 \text{ Hz}$) with a sampling frequency of 4 kHz (N = 80) and comprising of three pure sinusoids was generated. By zero-padding the signal with $n_{\text{fft}} = 2000$, an effective frequency resolution of 2 Hz is achieved. It is clear from Fig. 7 that applying zero-padding facilitates interpolation between the frequencies corresponding to the true frequency resolution. However, this comes at the cost of spurious peaks caused by the fact that the sin functions at the zero-padded frequencies do not form an orthogonal set. Using a Hann window solves this problem at the expense of broadening the peaks. Fortunately, this is not a problem for the spectral analysis of IMU signals because these are dominated by a base sinusoid with a minimum frequency generally above 100 Hz, and its harmonics have frequency separations greater than or equal to this value.

The values of the parameters n_s and $n_{\rm fft}$ are linked to parameters f_r , f_{r_e} and the sampling frequency f_s through Eq. 28 and 29 respectively. The choice of f_r and f_{r_e} plays a critical role in determining the quality of the STFT. If the f_r is chosen to be small, equating to large time windows, the signal may go through a large change in frequency within the time window resulting in the frequency content being smeared across multiple frequencies. Therefore, the true frequency-amplitude relationship cannot be recovered. Alternatively, a large value for f_r , equating to very short time windows may again be detrimental as there is little information in each window. Since the main factor influencing the choice of these parameters is how fast the dominant frequencies of the signal change with time, a numerical study was conducted (described in detail in Appendix B) which resulted in a choice of 60 Hz for f_r and 2 Hz for f_{r_e} .

$$n_s = \text{floor}\left(\frac{f_s}{f_r}\right) \tag{28}$$

$$n_{\rm fit} = {\rm floor}\left(\frac{f_s}{f_{r_e}}\right)$$
 (29)

Once the spectrogram of a signal is computed, each slice of the spectrogram is analyzed to find the location of the peak frequency, its harmonics, and the respective amplitudes of these harmonics. This procedure results in a data set of frequency-amplitude pairs for all the dominant harmonics of the time signal. Since the base harmonic is expected to be near the measured motor rotational speed, this frequency is found by locating the highest peak within a certain frequency range f_{range} of the motor frequency. The value of f_{range} is set to 25 Hz, which is heuristically set to ensure that a large range of frequency around the motor frequency is checked for peaks. With the frequency of the base harmonic known, the same procedure is repeated for the higher harmonics. Figure 8 shows an example of the spectral analysis described above applied to the raw roll rate measurements obtained from the Geyser drone. Here the motor frequency went from around 160 Hz to above 350 Hz in this span of 0.15 seconds, which is visible in the spectrogram. The detected amplitudes of the base harmonic are shown along with the addition of the amplitudes of the 2^{nd} and 3^{rd} harmonics, which collectively bound the signal fairly accurately. The significance of the 2^{nd} harmonic is also evident

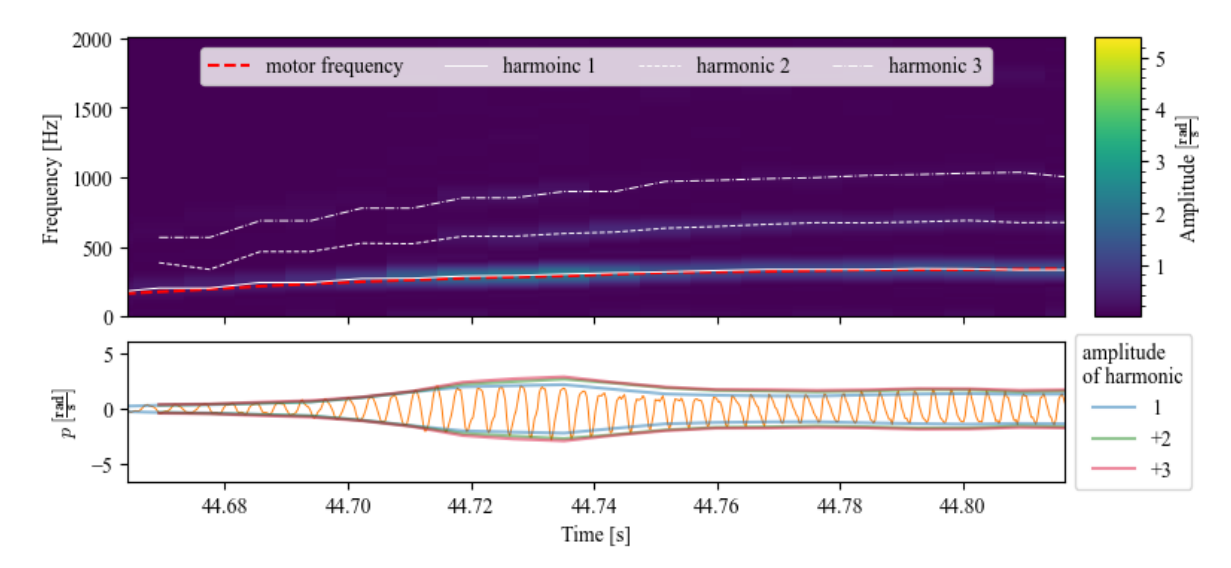


Fig. 8 A time-snippet of the roll rate (bottom) measured by the Geyser quadrotor for damage case 30FR, and the spectrogram of this signal showing peak harmonics related to the motor frequency (top).

in this particular set of frequencies. It is important to note here that the harmonics above the first are only computed for base harmonic frequencies which ensure a frequency separation of at least $3f_r$ (180 Hz) because smearing in the peaks of the STFT results in inaccurate estimates of amplitudes with low separation between sinusoids. Because the harmonics do not have significant contributions below (roughly) 250 Hz, this is not a major limitation.

3. Simplex B-splines

The final step of the system identification of the HF models is to fit a surface to each of the amplitude-frequency-damage scattered estimates for each harmonic, of each IMU signal, for all damage locations tested to obtain models of the form $A_n(f,d)$. Because of the highly non-linear local features of these surfaces, Simplex B-splines [35, 36] are used as the curve-fitting method of choice. Global polynomials models were also tried but did not give satisfactory results. Here, simplex B-splines are briefly summarised.

Simplex B-splines comprise of basis polynomials, defined locally over simplices t_i belonging to a triangulation \mathcal{T} , which are joined together to satisfy some prescribed continuity condition between polynomials of neighboring simplices. Simplices contain a local coordinate system known as Barycentric coordinates $\boldsymbol{b} = (b_0, ..., n_n) \in \mathbb{R}^{n+1}$ which uniquely map to point in \mathbb{R}^n . Given some point \boldsymbol{x} inside a simplex with vertices $(v_0, ..., v_n)$ where $v_i \in \mathbb{R}^n$, Eq. 30 relates the barycentric coordinates to \boldsymbol{x} . The barycentric coordinates $b_i \geq 0$ if \boldsymbol{x} is inside the simplex.

$$x = \sum_{i=0}^{n} b_i v_i \tag{30}$$

The B-form polynomials are defined in barycentric coordinates on a simplex according to Eq. 31 where c_{κ} are the B-coefficients of the polynomial set indexed with multi-index $\kappa = (\kappa_0, ..., \kappa_n) \in \mathbb{R}^n$ defined such that $|\kappa| = \sum_i \kappa_i$, $\kappa! = \prod_i \kappa_i$, and $\boldsymbol{b}^{\kappa} = \prod_i b_i^{\kappa_i}$ [35]. Each permutation of κ corresponds to a unique B-from polynomial and its B-coefficient, and the collective set forms a basis for the space spanned by all B-form polynomials of degree d in n variables.

$$p(\boldsymbol{b}) = \sum_{|\kappa|} c_{\kappa} \frac{d!}{\kappa!} \kappa \tag{31}$$

A continuity order r between B-form polynomials of neighboring simplices t_i and t_j are enforced through constraints on the respective B-coefficients of the two simplices using Eq. 32 where $\gamma = (\gamma_0, ..., \gamma_n)$ is another multi-index independent of κ , and w is the out-of-edge vertex. The continuity conditions for all simplices in the triangulation can be compiled into matrix form as shown in Eq. 33 where H is known as the 'smoothness matrix' [35].

$$c_{(\kappa_0,...,\kappa_{n-1},m)}^{t_i} = \sum_{|\gamma|=m} c_{(\kappa_0,...,\kappa_{n-1},0)+\gamma}^{t_j} B_{\gamma}^m(w), \quad 0 \le m \le r$$
(32)

$$Hc = 0 (33)$$

Given a pair of observations (x_i, y_i) related by some function f such that $y_i = f(x_i) + \epsilon_i$ where ϵ_i is a residual term. Then, the regression model for approximating f using a linear combination of B-form polynomials with degree d defined over a triangulation of f simplices is given by Eq. 34 where f are the barycentric coordinates of f with respect to simplex f. This expression can be written in matrix form to include all observations f through a data sifting matrix f which ensures that observations are only active within the simplices that contain them, explained in further detail by de Visser et al. [35]. The final spline-based regression model is then given by Eq. 35 where f is the vector of observations and f and f is the local regression matrix of all observations. Finally, the OLS estimation problem cost function is formulated as shown in Eq. 36. The equality-constrained OLS parameter estimator f using Lagrange multipliers f is then given by Eq. 37.

$$y_{i} = \sum_{j=1}^{J} \sum_{|\kappa|=d} c_{\kappa}^{t_{j}} B_{\kappa}^{d} (b_{i}) + \epsilon_{i}$$
(34)

$$Y = Xc + \epsilon \tag{35}$$

$$J_{OLS}(\mathbf{c}) = \frac{1}{2} (\mathbf{Y} - \mathbf{X}\mathbf{c})^T (\mathbf{Y} - \mathbf{X}\mathbf{c}) \text{ subject to } \mathbf{H}\mathbf{c} = 0$$
 (36)

$$\begin{bmatrix} \hat{\mathbf{c}} \\ \hat{\lambda} \end{bmatrix} = \begin{bmatrix} \mathbf{X}^T \mathbf{X} & \mathbf{H}^T \\ \mathbf{H} & 0 \end{bmatrix}^{+} \cdot \begin{bmatrix} \mathbf{X}^T \mathbf{Y} \\ 0 \end{bmatrix}$$
(37)

Simplex B-splines require the user to define a triangulation, the degree d, and continuity order r. These parameters are set based on the intuitive physical reasoning of the system being modeled, and certain best practices. In general, it is advised to start with a few simplices, low polynomial degree, and continuity order, and increase the complexity henceforth. For the amplitude surfaces presented in this paper, certain important aspects of the data must be considered when choosing a triangulation, degree, and continuity order. For one, the data are concentrated along the direction of frequency, while very sparse in the direction of damage level (see Fig. 27a). Secondly, the data is not uniformly scattered in the $f - d_l$ plane, but rather constrained in linear regions corresponding to each damage level. Because of these properties, a triangulation that is dense in the direction of f but sparse in the direction of f is chosen. An example is shown in Fig. 27a with 20 equally sized triangles. It is clear to see from the models presented in Sec IV.B that the local nonlinearities in the observed data are present along f, which is a further reason for more triangles along this direction. B-form polynomials with degree 3 and 1st order continuity were used to construct simple models which still capture the observed nonlinearities in the data.

A point to note is that the high-frequency models include both the blade damage level and frequency as regressors instead of building 1-dimensional spline models at each damage level separately. Surfaces are fit in the $f-d_l$ plane rather than curves for each damage level separately so that the amplitude models can facilitate the prediction of HF behavior at damage levels in between the rows of experimental data. An alternative approach to interpolate between damage levels would be to construct one-dimensional models as a function of frequency at all damage levels. Then, the corresponding B-coefficient parameter values of curves at the different damage levels can be interpolated to create interpolated spline curves. While there is no concrete proof that the applied method is better than this alternative, it does offer a more natural solution to the problem.

Table 6 Model performance metrics of aerodynamic force models around hover

		F	7 _x			F	⁷ y		F_z			
Case	NRMSE		\mathbb{R}^2		NRMSE		\mathbb{R}^2		NRMSE		R ²	
	Full	Test	Full	Test	Full	Test	Full	Test	Full	Test	Full	Test
Healthy	0.106	0.107	0.989	0.989	0.111	0.109	0.988	0.988	0.081	0.080	0.993	0.994
10F	0.117	0.118	0.986	0.986	0.090	0.090	0.992	0.992	0.077	0.078	0.994	0.994
10BL	0.157	0.157	0.975	0.975	0.087	0.086	0.992	0.993	0.080	0.081	0.994	0.993
10FL	0.113	0.110	0.987	0.988	0.125	0.125	0.984	0.984	0.125	0.125	0.984	0.984
20F	0.129	0.125	0.983	0.984	0.100	0.102	0.990	0.990	0.062	0.062	0.996	0.996
20BL	0.125	0.118	0.984	0.986	0.079	0.078	0.994	0.994	0.065	0.065	0.996	0.996
20BR	0.086	0.083	0.993	0.993	0.100	0.107	0.990	0.989	0.066	0.067	0.996	0.996
20FL	0.118	0.113	0.986	0.987	0.087	0.090	0.992	0.992	0.071	0.071	0.995	0.995
30F	0.083	0.083	0.993	0.993	0.074	0.071	0.995	0.995	0.066	0.067	0.996	0.996
30BL	0.077	0.078	0.994	0.994	0.069	0.072	0.995	0.995	0.063	0.064	0.996	0.996
30FL	0.085	0.084	0.993	0.993	0.073	0.073	0.995	0.995	0.072	0.072	0.995	0.995

IV. Results

A. Aerodynamics Models

1. Stepwise regression Models

Tables 6 and 7 respectively present the model performance metrics of the SWR force and moment models constructed for the low-speed flight regime. Tables 8 and 9 respectively present the model performance metrics for the force and moments models identified for the high-speed flight regime. It is evident that all the low-speed force and moment models give very good performance except for the yawing moment model, which was difficult to excite during the system-identification test flights. For high-speed flight, all the models perform worse except for M_x , with F_x and M_y particularly worse than the other models. Overall, however, all the models give decent performance and can be used for simulation purposes. The ratio of training data to test data was 75:25 for all the models. The similarity between the metrics for the test and the complete set shows that the models do not overfit the data.

To examine whether the SWR models actually capture the effects of blade damage, a 'model confusion matrix' was constructed. This matrix is constructed for each force and moment model, for all damage cases. The models for each damage case are applied to the observed data of all damage cases, and the NRMSE is computed for all combinations. Each row of the matrix represents the SWR model of the damage case, while the columns represent the training data for the damage case. With the matrix of NRMSE values computed, the relative NRMSE R_{NRMSE} values of the off-diagonal elements are computed with respect to the corresponding diagonal elements through Eq. 38. Based on this definition, if the off-diagonal elements have values above 1, this means that the model from one damage case fit the data of another damage case better, while values below 1 suggest the opposite.

$$R_{NRMSE_{ij}} = \frac{NRMSE_{ij}}{\min (NRMSE_{ii}, NRMSE_{jj})}$$
(38)

Figures 9 and 10 show the model confusion matrices for the low-speed and high-speed aerodynamic models respectively. These are computed by averaging (element-wise) the confusion matrices of each force and moment model. The results show that models applied to off-diagonal elements can have significantly lower NRMSE values, suggesting that the models for each damage case actually capture the effects of blade damage on the aerodynamics of the quadrotor. Although this is a week argument, when combined with the high R^2 values for each model (except M_z), however, it can be quantitatively concluded that the effects of blade damage are indeed captured.

Table 7 Model performance metrics of aerodynamic moment models around hover

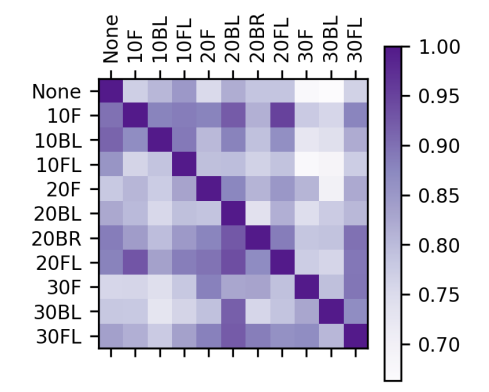
		M	I_x			N	I_y		M_z			
Case	NRMSE		\mathbb{R}^2		NRI	NRMSE		\mathbb{R}^2		NRMSE		22
	Full	Test	Full	Test	Full	Test	Full	Test	Full	Test	Full	Test
Healthy	0.170	0.185	0.971	0.966	0.228	0.230	0.948	0.947	0.603	0.595	0.636	0.646
10F	0.120	0.122	0.986	0.985	0.137	0.132	0.981	0.983	0.625	0.624	0.610	0.611
10BL	0.126	0.128	0.984	0.984	0.166	0.168	0.972	0.972	0.620	0.621	0.615	0.614
10FL	0.156	0.156	0.976	0.976	0.167	0.181	0.972	0.967	0.568	0.567	0.678	0.679
20F	0.155	0.149	0.976	0.978	0.160	0.154	0.974	0.976	0.691	0.703	0.522	0.505
20BL	0.208	0.208	0.957	0.957	0.184	0.194	0.966	0.962	0.817	0.728	0.332	0.470
20BR	0.142	0.141	0.980	0.980	0.190	0.175	0.964	0.969	0.733	0.745	0.463	0.445
20FL	0.144	0.146	0.979	0.979	0.143	0.146	0.979	0.979	0.663	0.652	0.561	0.574
30F	0.146	0.145	0.979	0.979	0.180	0.173	0.967	0.970	0.685	0.684	0.53	0.532
30BL	0.195	0.201	0.962	0.960	0.155	0.160	0.976	0.974	0.747	0.746	0.441	0.444
30FL	0.185	0.207	0.966	0.957	0.193	0.195	0.963	0.962	0.670	0.671	0.551	0.550

Table 8 Model performance metrics of aerodynamic force models in high-speed flight

		F	\vec{r}_x			F	⁷ y		$\overline{F_z}$			
Case	NRMSE		\mathbb{R}^2		NRMSE		\mathbb{R}^2		NRMSE		R ²	
	Full	Test	Full	Test	Full	Test	Full	Test	Full	Test	Full	Test
Healthy	0.205	0.206	0.958	0.957	0.137	0.133	0.981	0.982	0.129	0.131	0.983	0.983
10F	0.252	0.250	0.937	0.937	0.150	0.153	0.978	0.977	0.167	0.164	0.972	0.973
10BL	0.156	0.155	0.976	0.976	0.194	0.198	0.962	0.961	0.141	0.142	0.980	0.980
10FL	0.139	0.140	0.981	0.980	0.162	0.166	0.974	0.972	0.130	0.132	0.983	0.983
20F	0.261	0.260	0.932	0.932	0.140	0.144	0.980	0.979	0.135	0.136	0.982	0.981
20BL	0.250	0.251	0.937	0.937	0.099	0.093	0.990	0.991	0.139	0.140	0.981	0.980
20BR	0.219	0.222	0.952	0.951	0.096	0.096	0.991	0.991	0.134	0.134	0.982	0.982
20FL	0.235	0.236	0.945	0.944	0.198	0.208	0.961	0.957	0.156	0.157	0.976	0.975
30F	0.247	0.247	0.939	0.939	0.106	0.105	0.989	0.989	0.145	0.144	0.979	0.979
30BL	0.284	0.283	0.919	0.920	0.122	0.125	0.985	0.984	0.137	0.135	0.981	0.982
30FL	0.258	0.261	0.934	0.932	0.116	0.117	0.987	0.986	0.145	0.144	0.979	0.979

Table 9 Model performance metrics of aerodynamic moment models in high-speed flight

		N	I_x		M_{y}					
Case	NRMSE		R	\mathbb{R}^2	NRI	MSE	R	22		
	Full	Test	Full	Test	Full	Test	Full	Test		
Healthy	0.124	0.128	0.985	0.984	0.279	0.324	0.922	0.895		
10F	0.119	0.121	0.986	0.985	0.270	0.235	0.927	0.945		
10BL	0.115	0.114	0.987	0.987	0.435	0.427	0.811	0.818		
10FL	0.114	0.114	0.987	0.987	0.250	0.215	0.937	0.954		
20F	0.122	0.122	0.985	0.985	0.254	0.253	0.935	0.936		
20BL	0.126	0.126	0.984	0.984	0.204	0.206	0.958	0.958		
20BR	0.195	0.197	0.962	0.961	0.420	0.431	0.824	0.814		
20FL	0.105	0.105	0.989	0.989	0.307	0.285	0.906	0.919		
30F	0.217	0.232	0.953	0.946	0.528	0.621	0.721	0.614		
30BL	0.237	0.225	0.944	0.949	0.449	0.412	0.798	0.830		
30FL	0.136	0.126	0.982	0.984	0.316	0.318	0.900	0.899		



1.00 0.95 None 10F 10BL 10FL 20F 20BL 0.80 20BR 0.75 20FL 30F 0.70 30BL 30FL 0.65

Fig. 9 Element-wise average of model confusion matrices for all low-speed aerodynamic models

Fig. 10 Element-wise average of model confusion matrices for all high-speed aerodynamic models

2. Simplified Fixed-Regressor Models

The simplified models for the low-speed and high-speed flight regime were built using the regressors listed in Tables 10 and 11 respectively. These regressors were chosen based on the semi-quantitative procedure described in Sec. III.C. The regressor choices are fairly symmetric for the low-speed case because of the symmetry of the flight maneuvers, evident from the similarities in the F_x and F_y , and F_y , and F_y , and F_y are clearly influenced by the effects of the higher mean airspeed.

Figure 11 shows how the model performance metrics differ between the SWR and FR models, for both speed regimes. Interestingly, the FR models for F_y , F_z , and M_x are virtually as good as the SWR counterparts. The M_y FR models for both airspeed regimes are similarly reduced in accuracy, while for F_x only the high-speed models are significantly worse. These results suggest that the simplification of the models does not significantly reduce the performance of the models. It is again highlighted here that the purpose of the simplifications was to obtain models for different cases with the same set of regressors so that the parameter variations between the damage cases can be compared.

Figures 12-16 plot the variation of parameter values as a function of blade damage extent and location for the various force and moment models of the low-speed regime. The standard deviations of the parameters are plotted as error bars.

Table 10 Selected regressors for simplified low-speed models Table 11 Selected regressors for simplified high-speed models

Mo	odel	Regress	sors				Model	Regressors
	\overline{Y}_{X} l	$\iota, \sin(\theta)$	ω_{tot}				$\overline{F_x}$	$u, \sin(\theta)\mu_x, \sin(\theta)u^2$
I	\overline{y} 1	ϕ , $\sin(\phi)$	ω_{tot}				$F_{\mathbf{y}}$	$v, \sin(\phi)\omega_{tot}$
1	F_z	w, ω_t^2	ot				F_z	w, ω_{tot}^2
Λ	$I_x p$	$, u_p, co$	$s(\phi)v$				M_{x}	$p, u_p, \cos(\phi)v$
Λ	$I_y q$	u_q , co	$s(\theta)u$				M_{y}	q, u_q, μ_z
N	I_z 1	r, u_r, ω_t	$_{ot}u_r$				M_z	-
	F_{i}	x	F_y		F_{\cdot}	ı z	M_x	M_y
1.0 - C C C C C C C C C C C C C C C C C C				peed - m/s m/s		-		
NRMSE	SWR -	Œ.	SWR -	- FR	SWR -	Æ	SWR -	SWR - HR

Fig. 11 Model performance metric comparison between the SWR models and the simplified fixed regressor (FR) models

It is evident from these plots that, in general, no simple patterns can be found the parameter values of most of the regressors.

Intuitively, the control moment parameters corresponding to regressors u_p and u_q for the M_x and M_y model respectively are expected to decrease in magnitude with increasing levels of damage. While this is the case for M_x , the decrease in control effectiveness does not follow a logical trend with some model 10% damage showing an increase in control effectiveness compared to the base models. For example, the control effectiveness remains almost unaffected up to 20% FL damage. The models for M_y on the other hand show an increase in pitch control effectiveness with increasing blade damage which is physically impossible. The bias terms for both M_x and M_y do however show consistent patterns. For example, the M_x bias for F (front) damage stays around the bias corresponding to no damage, which makes sense because the damage is symmetric about the xz plane. The biases for both left-side damage cases –FL and BL– are in agreement, while bias for the BR case seems to be reflected about the zero-damage case bias. Similarly, the bias in M_y is worse for the F damage case compared to the single damage cases, and all the bias decreases or increases in the expected directions in accordance with the location of the damage.

Lastly, the parameters corresponding to the ω_{tot}^2 regressor show a clear pattern with respect to the damage level. There is almost a linear trend, with the F damage case having a higher slope. This makes physical sense, but the question arises why, from the same data, do the control effectiveness parameters not follow meaningful patterns? This is further explored in the next subsection.

The parameters of the high-speed regime models largely show the same non-patterns with respect to blade damage and are therefore omitted for brevity. Interestingly, the M_x models in the high-speed regime reveal clearer patterns in the parameters, as shown in Fig. 17 compared to the low-speed models. The regressor p has the physical interpretation of acting as a damping term. The parameters of this regressor do show a much more prominent pattern than the others (except the bias). Looking at the regressor values, it appears that the roll damping is decreased in the case of front damage, while it is increased in the case of rear damage in the high-speed regime.

The models built by SWR, and therefore the selected regressors are influenced strongly by the system identification

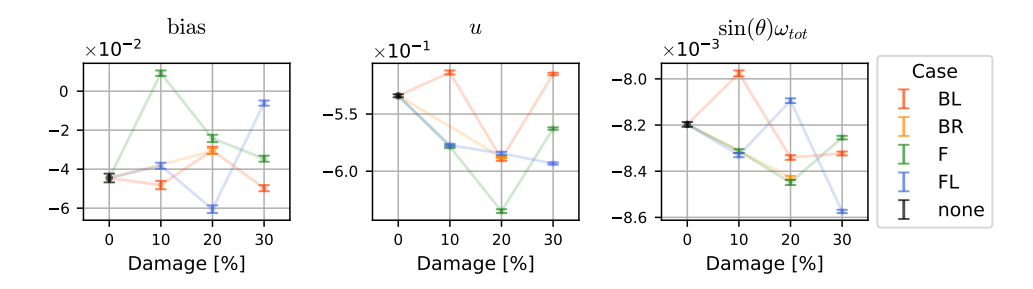


Fig. 12 F_x parameter variations with damage level and location (low-speed regime)

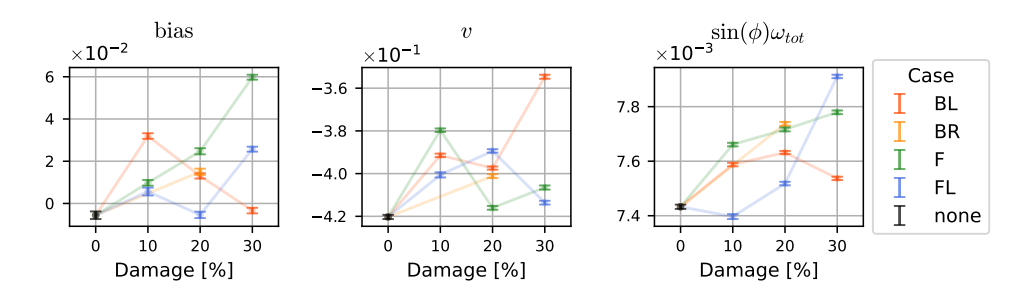


Fig. 13 F_y parameter variations with damage level and location (low-speed regime)

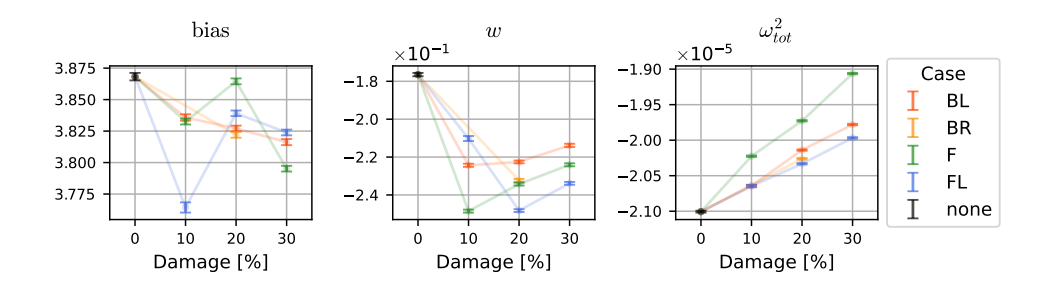


Fig. 14 F_z parameter variations with damage level and location (low-speed regime)

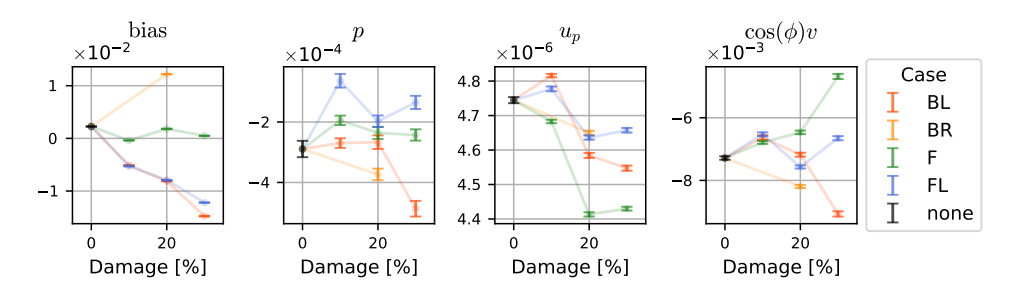


Fig. 15 M_x parameter variations with damage level and location (low-speed regime)

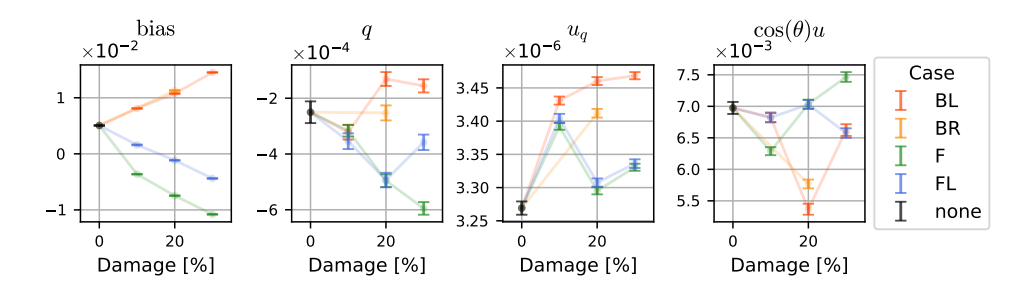


Fig. 16 M_{ν} parameter variations with damage level and location (low-speed regime)

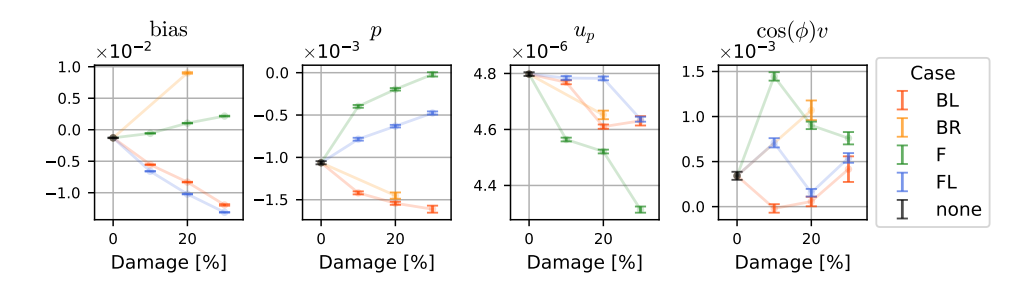


Fig. 17 M_x parameter variations with damage level and location (high-speed regime)

maneuvers performed and the regime of airspeeds flown. This is evident by the fact that the regressor $\cos(\theta)u$ selected for the hovering flight was not selected for any of the high-speed models, which apart from being identified at a much higher mean airspeed, also lack the slow speed rolling maneuvers which were performed for the hovering case.

3. Control Effectiveness Analysis

This section tries to uncover the reason for the sporadic estimates of the control effectiveness parameters of the pitching and rolling moments described in the previous subsection. Figures 18 and 19 respectively show the low-speed and high-speed observed forces/moments from training data plotted against the respective primary control effectiveness regressors. Each plot also shows a simple linear model fit to the respective data.

For the F_z model of both speed regimes, a linear trend is clearly observed between F_z and ω_{tot}^2 with decreased slope magnitude at higher damage levels. This is in line with expected behavior; the quadrotor should be less effective in producing thrust when blade damage is present. Conversely, the slope of the (low-speed) M_y model actually increases with increasing damage level, which was also the case for the simplified models shown in Fig. 16.

The low-speed M_x data shows that there are 2 distinct patterns between u_p and M_x . For example, the M_x data shows dominant linear behavior from -0.15 to 0.15 Nm but there is another region with a lower slope, which is active on a smaller range of moment values, roughly -0.03 to 0.03 Nm. This additional non-linear effect was found to occur during the lateral maneuvers while the dominant linear behavior corresponds to the quick roll maneuvers where the lateral airspeed remains close to zero. In the high-speed test flight, only fast roll maneuvers could be performed so as to make sure the quadrotor stays within the jet of the wind tunnel. This is also evident by the fact that the high-speed M_x data shown in Fig. 19 only shows the dominant linear pattern.

Similar to the phenomenon for M_x , similar features can be seen in the M_y data. Unlike the M_x , the pitching moment could be excited both through fast pitch maneuvers as well as slower longitudinal maneuvers during high-speed flight. This is clearly evident in Fig. 19 where two distinct linear regions are visible. The presence of these dual patterns results in the models identified from the data being an unweighted average of both patterns. Since the patterns arise based on the maneuvers performed, differences in flight maneuvers result in different distributions of data for each maneuver which eventually impact the control effectiveness parameters. This would also explain why the high-speed M_x models shown in 17 show clearer patterns than the other models, only one type of maneuver was flown for this case.

These findings suggest that linear-in-the-parameters models may not be sufficient to model the dynamics of a quadrotor from a physical perspective. For example, the roll control effectiveness is found to depend on additional

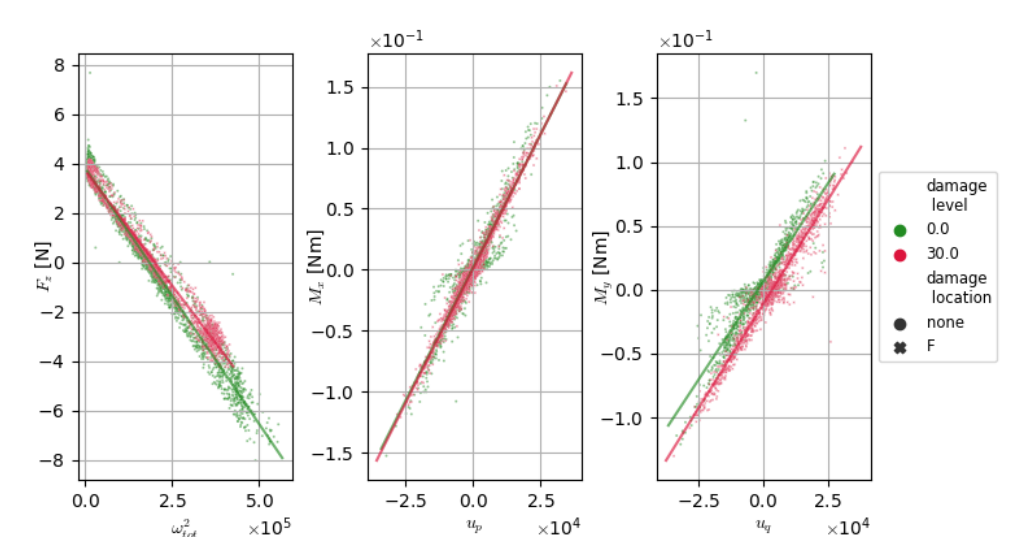


Fig. 18 Control effectiveness comparison plots for low-speed flight data

states such as lateral airspeed in a non-linear fashion, while also of course depending on the control input created by the combination of rotor speeds.

B. High-Frequency Models

1. Spectral Analysis

While the simplex B-spline models are the primary result of the HF models, the frequency-amplitude data gathered from the spectral analysis of the raw IMU data is interesting to analyze. Here, the results obtained for a variety of damage cases for both the Beetle and Geyser drone are presented. First, the results for a single damage case are presented which show the amplitude-frequency relationships of three harmonics for each IMU axis. Then, similar plots are shown for increasing levels of damage at a single location. Finally, results are shown for the same damage level at all four damage locations.

Figures 20 and 21 show the f-A relationships as mean value (solid lines) and 2σ bands (shaded regions) for the Beetle and Geyser quadrotors respectively. These results are obtained from a single flight with duration around 120 seconds. The duration of flights for the remainder of the HF spectral analysis results are derived from flights of similar duration.

Since the accelerometer on the Beetle is sampled at 1000 Hz, only the first harmonic is extracted. Another important point to note is that the accelerometers of both quadrotors have a limit of 16 g (160 m/s), yet the estimated amplitudes tend to surpass this value for the Beetle. This occurs at frequencies close to the Nyquist limit (500 Hz), where the STFT does start to break down given the very short time windows. This is an inherent limitation and requires the use of IMUs with higher sampling rates and higher saturation limits. Additionally, as mentioned in Sec. III.B, high frequencies are difficult to excite in an indoor environment, which results in fewer data points in these regions, accounting partly for the noisy data at frequencies above 450 Hz.

Figure 21 shows that the high-frequency region (>450 Hz) for the Geyser drone is less noisy than the Beetle. Unlike the Beetle, the accelerometer of the Geyser has a logging rate of 8 kHz. Additionally, the higher mass of the Geyser results in higher hovering RPM, making the full range of frequencies easier to cover through throttle punch maneuvers. The higher inertia of the Geyser also makes the accelerometer less susceptible to clipping.

It is interesting to note that the harmonics above the base harmonic have a relatively small contribution to the time-series signal. For the Beetle, the higher harmonics only contribute significantly to the yaw rate, while the Geyser has the highest contributions in a_z with noticeable peaks around 300 Hz for the other IMU measurements.

Figure 22 shows that increasing levels of blade damage manifest in clear differences between the f - A relationships for all the IMU axes of the Beetle quadrotor. Figure Figure 24 also shows that the location of damage results in different

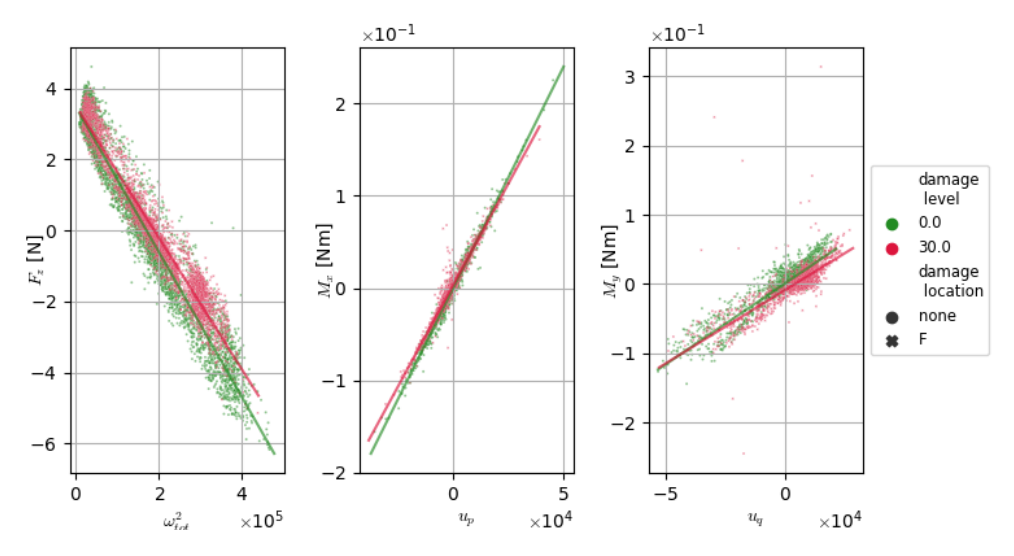
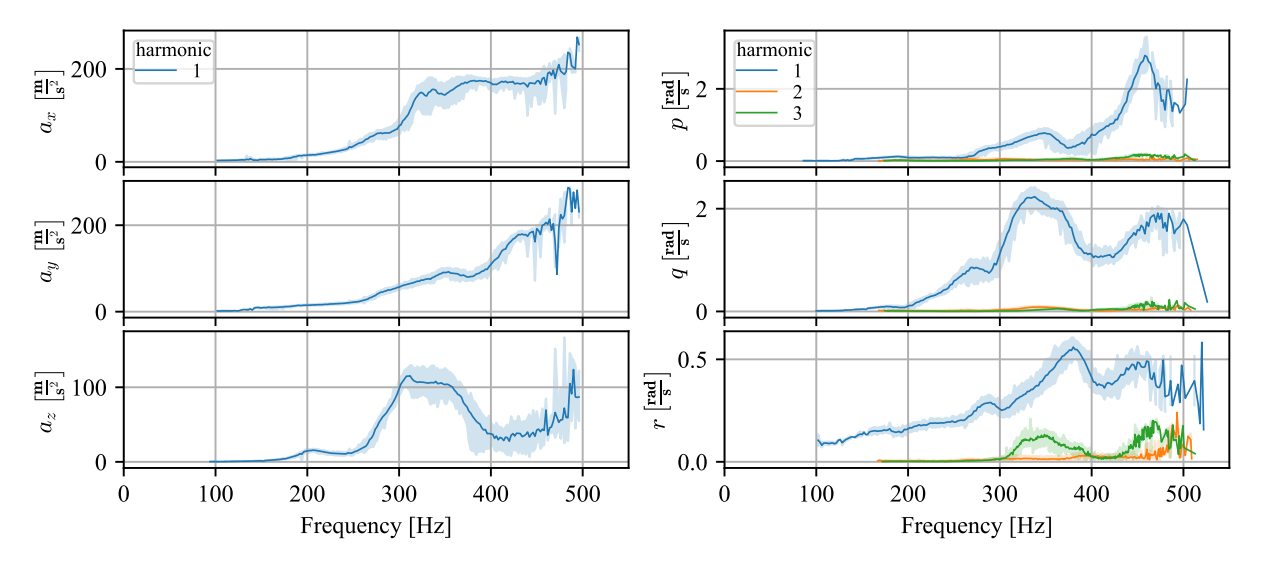


Fig. 19 Control effectiveness comparison plots for low-speed flight data



 $Fig.\ 20\quad Amplitude-frequency\ relationships\ of\ the\ Beetle\ quadrotor\ with\ damage\ case\ 30FR$

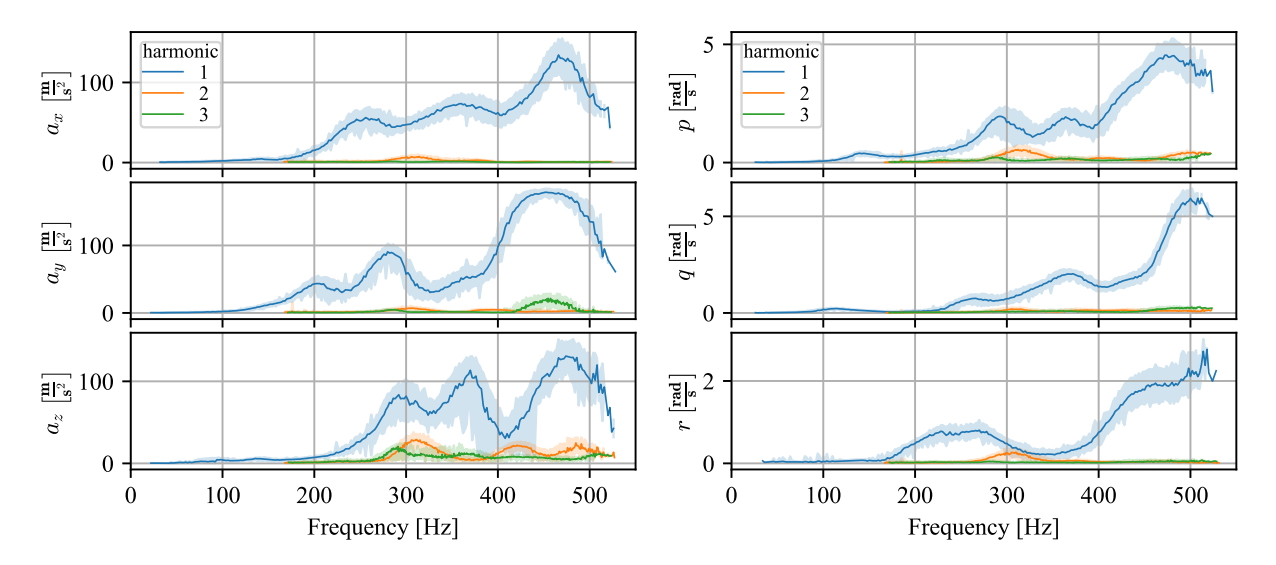


Fig. 21 Amplitude-frequency relationships of the Geyser quadrotor with damage case 30FR

f-A relationships at the same damage level. In both the figures, there are multiple lines of the same color which signifies data obtained from completely separate flights with the same damage case, which shows the reproducibility of the results obtained from the spectral analysis procedure explained in Sec. III.D. It is interesting to see that the curves at different damage levels show similar localized features which increase in prominence as the damage level increases. These highly non-linear effects are likely caused by structural resonance in the airframe, and complex aerodynamic interactions.

Figure 23 and 25 show the same effects seen from the corresponding plots for the Beetle quadrotor on the Geyser quadrotor. However, the mean f-A curves appear to be noisier for the Geyser, with larger 2σ bands. After a closer inspection of the raw IMU data, and the frequency and amplitude estimates at each time point, it was found that there may be a dependence of amplitude on additional states apart from f. For example, Fig. 26 shows the roll-rate data of the Geyser with damage case 30FR. A clear oscillation in the amplitude of the signal is seen which at first looks independent of the frequency of the signal, but there is a pattern visible of lower amplitudes corresponding to lower frequencies and vice-versa. This oscillation in frequency is also weakly visible in the STFT plot. These oscillations in amplitude were also observed on the Beetle but to a much lower extent.

There are two explanations for the high-frequency amplitude oscillation phenomenon. For one, the assumption that the amplitude is only a function of frequency may still be valid. This suggests that the high-frequency oscillations in frequency are caused by fast oscillation in motor RPM values, and the amplitude is directly related to these frequency oscillations. However, it is difficult to resolve these dynamics with the STFT because the frequency changes very rapidly. This essentially means that the signal is too non-stationary to capture the frequency and amplitude by analyzing even small time windows. This is also visible in Fig. 26, where the estimated amplitude does not perfectly conform to the signal.

Alternatively, there may be hidden states governing this oscillation in signal amplitude. It is important to note that the flight controller on the Geyser drone is mounted on the airframe via rubber standoffs which include metal inserts for securing the board with fasteners. The Beetle on the other hand has steel standoffs that are many orders of magnitude stiffer. It is possible that the high levels of vibration cause non-linear structural effects through the rubber standoffs which do not occur with the same severity on the Beetle. In either case, even though the high-frequency amplitude and frequency oscillation of the signal cannot be resolved, the mean f - A relations are still captured.

2. Simplex B-spline Models

The surfaces of the simplex B-spline models constructed for the Beetle quadrotor of the amplitudes corresponding to the first harmonic, for the FR damage case, are presented in Fig. 27. The training data is also shown in these plots but reduced to the mean value at each frequency bin for each damage level. The spline surfaces go through the training data and are able to capture all the local non-linearities in the data. Additionally, the regions in between the rows of training

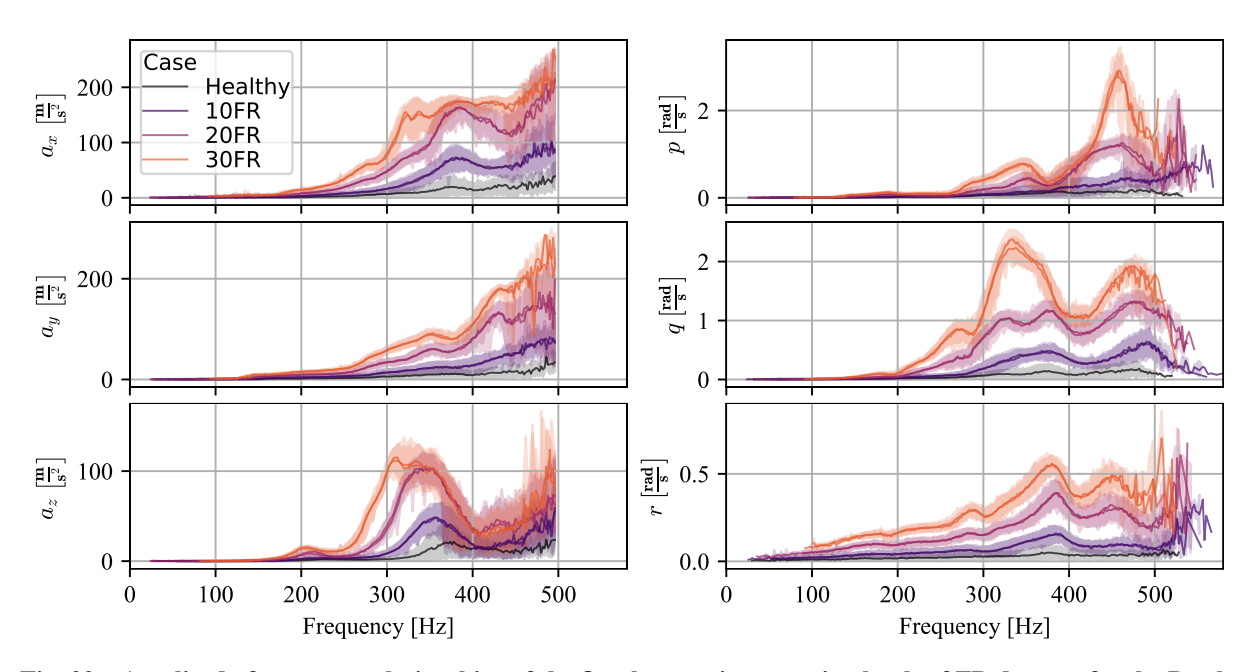


Fig. 22 Amplitude-frequency relationships of the first harmonic at varying levels of FR damage for the Beetle

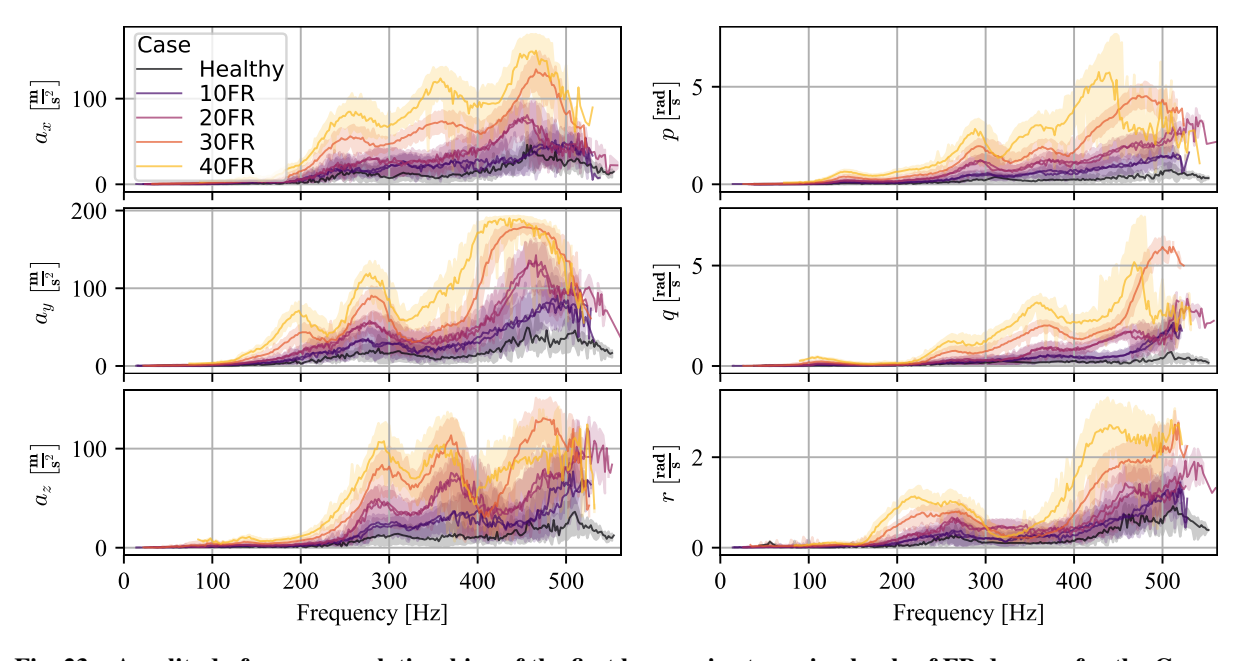
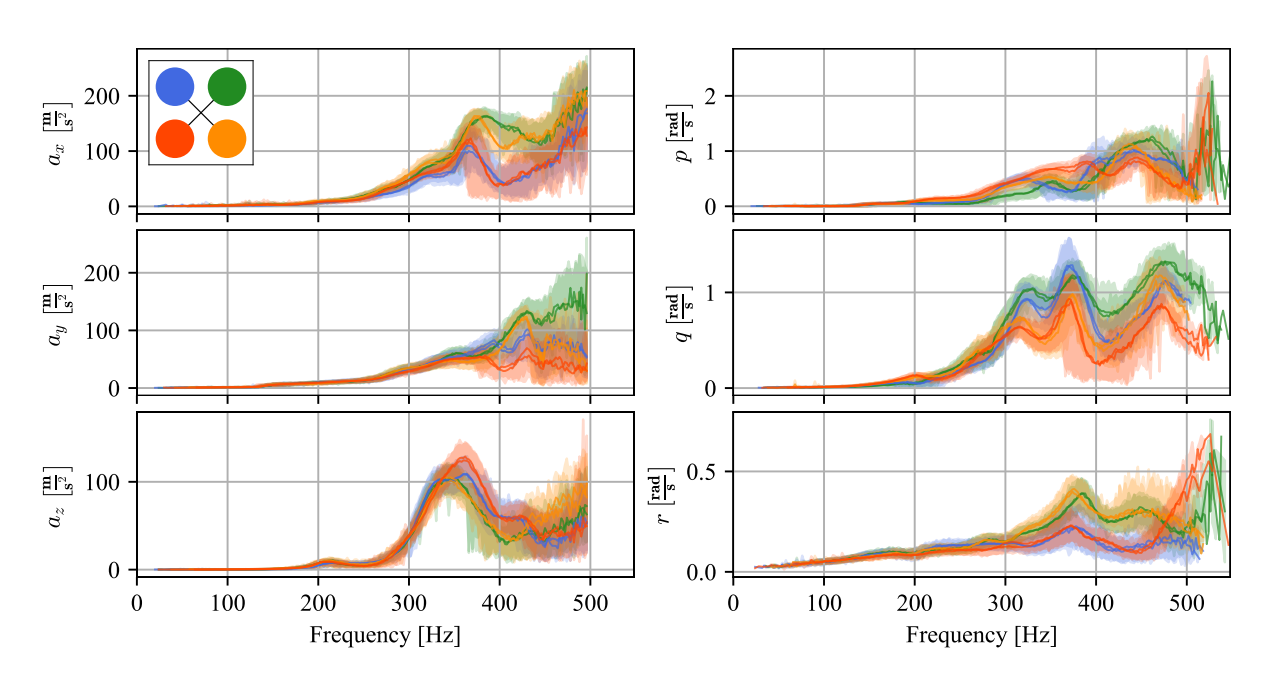
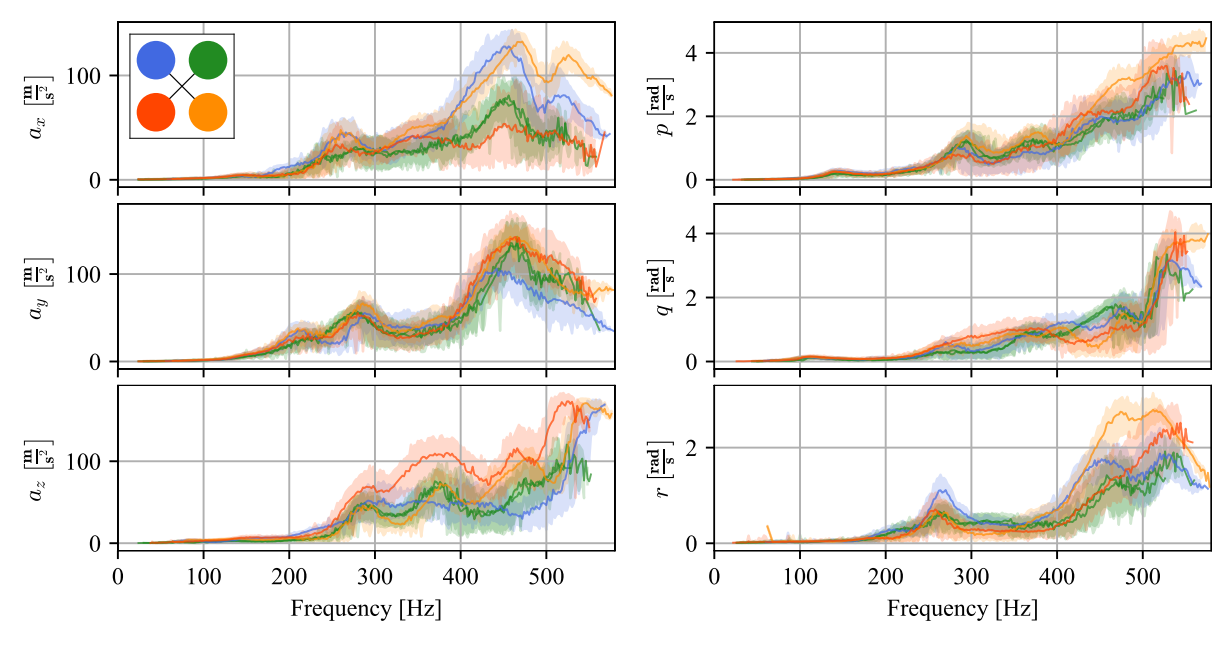


Fig. 23 Amplitude-frequency relationships of the first harmonic at varying levels of FR damage for the Geyser



 $Fig. \ 24 \quad Amplitude-frequency \ relationships \ of the \ first \ harmonic \ at \ varying \ locations \ with \ 20\% \ damage \ for \ the \ Beetle$



 $\label{eq:continuous} \textbf{Fig. 25} \quad \textbf{Amplitude-frequency relationships of the first harmonic at varying locations with 20\% damage for the Geyser}$

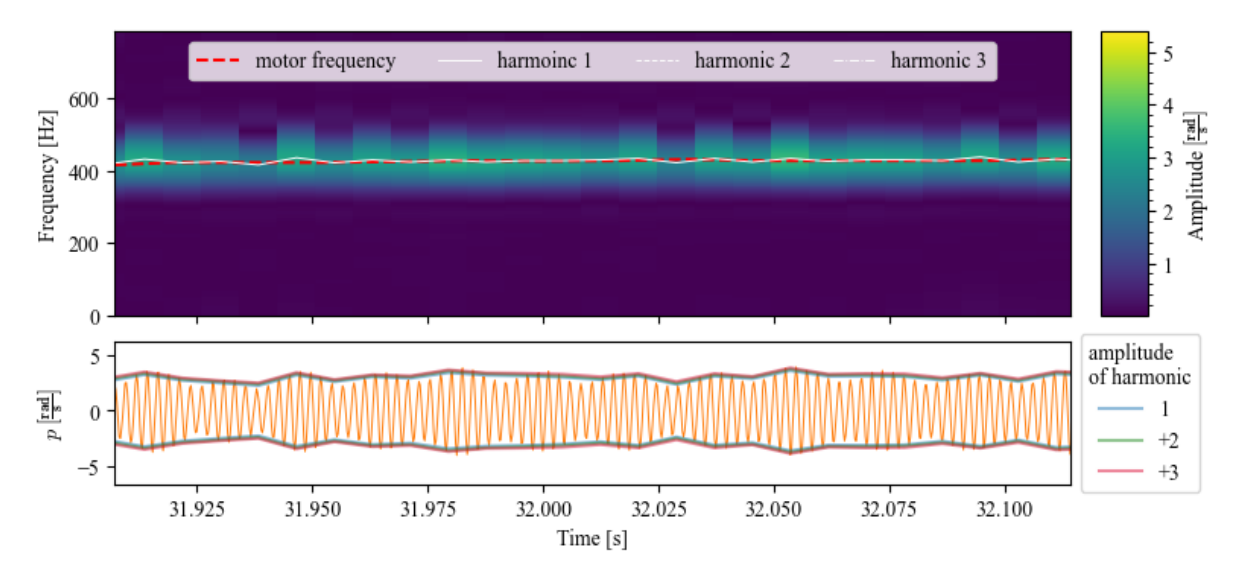


Fig. 26 A time-snippet of the roll rate (bottom) measured by the Geyser quadrotor for damage case 30FR, and the spectrogram of this signal showing peak harmonics related to the motor frequency (top)

data appear to be qualitatively well interpolated by the spline models. The models for the second harmonic are shown in Fig. 28. The training data appears nosier in this case but it is also important to notice that the amplitudes of the second harmonic are much lower in value than that of the first harmonic. The training data is especially noisy in the low and high-frequency regions. The noise in the low-frequency region is likely caused by leakage of amplitudes estimated for the first harmonic into the second harmonic, while noise in the high-frequency regions is likely because of fewer data points in each frequency bin as explained in the previous section.

The performance metrics for the various simplex B-spline models of the Beetle quadrotor are summarised in Table 12 and Table 13 for the accelerometer and gyroscope models respectively. The results are shown calculated on the entire dataset (*Full*) as well as the validation set (*Test*). The data was split randomly into the 80:20 ratio for the training and validation sets for all the models. Note that because the MPU6000 IMU is limited to 1 kHz, only the first harmonic models are possible to construct for the Beetle.

From the results, some general conclusions can be drawn. The base harmonic models generally perform significantly better than those corresponding to higher harmonics. Since the base harmonic is the dominant component, this is not a very consequential limitation. The performance metrics for the validation data are comparable to those of the complete dataset, which indicates that the models do not overfit the training data.

It is interesting to note the BL accelerometer models show worse performance than the other damaged locations. Looking at the top row of plots in Fig. 29, it appears that noise in the high-frequency regions (>450 Hz) is the probable cause. The noisy data in the high-frequency region are likely present because of the proximity of these frequencies to the Nyquist limit (500 Hz). The gyroscope models for the BL case are not always worse than the other damage locations. The gyroscope data is sampled at 8 kHz, which further suggests that accelerometer model training data is inflicted with noisy estimates due to proximity to the Nyquist limit.

The performance metrics for the simplex B-spline models of the Geyser quadrotor are summarised in Table 14 and Table 15 for the accelerometer and gyroscope models respectively. Unlike the Beetle, the 8 kHz sampling rate of the accelerometer in the ICM42605 IMU facilitates the identification of accelerometer models at harmonics higher than the base harmonic. Note that models only for the FR location are presented even though Table 4 suggests that all 4 single-damage locations were tested. This is because apart from the FR case, the other cases only cover one damage level, to qualitatively analyze how the f-A relationships change based on damage location, at the same damage level, for the Geyser quadrotor.

On average, the base harmonic models of the Geyser seem to be slightly worse than the Beetle. This is likely because of the high-frequency amplitude oscillations phenomenon described in the previous section. The models of the higher harmonics also show significantly worse performance than those of the base harmonics, as was the case with the Beetle.

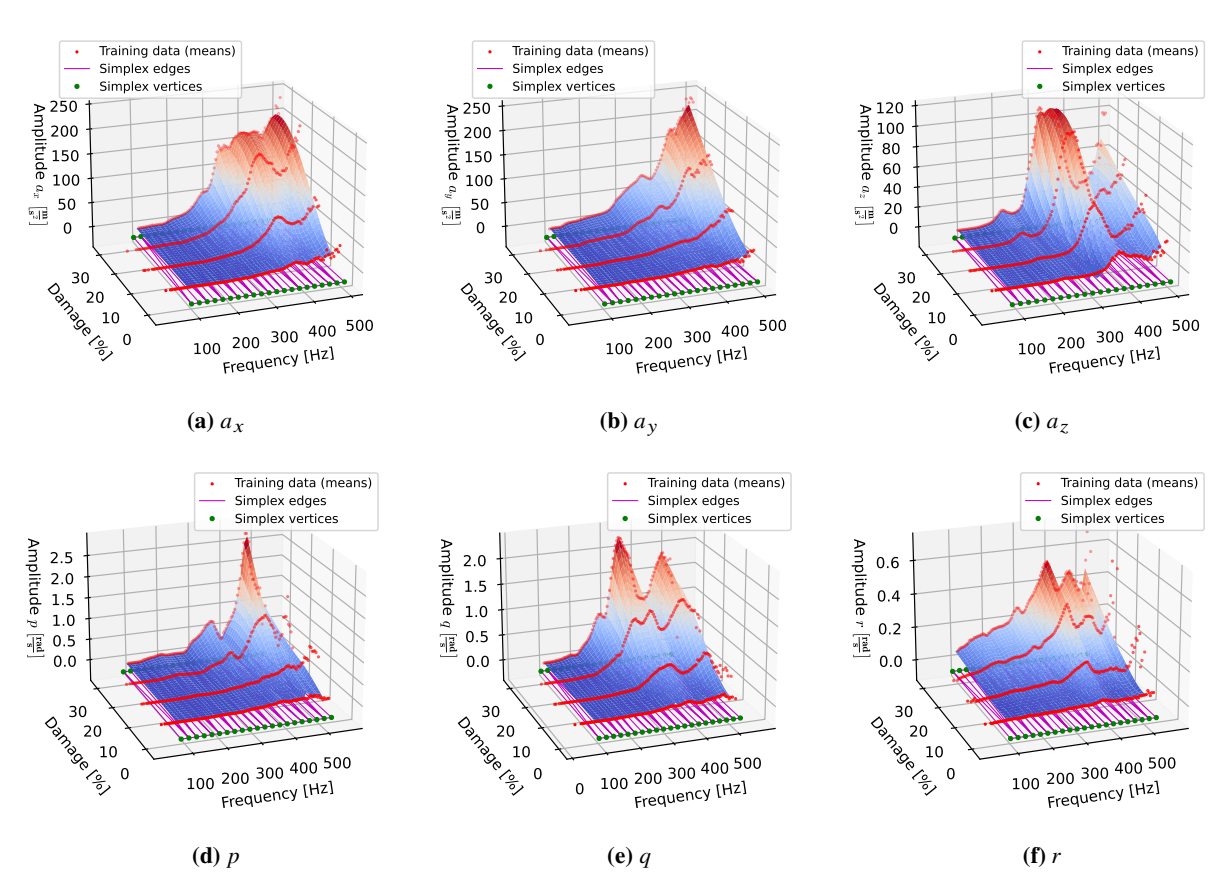


Fig. 27 Spline models of the Beetle for FR damage (Harmonic 1)

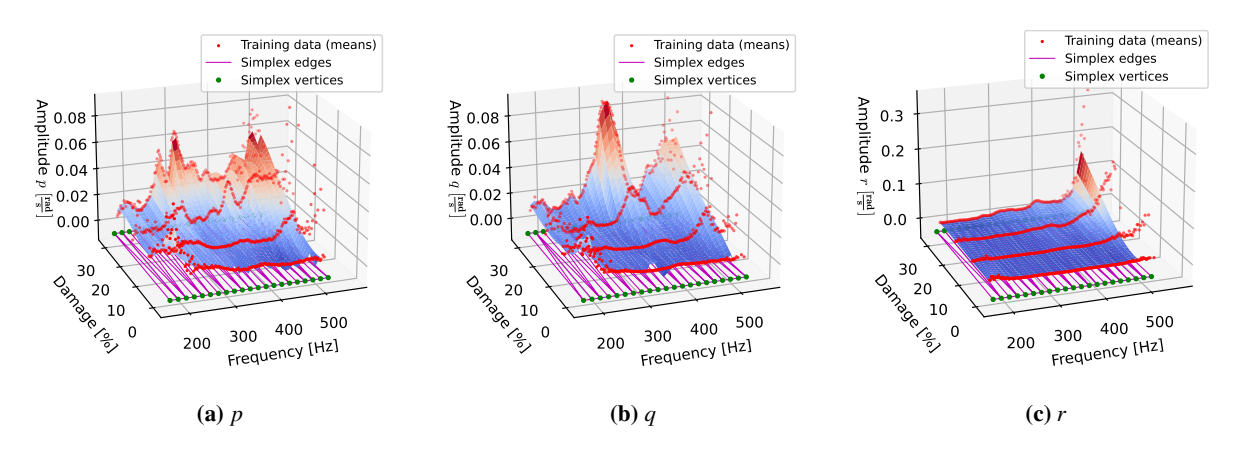


Fig. 28 Spline models of the Beetle for FR damage (Harmonic 2)

Table 12 Model performance metrics for the HF acceleration models of the Beetle quadrotor (h = harmonic)

			а	x		a_y				a_z				
Case	h	NRMSE		\mathbb{R}^2		NRMSE		\mathbb{R}^2		NRMSE		\mathbb{R}^2		
		Full	Test	Full	Test	Full	Test	Full	Test	Full	Test	Full	Test	
FR	1	0.171	0.173	0.971	0.970	0.194	0.191	0.963	0.964	0.239	0.241	0.943	0.942	
FL	1	0.285	0.292	0.919	0.915	0.200	0.201	0.960	0.960	0.223	0.219	0.950	0.952	
BR	1	0.174	0.173	0.969	0.970	0.220	0.222	0.952	0.951	0.147	0.147	0.979	0.979	
BL	1	0.323	0.323	0.895	0.896	0.309	0.302	0.905	0.909	0.189	0.186	0.964	0.966	

Table 13 Model performance metrics for the HF angular-rate models of the Beetle quadrotor (h = harmonic)

			1	p		q				r				
Case	h	NRMSE		\mathbb{R}^2		NRI	NRMSE		\mathbb{R}^2		NRMSE		R ²	
		Full	Test	Full	Test	Full	Test	Full	Test	Full	Test	Full	Test	
	1	0.243	0.236	0.941	0.945	0.137	0.134	0.981	0.982	0.180	0.179	0.967	0.968	
FR	2	0.525	0.536	0.724	0.712	0.38	0.398	0.855	0.841	0.457	0.475	0.771	0.759	
	3	0.318	0.317	0.893	0.894	0.391	0.402	0.815	0.819	0.349	0.352	0.877	0.875	
	1	0.253	0.250	0.936	0.937	0.169	0.168	0.971	0.972	0.365	0.367	0.867	0.866	
FL	2	0.495	0.482	0.755	0.767	0.532	0.513	0.718	0.737	0.462	0.464	0.784	0.781	
	3	0.367	0.368	0.864	0.863	0.389	0.387	0.816	0.815	0.322	0.323	0.882	0.882	
	1	0.217	0.218	0.953	0.953	0.206	0.204	0.958	0.958	0.176	0.176	0.969	0.969	
BR	2	0.286	0.288	0.920	0.918	0.625	0.620	0.615	0.622	0.509	0.519	0.591	0.583	
	3	0.274	0.272	0.912	0.913	0.172	0.163	0.895	0.896	0.258	0.262	0.929	0.928	
	1	0.209	0.216	0.956	0.953	0.288	0.287	0.917	0.918	0.305	0.299	0.905	0.909	
BL	2	0.455	0.403	0.791	0.837	0.634	0.634	0.594	0.594	0.491	0.470	0.747	0.764	
	3	0.268	0.271	0.925	0.924	0.245	0.237	0.934	0.937	0.275	0.279	0.924	0.922	

Table 14 Model performance metrics for the HF acceleration models of the Geyser quadrotor (h = harmonic)

	h	a_x				a_y				a_z			
Case		NRMSE		\mathbb{R}^2		NRMSE		\mathbb{R}^2		NRMSE		\mathbb{R}^2	
		Full	Test	Full	Test	Full	Test	Full	Test	Full	Test	Full	Test
	1	0.236	0.233	0.945	0.946	0.204	0.210	0.958	0.956	0.336	0.341	0.887	0.884
FR	2	0.327	0.357	0.893	0.873	0.355	0.348	0.874	0.879	0.28	0.29	0.922	0.916
	3	0.717	0.723	0.488	0.479	0.359	0.363	0.872	0.870	0.494	0.49	0.756	0.761

Table 15 Model performance metrics for the HF angular-rate models of the Geyser quadrotor (h = harmonic)

	h		1	י		q				r				
Case		NRMSE		\mathbb{R}^2		NRMSE		\mathbb{R}^2		NRMSE		\mathbb{R}^2		
		Full	Test	Full	Test	Full	Test	Full	Test	Full	Test	Full	Test	
	1	0.262	0.270	0.932	0.928	0.233	0.226	0.947	0.950	0.260	0.259	0.934	0.934	
FR	2	0.334	0.320	0.889	0.898	0.385	0.424	0.852	0.821	0.313	0.320	0.902	0.898	
	3	0.509	0.514	0.740	0.735	0.515	0.535	0.736	0.714	0.640	0.658	0.590	0.567	

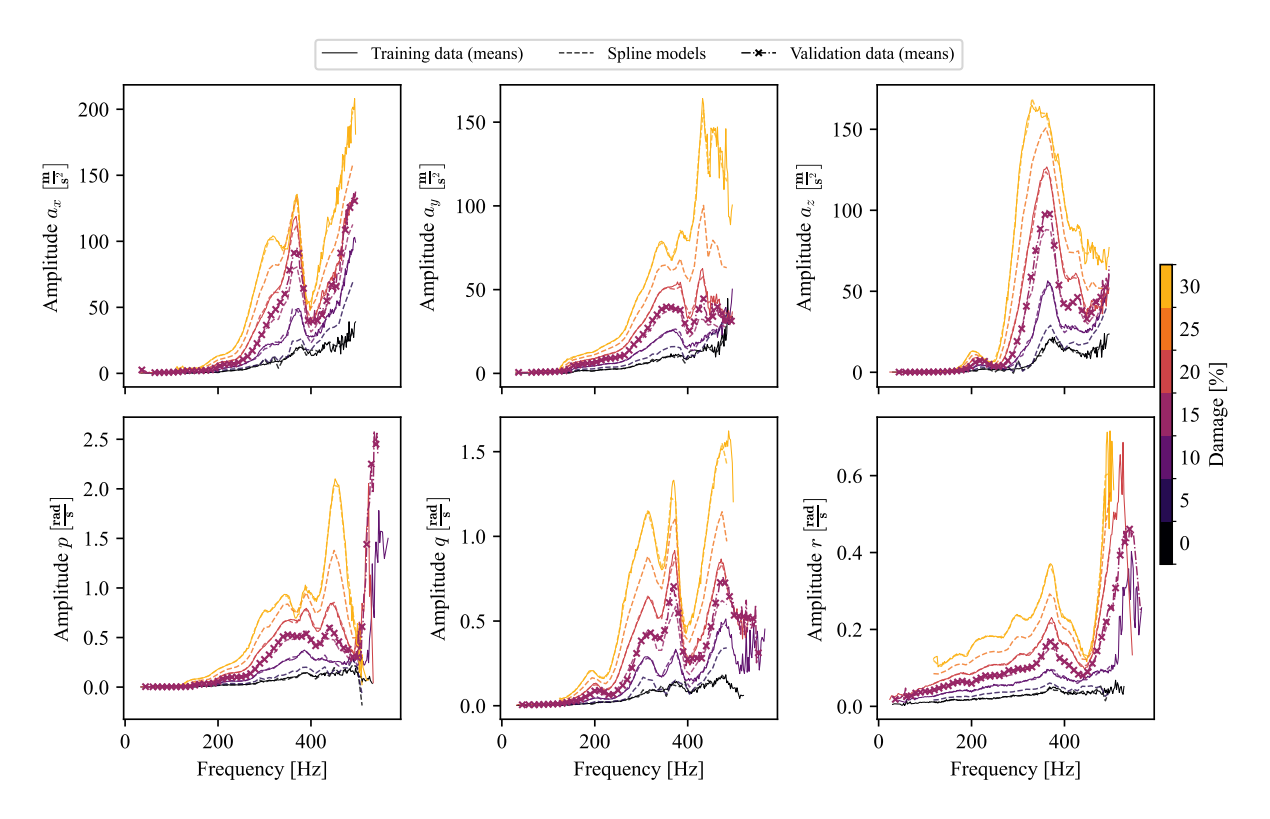


Fig. 29 Projected spline models of the Beetle for BL damage (Harmonic 1)

Table 16 Interpolation performance of the HF acceleration models

Case	h	a_x		a_y		a_z		
		NRMSE	\mathbb{R}^2	NRMSE	\mathbb{R}^2	NRMSE	\mathbb{R}^2	
15B1	1	0.475	0.774	0.516	0.734	0.291	0.915	
25FL	1	0.339	0.885	0.323	0.895	0.297	0.912	

In addition to creating models for the damage levels for which flight data was gathered, the simplex B-spline models also facilitate interpolation between the damage levels. To examine how accurately the spline models are capable of interpolating between damage levels, flight data was gathered for two damage cases: 15BL and 25FL (see Table 3). The data for these cases were not used to construct the models for the respective damage locations.

Figure 29 shows plots of the training data, spline models, and validation data for the BL damage case of the Beetle quadrotor. The validation data corresponds to a damage level of 15% and was not used when identifying the simplex B-spline model. It can be seen from the plot of each model in Fig. 29 that the spline model is actually able to approximate the data obtained for the 15% damage case quite well for all six models, even capturing the local peaks and valleys as a function of frequency.

Figure 30 shows similar plots as Fig. 29, but for FL damage, with validation data recorded at 25% damage. Again, the spline models are able to interpolate the 25% damage case quite well. However, roll rate (p) and a_y models perform relatively poorly at the higher frequency region. Models for q and r are particularly accurate.

Tables 16 and 17 respectively show the model performance metrics for the accelerometer and gyroscope models at both interpolated damage cases. While the error for the interpolated damage levels is higher than that of the damage levels used for training the model, the models still give a decent approximation. This shows the feasibility of simulating the HF behavior at several damage levels with HF models built from a discrete set of a few damage levels, which is a novel finding of this research.

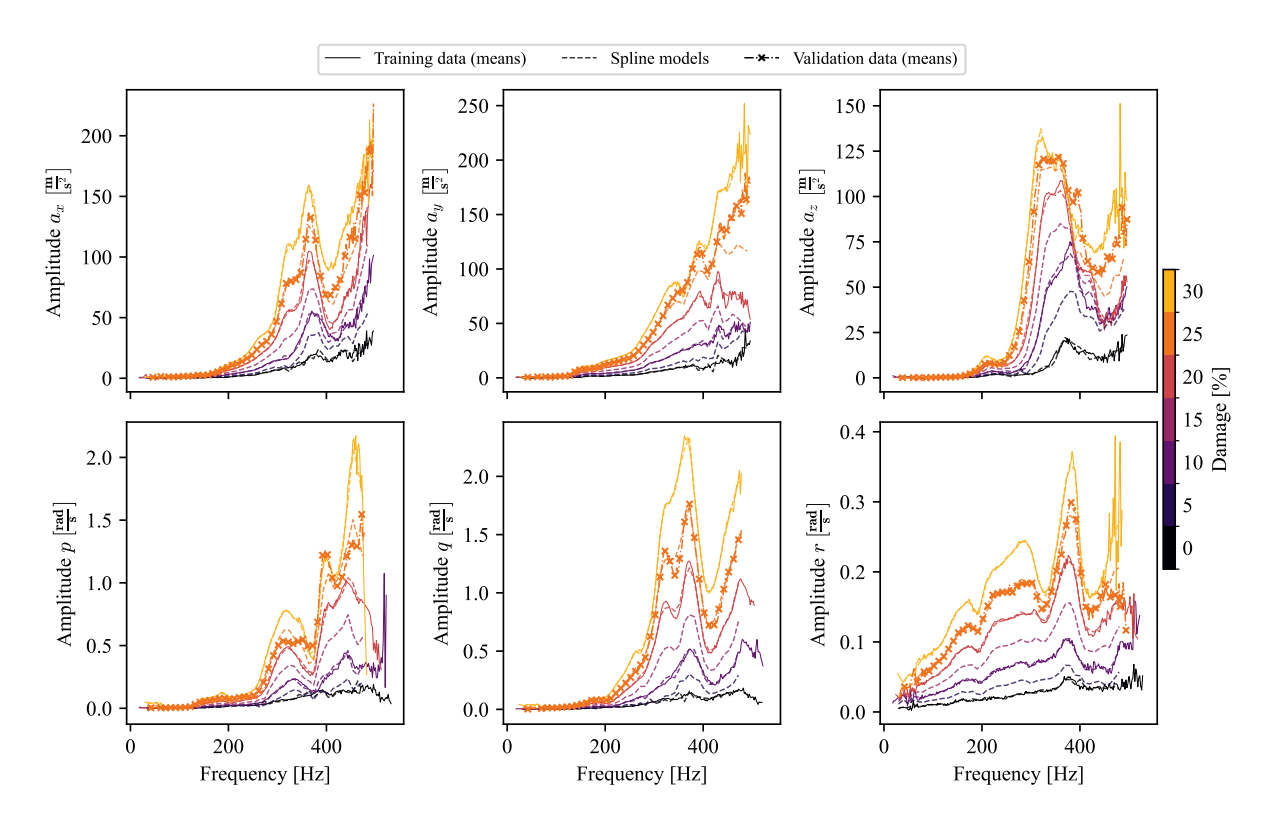


Fig. 30 Projected spline models of the Beetle for FL damage (Harmonic 1)

 $Table\ 17\quad Interpolation\ performance\ of\ the\ HF\ angular-rate\ models$

Case	h	p		q		r		
		NRMSE	R ²	NRMSE	R ²	NRMSE	R ²	
	1	0.411	0.831	0.547	0.701	0.602	0.638	
15BL	2	0.911	0.171	0.999	0.002	0.600	0.640	
	3	0.330	0.891	0.248	0.938	0.345	0.881	
	1	0.320	0.897	0.231	0.947	0.572	0.672	
25FL	2	0.581	0.662	0.619	0.617	0.474	0.776	
	3	0.377	0.858	0.661	0.564	0.483	0.767	

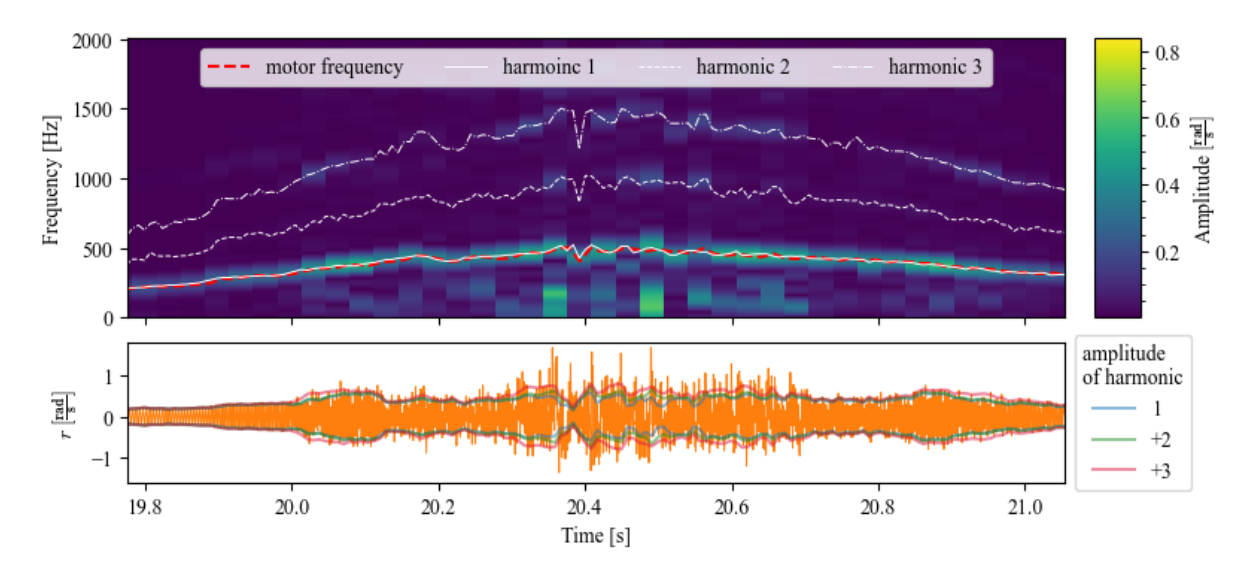


Fig. 31 A time-snippet of the yaw rate (bottom) measured by the Beetle quadrotor for damage case 30FR, and the spectrogram of this signal showing peak harmonics related to the motor frequency (top)

V. Discussion

A. Aerodynamic Models

While the aerodynamics models identified through SWR show good performance and are able to capture the effects of different combinations of blade damage and extent, they do not offer a meaningful method of interpolating between damage levels at a given damage case because of the differences in regressors chosen from one damage case to the next. The simplified fixed-regressor models identified to remedy this also did not show many meaningful relationships in the parameter values as a function of blade damage location and level. Exceptions to this were the ω_{tot}^2 regressor parameters of the F_z models, and the biases of the M_x and M_y models. However, it must be noted that the bias component of the moment models merely accounts for the constant offsets in rotor speeds created due to blade damage, and does not model the actual moments produced when maneuvers are performed.

One major reason for the lack of meaningful variations in model parameters as a function of blade damage was that, depending on the flight maneuvers performed, the training data can significantly impact the identified model parameters. Even though the system identification flights were performed manually, the variation between the maneuvers between flights was tried to be kept at a minimum by following a fixed set of pre-planned maneuvers. However, this clearly did not prove to be enough, suggesting that the only way to ensure that flight maneuvers are performed in a repeatable manner is to perform automated test flights, where pose feedback information provided by an external motion capture system is used to control the attitude and position of a quadrotor. This has been done by Sun et al. [31]. The automation of flight should also allow for more complicated maneuvers to be flown which better couple the forces and moments, unlike the largely uncoupled models presented in this paper.

The analysis of the control effectiveness regressors described in Sec. IV.A also shows the difficulty of capturing meaningful physical relationships using linear-in-the-parameters polynomial models. This was especially evident for the moment control effectiveness regressors u_p and u_q for the M_x and M_y models respectively.

B. High Frequency Models

One of the base assumptions used when building the HF models is that high-frequency accelerations and angular rates measured in each axis are comprised of a few sinusoids. Specifically, we further assume that the dominant sinusoid has a frequency equal to the rotation frequency of the damaged propeller, and only the harmonics of this frequency are dominant. While this was found to be the case for almost all IMU measurements of both the Beetle and Geyser, the yaw rate measured on the Beetle shows additional oscillations at sporadic frequencies below the motor frequency shown in Fig. 31. This generally occurs above around 250 Hz but is most dominant at frequencies above 400 Hz. The limitation of the HF modeling approach is that these sporadic effects are not captured.

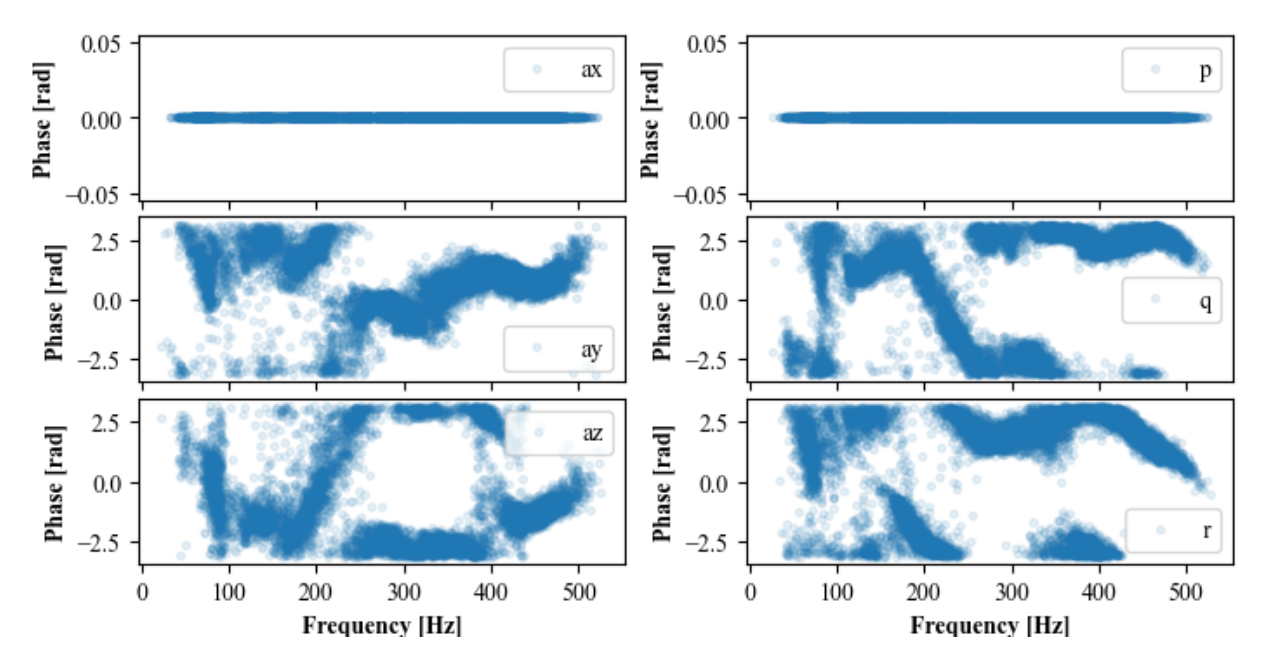


Fig. 32 Relative phases of the IMU signals of the Geyser, with damage case 30FR, obtained from the STFT of each respective signal.

While the spline-based HF models show the possibility of predicting signal amplitudes at damage levels in between the levels corresponding to the training data, a spacing of 10% damage between the training data may be too high to accurately reproduce the behavior in between the training damage levels. The spacing between damage levels also affects the number of test flights required, so a trade-off is required in terms of accuracy and experimental costs.

The phase relationships between the harmonics of each IMU axis, as well as the phase relationships between these axes, are not described by the HF models presented in this paper. This would be a useful addition, whereby phase relationships are constructed as a function of frequency in a similar manner as was done for the amplitudes in this paper. Figure 32 shows the phase information extracted from the 30FR damage case of the Geyser. Since the absolute phase depends on the actual angle made by the damaged rotor with respect to a fixed body reference – an unmeasured quantity—it is impossible to obtain the absolute phase of each IMU signal. However, at each slice of the STFT, the relative phases between signals can be computed. In Fig. 32, the phase of a_y and a_z is shown relative to that of a_x , while the phases of a_y and a_z are shown relative to that of a_z . Interestingly, there are clear patterns visible in the phase data as a function of frequency. However, the phase data obtained for damage levels below 30% are not as clear as shown here, and almost look random at 10% damage even though the IMU signals are sinusoidal for all damage cases. Therefore, before phase models can be constructed, accurate extraction of phase information should be investigated.

The simplex B-spline models presented in this paper use a fairly simple triangulation which is defined on a rectangular grid of points. To better cover the complete data space, the convex hull of the data should be used to select the simplex vertices. In terms of the number of simplices in each direction, the triangulation presented here shows good results and is recommended to be kept the same for amplitude surface modeling.

The HF models only treat frequency as the dependent variable (at a constant damage level). However, there may be a weak dependence on additional variables which affect the aerodynamic imbalances created by the damaged propeller. For example, the angle of attack of the rotor plane and airspeed may increase or decrease the effects of the HF forces and moments caused by aerodynamic imbalances which are not accounted for in the presented models. A few HF model identification flights were also conducted in the wind tunnel to see the effects of mean flow velocity on the frequency amplitude curves obtained from spectral analysis. Figure 33 shows the amplitude-frequency relationship for the same damage case, but flying at different mean airspeed. Note that the multiple curves for the '0 m/s' case are for different

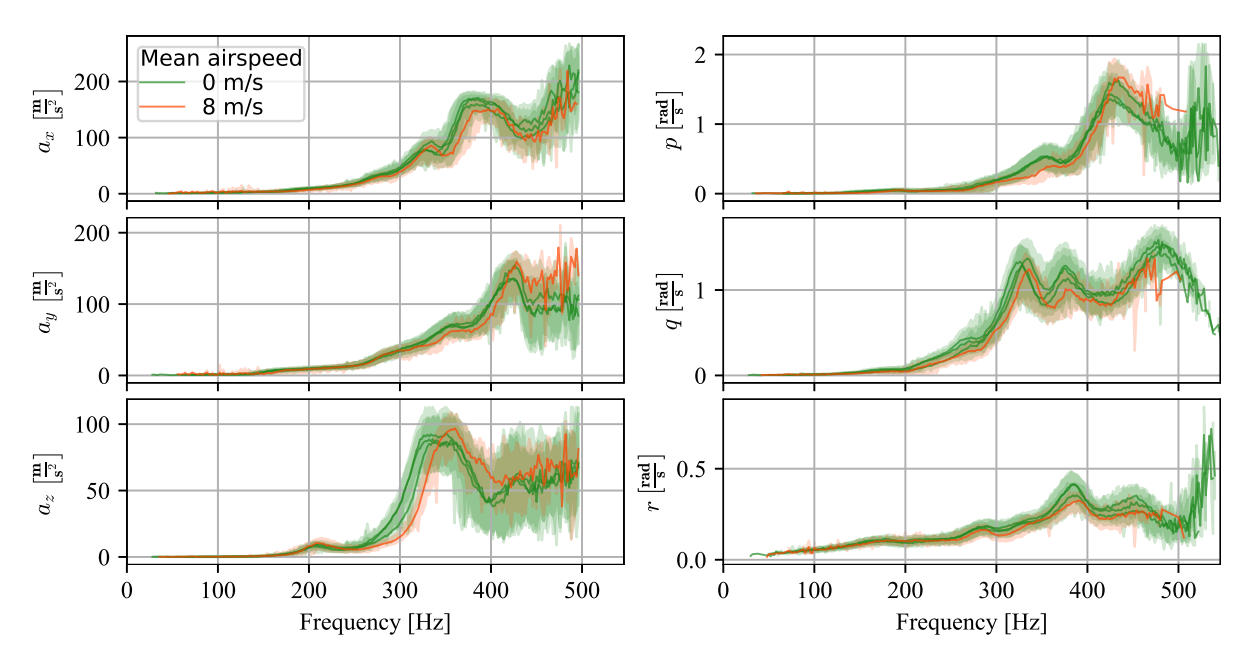


Fig. 33 First harmonic amplitude-frequency relationships of the Beetle quadrotor at varying wind speed for the same damage case (20FR)

flights. From these results, it is clear that frequency-amplitude relationships do not change drastically at different air speeds.

It is important to note here that the variations between the green curves (all corresponding to the same damage case) in Fig. 33 seem quite large compared to what was shown in Fig. 20 for various damage cases. This is likely because of minor changes in mass, and mass distribution introduces by changing the battery in between test flights. The wind tunnel tests were conducted before the model identification flights, the data from which the HF models for the Beetle are constructed. For the latter, the battery was taped onto the airframe, and all flights were conducted with the same battery (recharged without detaching from the quadrotor). Therefore, the HF behavior is found to be very sensitive to even minor changes in the way the mass is distributed on the airframe. In fact, the variation of the high airspeed curve (red) in Fig. 33 may also largely be because of the fact that the battery was changed, and not purely because of the effect of flying at a higher mean airspeed.

While the amplitude-frequency relationships are modeled using simplex B-splines in the presented HF modeling methodology, an alternative approach would be to compute the frequency response function using pole-zero models. This has the potential advantage of providing fewer and more physical parameters which describe the local peaks and valleys observed in the amplitude curves as a function of frequency. However, this would come at a cost of providing a straightforward way to interpolate between the damage levels, which is a benefit of using the spline-based models.

Finally, the HF models are only constructed for the single damage case. If linearity is assumed, then a damage case for 2 simultaneously failed rotors can be simulated by adding the respective models corresponding to only one damaged rotor. The difference in phase between the two rotors in this case can cause constructive or destructive interference between the forces and moments created by each rotor. In a simulation, the angular positions of the rotors can be simulated through time integration, and so the dual damage cases can be simulated by simply super-imposing the models identified for single propeller damage. Clipping, especially in the simulated accelerometer, should be taken into account when simulating simultaneous damage in this way.

The super-imposition of single damage models would have to be validated through HF model identification of a quadrotor with simultaneous damage to two or more propellers. However, this presents further challenges. Since the rotor speeds are generally very close throughout most of the flight, spectral analysis through the STFT-based procedure described in this paper may not be applicable because the frequency resolution would be too low to differentiate the

nearby frequencies. In this case, probably a single peak frequency corresponding to the dominant propeller can be extracted from the STFT, however, the amplitude of this peak would lump the influence of each damaged propeller. One remedy for this would be to fly maneuvers that create differences between rotor speeds such as aggressive pitch, roll, or yaw combined with simultaneous throttle punch maneuvers to ensure that the effects of imbalances in both propellers have significant amplitudes and sufficiently distanced frequencies.

C. Implications for blade damage diagnosis

Based on the aerodynamic models and high-frequency models identified for ABD, some important conclusions can also be drawn regarding the diagnosis of this damage case. High-frequency models are much more robust to the maneuvers because the primary dependence is on the (rotational) speed of the damaged rotor, while also being highly sensitive to the damage level. As shown in Sec. IV.B.1, the HF behavior differs based on damage location, at the same damage level. Bondyra et al. [17] suggest that damage cannot be localized using only a single IMU, however, the results of this study show that this is not the case. A single IMU is a sensitive enough source of information to differentiate between the same level of damage at different locations. However, this sensitivity also comes with the disadvantage that two identically manufactured quadrotors may show significantly different HF model behavior. This also calls into question the various existing diagnosis methodologies [18, 21, 37] which rely purely on IMU data.

While the aerodynamic models suggest that online identification of these models may not be a good method for diagnosing damage, certain parameters such as the bias terms of the moment models, as well the parameter for the ω_{tot}^2 regressor for F_z offer a useful diagnostic tool which may not be as sensitive to the local variations in structural properties of the airframe like the HF models. However, these parameters would not provide information about the asymmetry of the damage, unlike the HF models. It may be possible to harness the strengths of both frequency regimes to develop a robust blade diagnosis framework that is robust to small changes between airframe properties of different quadrotors but can still provide accurate estimates of the type of blade damage present on the quadrotor.

VI. Conclusion

This paper explored the process of modeling the effects of asymmetric blade damage on the dynamics of a quadrotor. It was found that the effects can be largely separated into two frequency ranges, and modeled independently for each regime. Polynomial models constructed using stepwise regression, which quantify the effects of blade damage on the aerodynamic forces and moments were analyzed. These models were found to show good performance and were demonstrated to capture the effects of blade damage. However, the variations of parameter values as a function of damage extent were sporadic for most model regressors and therefore did not facilitate interpolation between damage levels, where experimental data is not gathered. A possible way to improve the aerodynamic model interpolatability would be to perform automated, and therefore more reproducible system identification flights at each damage level.

A novel approach for modeling the high-frequency effects of asymmetric blade damage in the frequency domain was developed. A simple sinusoidal model structure was found to capture a large part of the high-frequency behavior, producing accurate models of the HF phenomena, which also facilitated reasonably accurate interpolation of the HF behavior at damage levels not used for model identification. The HF modeling approach relies purely on on-board IMU measurements, therefore facilitating online identification. Additionally, with the approach being validated on two separate quadrotor platforms, the potential for generalization is demonstrated. The findings in terms of HF behavior also provide insights regarding the diagnosis of blade damage in quadrotors, or similar platforms. Primarily, the potential strengths and weaknesses of relying purely on IMU sensors as a source of information for diagnosis are highlighted. Future research should explore the development of robust blade damage diagnosis algorithms which fuse the high sensitivity capability of the IMU with more robust information provided by certain aerodynamic model terms such as the bias terms of aerodynamic moments, as well as the ω_{tot}^2 regressor for F_z .

Appendix A: IMU properties

This section presents and compares the noise properties of the MPU6000 and ICM42605 IMUs used for gathering experimental data. Additionally, the sampling jitter properties of both IMUs are also analyzed to examine the validity of using the STFT for spectral analysis, as it assumes constant sampling times.

Figure 34 shows the noise characteristics of the MPU6000 and ICM62605 IMUs. The distributions are constructed from 30 seconds of measurement data. While the gyroscopes perform similarly for both, the accelerometer measurements of the ICM42605 have significantly lower variances than the MPU6000. However, for the purposes of high-frequency

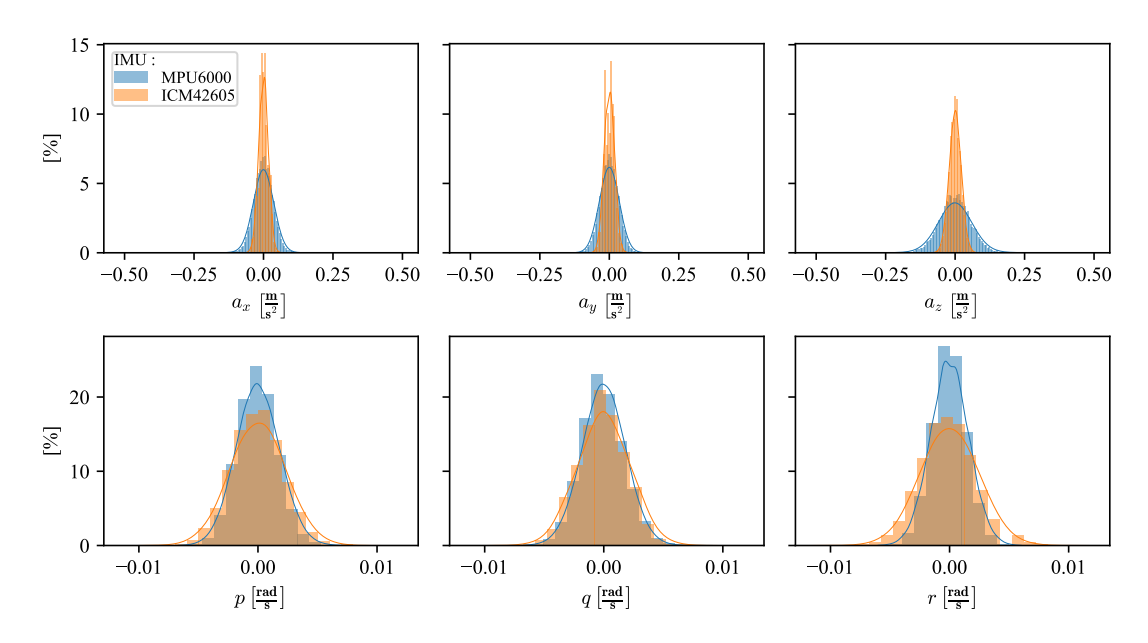


Fig. 34 Distributions of stationary noise measurements of the MPU6000 and ICM42605

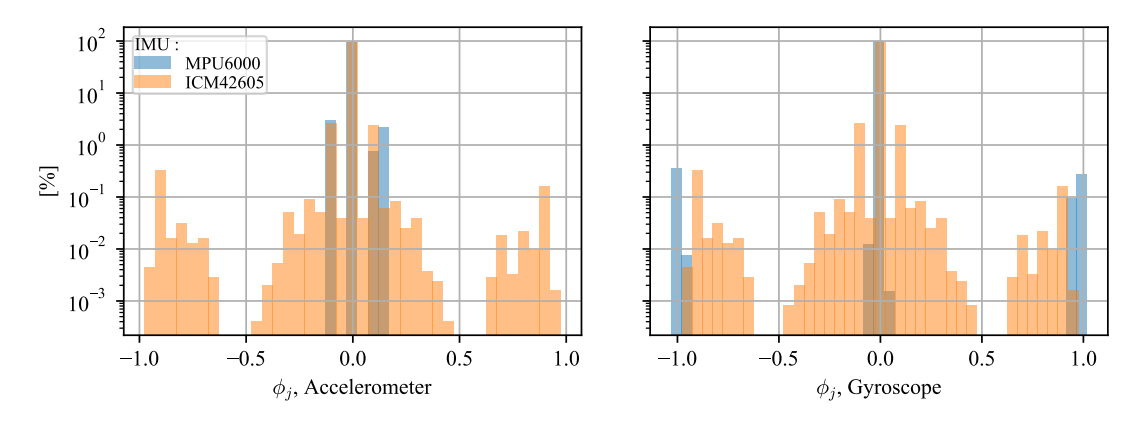


Fig. 35 Distributions of *jitter fraction* for the accelerometer (left) and gyroscope (right) measurements of the MPU6000 and ICM42605.

model identification, the signal-to-noise ratio is very high for both IMUs for both accelerometer and gyroscope measurements. The data Note that the temperature was not recorded, however, the data was gathered under similar environmental conditions. It is therefore assumed that variation in temperature did not have a significant effect on the measured noise statistics.

Apart from the measurement noise, some jitter in sampling times was also observed in the raw IMU data for both the MPU6000 and ICM42605. Here a quantity *jitter fraction* (ϕ_j) is defined as per Eq. 39, where Δt_{true} is the required sampling time, and Δt_{meas} is the measured time difference between two consecutive samples. Figure 35 shows the distributions of phi_j for the accelerometer and gyroscope measurements. The raw IMU data in px4 is logged independently for the accelerometer and gyroscope, while the axes of both sensors are logged simultaneously. While there is some amount of sampling jitter, a vast majority of the measurements (>92%) show consistent sampling periods.

$$\phi_j = \frac{\Delta t_{true} - \Delta t_{meas}}{\Delta t_{true}} \tag{39}$$

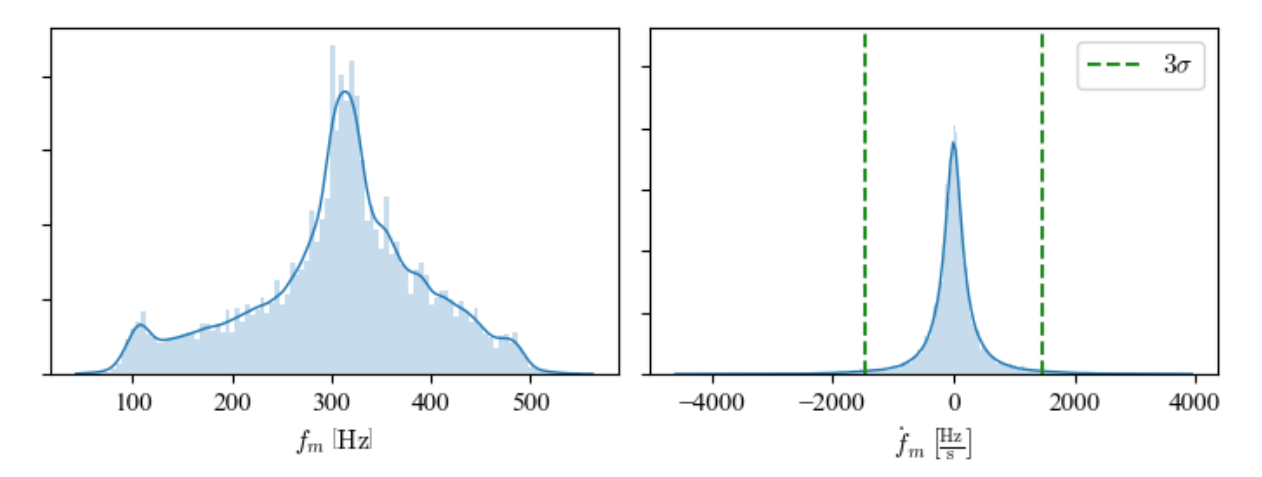


Fig. 36 Distribution of motor frequencies (left) and their derivative (right) constructed from data gathered from all Beetle test flights

Appendix B: Optimal STFT parameters based on signal properties

As discussed in the paper, the outputs of the STFT are highly sensitive to the choice parameters n_s and $n_{\rm fft}$, which are linked to the f_s , f_r , and f_{r_e} via Eq. 28 and 29 respectively. Intuitively, it is appropriate to assume that the choice of these parameters is influenced by the degree of non-stationarity of the sinusoidal signal to be analyzed, which can be formally defined as the maximum derivative of the frequency of the sinusoidal signal \dot{f}_{max} .

For the purpose of building the HF models presented in this paper, the sinusoidal IMU signals are analyzed using the STFT. Because the frequency of these signals is directly related to the rotational frequency of the damaged propeller, it is useful to study the properties of the motor frequencies. Figure 36 shows the distributions of motor frequencies, and the derivatives of these frequencies, computed from the data of all the test cases presented in Table 3. We see that the sinusoidal signals measured by the IMU can have changes in frequency at more than 4000 Hz/s, however, very rare. A value of 2500 Hz/s for \hat{f}_{max} encompasses a large amount of the observed non-stationarity.

To determine a good choice for the parameters f_r and f_{re} , a numerical study was conducted. For this, artificial non-stationary sinusoidal signals are generated using Eq. 41 where the frequency of the signal is given by Eq. 40. The sampling rate of the test signal is chosen as 4 kHz, with a length of 20k samples, and the maximum f_{max} and minimum frequency f_{min} are chosen to be 1800 Hz and 100 Hz respectively. Then, the test signal is analyzed through the STFT at several combinations of f_r and frequency factor ψ_f (Eq. 42). The relative RMSE of the STFT-derived amplitude and frequency are computed, for each pair of f_r and ψ_f . Figure 37 shows the result of this process. It is clear from the results that a naive choice of parameters can lead to a very bad estimate of amplitude especially.

$$f(t) = \frac{f_{max} - f_{min}}{2} \sin\left(2\frac{\dot{f}_{max}}{f_{max} - f_{min}}t\right) + \frac{f_{max} - f_{min}}{2}$$
(40)

$$y(t) = \sin(2\pi f(t)) \tag{41}$$

$$\psi_f = \frac{f_{r_e}}{f_r} \tag{42}$$

While several good options for f_r and ψ_f are available, values of 60 Hz and 1/30 were chosen for each parameter respectively. This choice of parameters results in a very low error in both frequency (<2%) and amplitude (<5%) estimates derived from the STFT. Based on the definition of ψ_f , the chosen effective frequency resolution has a value of 2 Hz.

Acknowledgments

B.Saify would like to thank the member of the VIDI research group for providing meaningful insights, which allowed for better research.

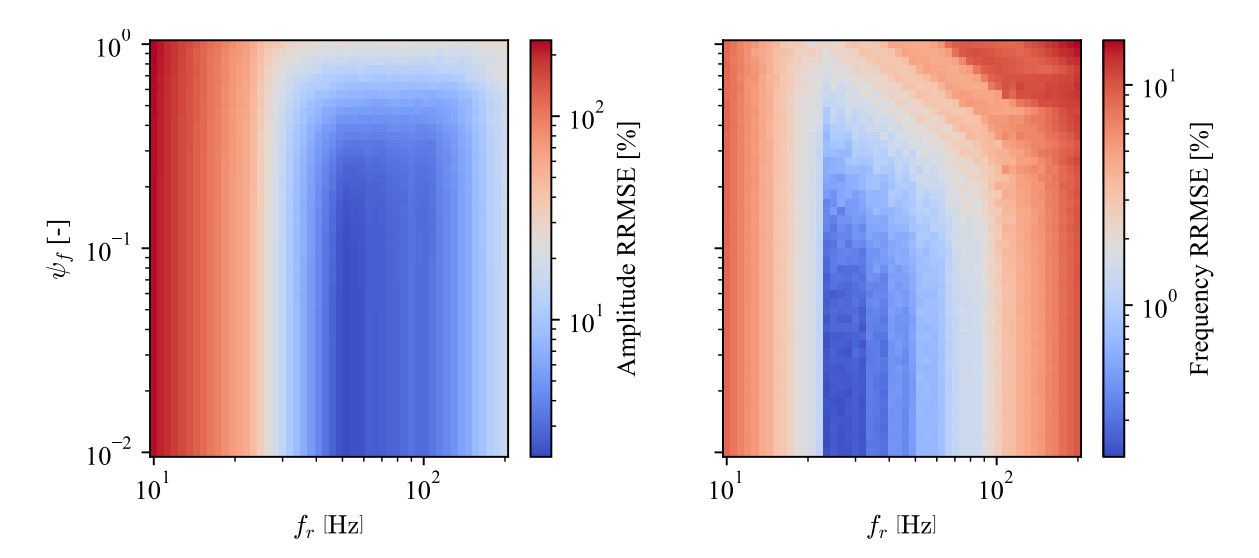


Fig. 37 Variation of STFT derived amplitude and frequency RRMSE a function of the frequency resolution f_r and the frequency factor ψ_f

- [1] Cummings, A. R., McKee, A., Kulkarni, K., and Markandey, N., "The rise of UAVs," *Photogrammetric Engineering & Remote Sensing*, Vol. 83, No. 4, 2017, pp. 317–325.
- [2] Sun, S., Sijbers, L., Wang, X., and De Visser, C., "High-Speed Flight of Quadrotor Despite Loss of Single Rotor," *IEEE Robotics and Automation Letters*, Vol. 3, No. 4, 2018, pp. 3201–3207. https://doi.org/10.1109/LRA.2018.2851028.
- [3] Sun, S., Wang, X., Chu, Q., and de Visser, C., "Incremental nonlinear fault-tolerant control of a quadrotor with complete loss of two opposing rotors," *IEEE Transactions on Robotics*, Vol. 37, No. 1, 2020, pp. 116–130.
- [4] Mueller, M. W., and D'Andrea, R., "Stability and control of a quadrocopter despite the complete loss of one, two, or three propellers," 2014 IEEE international conference on robotics and automation (ICRA), IEEE, 2014, pp. 45–52.
- [5] Zhong, Y., Zhang, Y., Zhang, W., Zuo, J., and Zhan, H., "Robust actuator fault detection and diagnosis for a quadrotor UAV with external disturbances," *IEEE Access*, Vol. 6, 2018, pp. 48169–48180.
- [6] Amoozgar, M. H., Chamseddine, A., and Zhang, Y., "Experimental test of a two-stage Kalman filter for actuator fault detection and diagnosis of an unmanned quadrotor helicopter," *Journal of Intelligent & Robotic Systems*, Vol. 70, No. 1, 2013, pp. 107–117.
- [7] Sun, S., Schilder, R., and de Visser, C. C., "Identification of quadrotor aerodynamic model from high speed flight data," 2018 AIAA Atmospheric Flight Mechanics Conference, 2018, p. 0523.
- [8] Sun, S., "Quadrotor Fault Tolerant Flight Control and Aerodynamic Model Identification," Ph.D. thesis, Delft University of Technology, 2020. https://doi.org/10.4233/uuid:f0bdac3d-376d-4b24-9241-3a1e35731373.
- [9] Hoffmann, G. M., Huang, H., Waslander, S. L., and Tomlin, C. J., "Quadrotor helicopter flight dynamics and control: Theory and experiment," *Collection of Technical Papers - AIAA Guidance, Navigation, and Control Conference* 2007, Vol. 2, 2007, pp. 1670–1689. https://doi.org/10.2514/6.2007-6461.
- [10] Sun, S., and de Visser, C. C., "Quadrotor safe flight envelope prediction in the high-speed regime: A Monte-Carlo approach," *AIAA Scitech 2019 Forum*, 2019, p. 0948.
- [11] Avram, R. C., Zhang, X., and Muse, J., "Quadrotor sensor fault diagnosis with experimental results," *Journal of Intelligent & Robotic Systems*, Vol. 86, No. 1, 2017, pp. 115–137.
- [12] Guo, J., Qi, J., and Wu, C., "Robust fault diagnosis and fault-tolerant control for nonlinear quadrotor unmanned aerial vehicle system with unknown actuator faults," *International Journal of Advanced Robotic Systems*, Vol. 18, No. 2, 2021. https://doi.org/10.1177/17298814211002734.

- [13] Guo, K., Zhang, W., Zhu, Y., Jia, J., Yu, X., and Zhang, Y., "Safety Control for Quadrotor UAV against Ground Effect and Blade Damage," *IEEE Transactions on Industrial Electronics*, 2022. https://doi.org/10.1109/TIE.2022.3140494.
- [14] Asadi, D., Ahmadi, K., and Nabavi, S. Y., "Fault-tolerant Trajectory Tracking Control of a Quadcopter in Presence of a Motor Fault," *International Journal of Aeronautical and Space Sciences*, Vol. 23, No. 1, 2022, pp. 129–142. https://doi.org/10.1007/s42405-021-00412-9.
- [15] Sadeghzadeh, I., Mehta, A., and Zhang, Y., "Fault/damage tolerant control of a quadrotor helicopter UAV using model reference adaptive control and gain-scheduled PID," *AIAA Guidance, Navigation, and Control Conference*, 2011, p. 6716.
- [16] Guzmán-Rabasa, J. A., López-Estrada, F. R., González-Contreras, B. M., Valencia-Palomo, G., Chadli, M., and Pérez-Patricio, M., "Actuator fault detection and isolation on a quadrotor unmanned aerial vehicle modeled as a linear parameter-varying system," *Measurement and Control (United Kingdom)*, Vol. 52, No. 9-10, 2019, pp. 1228–1239. https://doi.org/10.1177/0020294018824764.
- [17] Bondyra, A., Gasior, P., Gardecki, S., and Kasiński, A., "Fault diagnosis and condition monitoring of UAV rotor using signal processing," 2017 Signal Processing: Algorithms, Architectures, Arrangements, and Applications (SPA), IEEE, 2017, pp. 233–238.
- [18] Yang, P., Wen, C., Geng, H., and Liu, P., "Intelligent fault diagnosis method for blade damage of quad-rotor uav based on stacked pruning sparse denoising autoencoder and convolutional neural network," *Machines*, Vol. 9, No. 12, 2021. https://doi.org/10.3390/machines9120360.
- [19] Brown, J. M., Coffey, J. A., Harvey, D., and Thayer, J. M., "Characterization and prognosis of multirotor failures," *Structural Health Monitoring and Damage Detection, Volume 7*, Springer, 2015, pp. 157–173.
- [20] Ghalamchi, B., Jia, Z., and Mueller, M. W., "Real-Time Vibration-Based Propeller Fault Diagnosis for Multicopters," IEEE/ASME Transactions on Mechatronics, Vol. 25, No. 1, 2020, pp. 395–405. https://doi.org/10.1109/TMECH.2019.2947250.
- [21] Du, C., Zhang, X., Zhong, R., Li, F., Yu, F., Rong, Y., and Gong, Y., "Unmanned aerial vehicle rotor fault diagnosis based on interval sampling reconstruction of vibration signals and a one-dimensional convolutional neural network deep learning method," *Measurement Science and Technology*, Vol. 33, No. 6, 2022. https://doi.org/10.1088/1361-6501/ac491e.
- [22] Liu, W., Chen, Z., and Zheng, M., "An audio-based fault diagnosis method for quadrotors using convolutional neural network and transfer learning," 2020 American Control Conference (ACC), IEEE, 2020, pp. 1367–1372.
- [23] Jiang, Y., Zhiyao, Z., Haoxiang, L., and Quan, Q., "Fault detection and identification for quadrotor based on airframe vibration signals: a data-driven method," 2015 34th chinese control conference (ccc), IEEE, 2015, pp. 6356–6361.
- [24] Smeur, E. J., Chu, Q., and De Croon, G. C., "Adaptive incremental nonlinear dynamic inversion for attitude control of micro air vehicles," *Journal of Guidance, Control, and Dynamics*, Vol. 39, No. 3, 2016, pp. 450–461.
- [25] Mahony, R., Kumar, V., and Corke, P., "Multirotor aerial vehicles: Modeling, estimation, and control of quadrotor," *IEEE Robotics and Automation Magazine*, Vol. 19, No. 3, 2012, pp. 20–32. https://doi.org/10.1109/MRA.2012.2206474.
- [26] Pounds, P., Mahony, R., and Corke, P., "Modelling and control of a quad-rotor robot," *Proceedings of the 2006 Australasian Conference on Robotics and Automation*, Australian Robotics and Automation Association (ARAA), 2006, pp. 1–10.
- [27] Bangura, M., Mahony, R., et al., "Nonlinear dynamic modeling for high performance control of a quadrotor," 2012.
- [28] Powers, C., Mellinger, D., Kushleyev, A., Kothmann, B., and Kumar, V., "Influence of aerodynamics and proximity effects in quadrotor flight," *Experimental robotics*, Springer, 2013, pp. 289–302.
- [29] Sun, S., De Visser, C. C., and Chu, Q., "Quadrotor gray-box model identification from high-speed flight data," *Journal of Aircraft*, Vol. 56, American Institute of Aeronautics and Astronautics Inc., 2019, pp. 645–661. https://doi.org/10.2514/1.C035135.
- [30] Prouty, R. W., Helicopter performance, stability, and Control, Krieger Publishing Company, 2002.
- [31] Sun, S., and de Visser, C., "Aerodynamic Model Identification of a Quadrotor Subjected to Rotor Failures in the High-Speed Flight Regime," *IEEE Robotics and Automation Letters*, Vol. 4, No. 4, 2019, pp. 3868–3875. https://doi.org/10.1109/lra.2019.2928758.
- [32] Morelli, E. A., and Klein, V., Aircraft system identification: theory and practice, Vol. 2, Sunflyte Enterprises Williamsburg, VA, 2016.

- [33] Ribeiro, M. I., "Kalman and extended kalman filters: Concept, derivation and properties," *Institute for Systems and Robotics*, Vol. 43, 2004, p. 46.
- [34] Jones, E., Oliphant, T., Peterson, P., et al., "SciPy: Open source scientific tools for Python,", 2001-. URL http://www.scipy.org/.
- [35] de Visser, C. C., Chu, Q., and Mulder, J., "A new approach to linear regression with multivariate splines," *Automatica*, Vol. 45, No. 12, 2009, pp. 2903–2909.
- [36] de Visser, C., Mulder, J., and Chu, Q., "Global nonlinear aerodynamic model identification with multivariate splines," *AIAA* atmospheric flight mechanics conference, 2009, p. 5726.
- [37] Bondyra, A., Gasior, P., Gardecki, S., and Kasinski, A., "Development of the Sensory Network for the Vibration-based Fault Detection and Isolation in the Multirotor UAV Propulsion System," *ICINCO 2018 - Proceedings of the 15th International Conference on Informatics in Control, Automation and Robotics*, Vol. 2, SciTePress, 2018, pp. 102–109. https://doi.org/10.5220/0006846801020109.

Part III Preliminary Report

1

Introduction

Small unmanned aerial vehicles (UAVs) have become increasingly popular in both commercial and research aspects [13]. These vehicles offer autonomy and flexibility which opens up many areas of applicability including transportation of goods, surveying, and infrastructure inspection to name a few. The quadrotor is the most popular UAV configuration, which has been heavily researched.

Like any engineered system, quadrotors are susceptible to partial or complete failures which can result in crashes. Therefore, a large amount of research has focused on fault detection and fault-tolerant control [49, 35, 1, 60] of these vehicles. One area of research which aims to improve the safety of aircraft such as UAVs is Safe Flight Envelope (SFE) estimation and protection [52, 58, 30, 31]. When an aircraft sustains damage or a fault, the safely operable part of the state space is reduced. Without knowledge of this reduced region of safe operation, Loss of Control (LOC) can occur [36, 52, 58, 30, 31].

The computation of SFEs requires dynamic system models. In quadrotors, failure scenarios such as partial and complete loss of rotor effectiveness have been researched, and a dynamic model has been obtained for a quadrotor which has sustained complete loss of one propeller [48]. However, the failure scenario of propeller blade damage has not been modelled. Most of the research effort focuses on the detection and diagnosis of propeller blade damage [18, 21, 26, 17], or on fault-tolerant control [28, 12, 20]. Thus, an important gap in the knowledge of quadrotors is found.

This literature report presents in detail the findings of a literature study conducted on quadrotors, quadrotor model identification, and quadrotors afflicted with propeller blade damage. First, the quadrotor vehicle is formally described and a first-principles dynamic model is presented in Chapter 2. An overview of the literature found regarding propeller blade damage of quadrotors is presented in Chapter 3. A short description of SFEs is provided in Chapter 4 along with an argument for why model identification for a quadrotor with blade damage is relevant. System identification techniques for quadrotors are discussed in Chapter 5, followed by a conclusion and research proposal in Chapter 6.

Quadrotor Dynamic Model

The quadrotor is a complex dynamical system. There are several forces and moments which act on a quadrotor type UAV aircraft in flight, such as gravity, propulsive forces and moments, gyroscopic effects, and aerodynamic forces. These forces effect the dynamics of a quadrotor, and reliable prediction of these forces enables accurate simulations of these vehicles. This chapter gives an overview of a commonly used dynamic model of a quadrotor which is valid in hovering and low speed flight. First, the important reference frames are introduced in Section 2.1, followed by a simple model in Section 2.2.

2.1. Reference Frames

The variables which define the state of an aircraft in flight are its velocity, attitude, angular velocity and position. These vector quantities are represented with respect to coordinate frames. Thus, it is important to have concrete definitions of the reference frames, and how vector quantities can be transformed between these frames.

It is often convenient to define forces created by the quadrotor -such as the thrust created by each of the rotors- in a reference frame which has a fixed orientation with respect to the body of the quadrotor. However, to define the dynamic motion of the quadrotor using Newton's laws of motion, an inertial frame is required.

The inertial frame \mathcal{F}^I is generally defined fixed to the ground, with a North-East-Down orientation. The x-axis of this frame points towards the north poles, the z-axis points towards the center of the Earth and the y-axis completes the right-handed coordinate system.

The body frame \mathcal{F}^B of a quadrotor is often defined in two unique ways in literature. For both these frames, it is assumed that the four rotors lie in the same plane, and that their centers of rotation form a rectangle. The center of mass is taken as the origin and is assumed to lie on an axis perpendicular to the plane of rotation of all the rotors, and which passes through the intersection point of lines connecting diagonally opposite rotors. One representation of the body fixed frame is defined for square quadcopter configurations where the origin is located at the intersection of the lines connecting opposite rotor axes, the x-axis points towards one of the arms, the z axis points downwards (perpendicular to the plane containing the rotors), and the y axis completes the right-handed coordinate system.

The alternative representation of the body-fixed reference frame is one where the x-axis lies parallel to the plane of the 4 rotors, the projection onto which bisects the lines connecting two adjacent rotors. The z-axis points downwards perpendicular to the plane containing the rotors, and the y-axis completes the right-handed coordinate system. The two rotors which are located in the direction of the body x-axis can be labelled as the 'front' rotors, with the other two naturally being the 'rear' rotors. The advantage of this body reference frame is that independent control of rotation about each axis is more intuitive. For example, to pitch down, the aft rotors increase thrust and their opposite angular velocities cancel out any yawing moment. Similarly, rolling to the right is achieved by increasing the speeds of the left two rotors equally. Again, the yawing torque of each rotor is cancelled because they spin in opposite directions. The alternate representation of the body frame is shown in Figure 2.1 and is used for the remainder of this chapter.

With the reference frames clearly defined, the rotation of one frame with respect to the other can be represented using Euler angles. These are the pitch (θ) , roll (ϕ) and yaw (ψ) angles and the describe the orientation of the

2.2. Dynamic Model 48

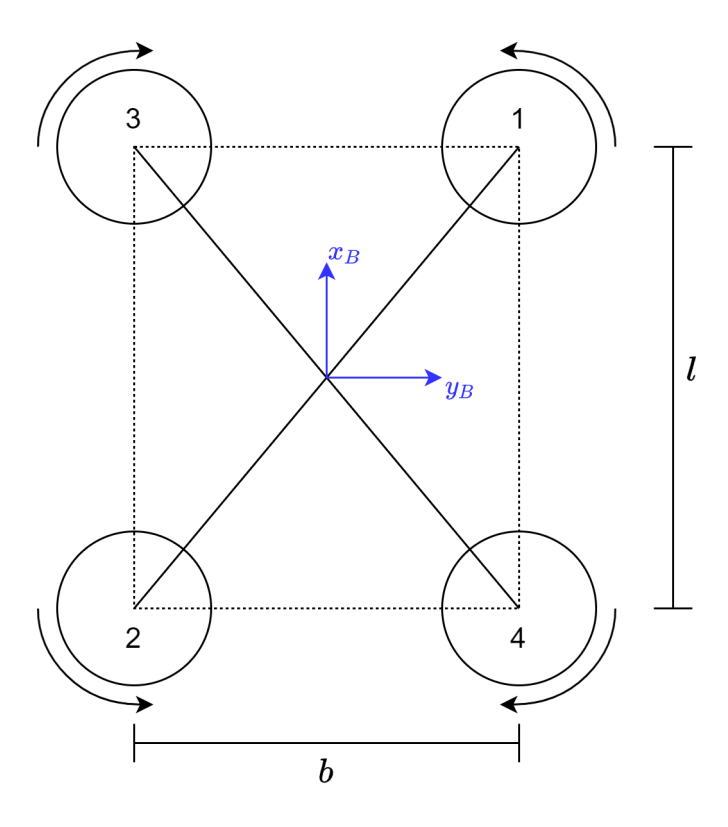


Figure 2.1: Representation of a quadrotor (z_B axis points into the page)

body-fixed reference to the inertial frame, with the order of rotation being yaw, pitch and roll (which is commonly used in the field of aerospace engineering). The matrix used to transform a vector in the inertial frame to the body frame is given by Equation 2.1. The inverse transformation of a vector in the body frame to the inertial frame is computed using the transpose of the matrix, which is equal to the inverse since the matrix is orthonormal[6].

$$\mathbf{R}_{BI} = \begin{bmatrix} \cos\theta\cos\psi & \cos\theta\sin\psi & -\sin\theta \\ \sin\varphi\sin\theta\cos\psi \\ -\cos\varphi\sin\psi & +\cos\varphi\cos\psi \\ \cos\varphi\sin\theta\cos\psi \\ +\sin\varphi\sin\psi & +\sin\varphi\sin\psi \\ -\sin\varphi\cos\psi & -\sin\varphi\cos\psi \\ \end{bmatrix} \cos\varphi\cos\theta$$
(2.1)

2.2. Dynamic Model

A commonly used first principles model for the dynamics of quadrotor drone are presented in this section. The model is applicable in hovering flight, and small deviations around this flight condition [45]. A few key assumptions are highlighted before proceeding:

- The Earth is assumed flat. The curvature will cause significant effects when the displacements are of the order of a kilometer. However, for quadrotor UAVs, generally the flights are within line of sight, making this assumption valid.
- The rotation of the Earth is ignored. The rotation of the earth means that the ground can no longer be considered an inertial frame. However, the effect is small enough that is often ignored for modelling small aircraft
- The body of the quadrotor is considered rigid, which is equivalent to assuming a constant inertia tensor.
- The mass is assumed to be constant. For battery-powered aircraft, this is indeed the case.

The dynamics of an aircraft can be split into the linear and rotational dynamics. These are governed by Newton's laws of motion, and their rotational analogues. The linear velocity derivatives $\dot{v}_B = \begin{bmatrix} \dot{u} \ \dot{v} \ \dot{w} \end{bmatrix}^T$ are computed in the body reference frame, which are transformed to and integrated in the inertial frame to propagate

2.2. Dynamic Model 49

the inertial position vector $\dot{\boldsymbol{p}}_I = [\dot{x}_I \, \dot{y}_I \, \dot{z}_I]^T$. Similarly, the angular velocity derivatives $\dot{\boldsymbol{\omega}}_B = [\dot{p} \, \dot{q} \, \dot{r}]^T$ are computed in the body reference frame, and integrated in the inertial reference frame to compute the attitude $\boldsymbol{q} = [\phi \, \theta \, \psi]^T$ of the aircraft.

The complete dynamic and kinematic equations of motion for an aircraft are given by the system of equations given below. Equation 2.2 and Equation 2.3 describe the linear equations of motion and Equation 2.4 and Equation 2.5 describe the rotational equations of motion. Since the linear accelerations (\dot{v}_B) and angular accelerations (\dot{v}_B) are computed in the body frame, additional terms appear in Equation 2.3 and Equation 2.5 to account for the angular velocity of the body reference frame with respect to the inertial frame. In order to transform the body angular rates to the attitude derivatives (\dot{q}) , the matrix K_{IB} computed using Equation 2.6 is used in Equation 2.4.

$$\dot{\boldsymbol{p}}_I = \boldsymbol{R}_{IB} \boldsymbol{v}_B \tag{2.2}$$

$$\dot{\boldsymbol{v}}_B = \frac{1}{m} \boldsymbol{F}_B + \boldsymbol{\omega}_B \times \boldsymbol{v}_B \tag{2.3}$$

$$\dot{q} = K_{IB}\omega_B \tag{2.4}$$

$$\dot{\boldsymbol{\omega}}_{B} = \boldsymbol{I}^{-1} \left(\boldsymbol{M}_{B} - \boldsymbol{\omega}_{B} \times \boldsymbol{I} \boldsymbol{\omega}_{B} \right) \tag{2.5}$$

$$\boldsymbol{K}_{IB} = \begin{bmatrix} 1 & \sin\phi \tan\theta & \cos\phi \tan\theta \\ 0 & \cos\phi & -\sin\phi \\ 0 & \sin\phi \sec\theta & \cos\phi \sec\theta \end{bmatrix}$$
(2.6)

The total external forces and moments are lumped into (F_B) and (M_B) respectively. External forces are decomposed into gravity forces $(F_{B,g})$, propulsive forces $(F_{B,p})$ and aerodynamic forces $(F_{B,a})$. Similarly, the external moments comprise of the propulsive $(M_{B,p})$ and aerodynamic $(M_{B,a})$ moments. The leading subscript (B) indicates that the forces and moments are computed in the body frame, while the latter subscript indicates the type of force or moment. Since the moments are computed around the center of mass, there is no moment due to gravity.

$$\boldsymbol{F}_{B} = \boldsymbol{F}_{B,q} + \boldsymbol{F}_{B,p} + \boldsymbol{F}_{B,a} \tag{2.7}$$

$$M_B = M_{B,p} + M_{B,a} (2.8)$$

The gravitational force is computed in the body frame by transforming the gravitational acceleration vector in the inertial reference frame to the body frame using the matrix in Equation 2.1 and multiplying by the mass (m) of the vehicle.

$$\boldsymbol{F}_{B,g} = m\boldsymbol{R}_{BI} \begin{bmatrix} 0 \\ 0 \\ g \end{bmatrix} \tag{2.9}$$

Propulsive forces and moments

A commonly used propulsion model for quadrotors models the thrust and axial aerodynamic torque of each rotor as directly proportional to the square of the angular velocity of the rotor. The thrust of rotor i is computed using Equation 2.10, and torque is computed using Equation 2.11 where Ω_i is the angular velocity of rotor i. The aerodynamic torque acts along the z body axis, and has a sign opposite to the sign of the rotor spin. The constants of proportionality k and d depend on the density of the air and the geometry of the rotor blades [45, 39].

The total thrust force in the body frame is computed using Equation 2.12 with the assumption that the axes of all rotors are parallel to the z body axis. The moment vector is computed using Equation 2.13 where the rotor indices correspond to those in Figure 2.1, b is the distance between the left and right rotors, and 1 is the distance between the forward and aft rotors.

$$T_i = k\Omega_i^2 \tag{2.10}$$

$$Q_i = -d\Omega_i^2 \operatorname{sign}(\Omega_i) \tag{2.11}$$

$$\boldsymbol{F}_{B,p} = \begin{bmatrix} 0 \\ 0 \\ -k \sum \Omega_i^2 \end{bmatrix}$$
 (2.12)

$$\mathbf{M}_{B,p} = \begin{bmatrix} \frac{b}{2}k((\Omega_2^2 + \Omega_3^2) - (\Omega_1^2 + \Omega_4^2)) \\ \frac{l}{2}k((\Omega_1^2 + \Omega_3^2) - (\Omega_2^2 + \Omega_4^2)) \\ -d\sum \Omega_i^2 \text{sign}(\Omega_i) \end{bmatrix}$$
(2.13)

In the simply model, the aerodynamics forces $(F_{B,a})$ and moments $(M_{B,a})$ are not considered. The forces and moments arise from non-propulsion elements such as the body of the drone which houses the flight computer and avionics, and the arms linking the body to the motors. The effects of these contributions are not significant in low-speed flight and are thus reasonably omitted.

Gyroscopic effects

Due to the relatively high angular velocities of rotors of a quadrotor in flight, gyroscopic effects are present and these contribute to the moment acting on the quadrotor body. Since the rotors are assumed to rotate in the z body axis, the gyroscopic rigidity phenomenon affects the x and y-axis moments. The z-axis moment is generated by the angular accelerations of the rotors. The gyroscopic effects are quantified by Equation 2.14 where $I_{r,z}$ is the polar moment of inertia of each rotor. Since the gyroscopic moments arise from the only the propulsion elements, these can also be categorised as propulsive moments [45].

$$\mathbf{M}_{B,r} = \begin{bmatrix} qI_{r,z}(\Omega_1 + \Omega_2 - \Omega_3 - \Omega_4) \\ pI_{r,z}(-\Omega_1 - \Omega_2 + \Omega_3 + \Omega_4) \\ I_{r,z}(\dot{\Omega}_1 + \dot{\Omega}_2 - \dot{\Omega}_3 - \dot{\Omega}_4) \end{bmatrix}$$
(2.14)

2.3. Aerodynamic Effects

The propulsion model discussed above is valid only near hovering conditions and ignores phenomena that are observed in high speed flight. In general, the additional aerodynamic effects cause additional forces and moments to act on the rotor which have a significant effect on the dynamics of a quadrotor. Two important such phenomena are that of thrust variance and blade flapping [22, 32] which are discussed in this section.

Thrust Variance

The relation for calculating the thrust of a rotor given by Equation 2.10 is derived from actuator disk momentum theory for hovering flight [32]. However, this relation is not valid in the case of ascending, descending, and high-speed translational flight.

The general expression for the thrust produced by a rotor as a function of the airspeed V and angle of attack α of a rotor, derived from momentum theory, is given by Equation 2.15. Another expression for thrust is obtained by analysing a rotor using Blade Element Theory which results in Equation 2.16 where a is the lift curve slope of the airfoil comprising the blades of the rotor, b is the number of blades, c is the blade chord, b is the radius of the rotor and b_{tip} is the pitch angle at the rotor blade tip [39].

Given an airspeed and angle of attack, the induced velocity can be found by solving a quartic equation obtained by equating the two expressions for the thrust. Then, either of the equations can be used to compute the actual thrust [39].

$$T = 2\rho A v_i \sqrt{V^2 + 2V v_i \sin \alpha + v_i^2}$$
(2.15)

$$T = \frac{\rho a b c \omega^2 R^3}{2} \left(\frac{\theta}{3} + \frac{V^2 \cos^2 \alpha \theta}{2\omega^2 R^2} + \frac{V \sin \alpha + v}{2\omega R} \right)$$
 (2.16)

Experiments conducted by Powers et al. [39] investigated the effects of velocity and angle of attack on the thrust produced by propellers. Their results show that there is a decrease in thrust with increasing airspeed,

however, the effects are most pronounced at high angles of attack (climbing flight) compared to low angles of attack (translational flight). Similar experiments were conducted previously by Hoffman et al. [22] where they conclude that at low speed, the variation of the angle of attack has a negligible effect on the thrust produced with a constant power input which is equivalent to low thrust variance with flight speed at high angles of attack. Thus the two studies agree with each other. The main conclusion drawn is thus that translational flight at flight speeds in the range of even 3-4 m/s encounters significant thrust variance.

For a quadrotor in flight, depending on the maneuver being flown, each rotor will have a local airspeed and angle of attack because of the angular velocity of the quadrotor. However, the local effects at each rotor can be accounted for by computing the angles of attack and airspeed for each rotor using kinematic relations and using these values to compute the thrust using Equation 2.16. Conversely, explicit relations can be derived using Blade Element Theory which incorporates the angular rates into the thrust equation as was done by Bristeau et al. [10]. However, the relations they derive incorporate simplifications such as assuming that the vehicle angular rates stay below 1 rad/s in magnitude and that the translational velocities have magnitudes of less than 10 m/s. Even with these limitations, the flight envelopes for which the equations are valid is still reasonably large.

Blade Flapping

When a spinning, thrust generating and elastic propeller moves through the air in a way that there is a significant component of airspeed perpendicular to the axis of the rotor, a phenomenon termed as blade flapping occurs. Blade flapping is described as the vertical oscillatory motion (along the rotational axis) of each propeller blade from the horizontal plane (in the body frame) as it rotates about the propeller rotational axis. This phenomenon has been studied extensively in helicopters [40, 27] and has also been analysed for quadrotors by several authors [22, 10, 38].

Blade flapping is triggered because of the radially asymmetric velocity distribution about the rotational axis of the rotor in transitional flight. The advancing blade experiences a higher velocity, and thus higher lift and drag forces than the retreating blade. This asymmetry is maximum when a blade is oriented perpendicular to the flight direction (advancing or retreating). The imbalance in lift forces causes the blades to rise (on the advancing side) and fall (on the retreating side). However, because of the high angular velocity of the blades, the maximum angular deflections of the blades about the flapping axis occur approximately 90 degrees out of phase of the maximum force application. Thus, the maximum flapping angle occurs in the direction of flight, and the minimum in the opposite direction.

In helicopters, flapping is a very important phenomenon which enables high-speed flight. This is because the flapping motion locally decreases the angle of attack on the advancing blade and increases it on the retreating blade which helps to balance the undesirable effects of the asymmetric velocity distribution around the rotational axis [40, 27].

Helicopter rotors incorporate a flapping hinge, and the analysis of the flapping angle of the blades is carried out by enforcing a moment equilibrium of gravitational, centrifugal, and aerodynamic moments about this hinge for infinitesimally small blade elements and integrating them along the blade. A solution for the flapping angle as a function of the blade azimuth (Ψ) is obtained by assuming that only the first harmonic of blade flapping is considered. The solution is defined as a Fourier series shown in Equation 2.17 where a_0 is the coning angle of the rotor, a_{1_s} is the tilt of the rotor plane around the axis orthogonal to the velocity vector of the rotor, and b_{1_s} is the tilt of the rotor plane around the velocity vector [27, 3]. The azimuth angle Ψ is taken as zero at the rear of the rotor which is the direction opposite the in-plane velocity vector of the rotor, and is measured positive counter-clockwise when viewing the rotor from above.

$$\beta = a_0 - a_{1s}\cos\Psi + b_{1s}\sin\Psi \tag{2.17}$$

By obtaining the flapping coefficients, the tilt of the rotor can be defined and thus the forces generated as a result of the flapping can be calculated. Bangura et al. [3] have derived a lumped parameter model for blade flapping which simplifies flapping coefficient relations derived by Pounds [37]. The flapping coefficients that they derive account for the effects of the angular velocity of the body and are calculated using Equation 2.18 and Equation 2.19 where $V_p = (u\ v\ 0)^T$ is the xy plane body velocity vector. It must be noted here that the signs of the terms in the equations have been adjusted here to be consistent with Equation 2.17.

Defining the lumped parameter matrices A_{flap} and B_{flap} as shown in Equation 2.20 and Equation 2.21 respectively, the drag like effects due to the flapping of the i_{th} rotor can be calculated using Equation 2.22 [3].

The coefficients of the two matrices are dependent on the geometry of the propeller and can be estimated by matching the model to flight recorded test data. This model makes a simplification by assuming that the square of the advance ratio $\mu = \frac{|V_p|}{\Omega R}$ is negligible. Additionally, these equations do not consider the stiffness of the rotor blades, instead assuming they are hinged as is done in helicopter blade flapping analysis.

$$a_{1s} = \frac{|V_p|}{\Omega R} A_{1c} + \frac{1}{\Omega} B_2 p - \frac{1}{\Omega} B_1 q \tag{2.18}$$

$$b_{1s} = -\frac{|V_p|}{\Omega R} A_{1s} + \frac{1}{\Omega} B_1 p - \frac{1}{\Omega} B_2 q \tag{2.19}$$

$$A_{flap} = \frac{1}{R} \begin{pmatrix} -A_{1c} & A_{1s} & 0\\ -A_{1s} & -A_{1c} & 0\\ 0 & 0 & 0 \end{pmatrix}$$
 (2.20)

$$B_{\text{flap}} = \begin{pmatrix} B_2 & -B_1 & 0 \\ B_1 & -B_2 & 0 \\ 0 & 0 & 0 \end{pmatrix}$$
 (2.21)

$$D_{flap_i} = T_i \left(A_{flap} \frac{\boldsymbol{V}_{p_i}}{\Omega_i} + B_{flap} \frac{\boldsymbol{\omega_B}}{\Omega_i} \right)$$
 (2.22)

The coefficients a_{1s} and b_{1s} have been modelled by Hoffmann et al. [22] for quadrotor propellers. They analyse the flapping by treating the propeller as having a virtual torsional hinge with a spring constant k_{β} at a location e_f scaled by the radius R of the rotor. Thus, e_f is the effective hinge offset. The flapping coefficients are obtained by solving the system described by Equation 2.23. μ_{lon} and μ_{ver} are the horizontal and vertical advance ratios respectively, Θ_{avg} is the average pitch angle of the propeller blade, λ_{β} is the ratio of the flapping frequency ω_{β} to the rotor speed Ω and is calculated using Equation 2.24. I_b is the effective moment of inertia of the blade about the flapping axis and γ is the lock number which is a dimensionless parameter which quantifies the ratio of aerodynamic forces to the centrifugal forces on the blade [27].

$$\begin{bmatrix} \lambda_{\beta}^{2} & 0 & 0 & 0 \\ \frac{\gamma}{6}\mu_{lon} & \left(1-\lambda_{\beta}^{2}\right) & -\frac{\gamma}{8} & 0 \\ 0 & \frac{\gamma}{8} & \left(1-\lambda_{\beta}^{2}\right) & 0 \\ 0 & 0 & 0 & 1 \end{bmatrix} \begin{bmatrix} a_{0} \\ a_{1s} \\ b_{1s} \\ \frac{C_{T}}{\sigma a_{0}} \end{bmatrix} = \begin{bmatrix} \frac{\gamma}{8} & -\frac{\gamma}{6} \\ 0 & 0 \\ \frac{\gamma}{3}\mu_{lon} & 0 \\ \frac{1}{3} & -\frac{1}{2} \end{bmatrix} \begin{bmatrix} \Theta_{avg} \\ \mu_{ver} + \lambda_{i} \end{bmatrix}$$
 (2.23)

$$\lambda_{\beta} = \sqrt{1 + \frac{3}{2}e_f + \frac{k_{\beta}}{I_b\Omega^2}} \tag{2.24}$$

The tilt of the rotor plane causes the thrust vector to no longer be aligned with the axis of the electric motor. Thus the component of the thrust vector projected onto the shaft plane of the motor create additional drag forces which are quantified by Equation 2.22. When a quadrotor flies straight at high speed, and if the rotors lie above the center of gravity of the quadrotor at some distance l, the drag forces arising due to blade flapping create a pitch up moment given by Equation 2.25 which must be compensated for by the rear rotors. The lateral tilt of each rotor also produces side forces $T_{b,lat} = T \sin b_{1s}$, but for a quadrotor with undamaged propellers, these side forces cancel out for the forward and aft propeller pairs because of their opposite spin directions [22]. However, in the case where a propeller blade is asymmetrically damaged, a force imbalance will result creating a yawing moment on the quadrotor body.

$$M_{b,lon} = Tl\sin a_{1s} \tag{2.25}$$

The stiffness of the blade also causes an additional moment on the rotor hub which is proportional to the flapping coefficients. The longitudinal flapping moment created by the spring stiffness of the blade is calculated using Equation 2.26 [22]. It must be noted that in all discussions of blade flapping in quadrotors and helicopters as well, the dynamics of the change in flapping angles are usually not considered. Instead, only the steady-state solutions are used. This is because it has been experimentally verified that because of strong aerodynamic damping, the tilt of the rotor plane caused by flapping reaches a steady-state value very quickly, within the time frame of a single rotation [27, 40].

$$M_{bs} = k_{\beta} a_{1s} \tag{2.26}$$

The overall conclusion from past literature on blade flapping is that it has a significant effect on the dynamics of a quadrotor in high-speed flight. All previous research on this phenomenon is done on undamaged propellers which allow for some simplifications to be made such as ignoring the lateral forces and moments generated due to blade flapping. For a quadrotor inflicted with asymmetric blade damage, these simplifications cannot be made. Thus, it is worth exploring these effects to build accurate dynamic models for a quadrotor with asymmetric blade damage. In the next chapter, previous work done specifically on quadrotors with damaged blades is presented

Quadrotor Blade Damage

Quadrotors and UAVs in general are susceptible to faults which affect their ability to fly safely. Several sources of faults exist such as sensor errors, structural damage, or faults in the propulsion system motors. Sensor faults have been studied by various authors and sensor fault detection and isolation systems have been designed. Controllers have also been developed to enable the flight of a quadrotor with a complete loss of effectiveness of one or two diagonally opposing motors [49].

Physical damage to the rotor blades is one of the important faults that must be considered for quadrotors. This because in several popular quadrotor designs, the rotors are the most exposed part of the drone and thus likely the first point of contact during collisions. Additionally, high rotational energy makes rotors susceptible to damage in the event of a collision. Fault diagnosis of damaged quadrotor propellers has been researched extensively in the literature, along with methodologies for control in the presence of propeller damage. It was found that most of the methodologies for the detection of damage are model free. The control strategies developed for handling blade damage are also often model-free or rely on very simple models to compensate for the effects of damaged blades. The work done towards blade damage detection is discussed in Section 3.1 and fault-tolerant control techniques are discussed in Section 3.2.

3.1. Blade Damage Detection

Several model-based and model-free approaches for blade damage detection have been proposed in the literature. First model-based approaches are discussed followed by model free.

Ghalamchi et al. [18] propose a method which relies on accelerometer measurements to estimate mass imbalances in propellers. The method works by using an extended Kalman filter where the states to be estimated encode the propeller mass imbalance information. The method relies on a model for the thrust produced by each propeller. The authors use a simple thrust model explained in Chapter 2, computed using Equation 2.10. The dynamics of the unbalances are assumed to be driven by zero-mean, white, and independent noise. The authors have applied their method to three quadrotors at differing size scales, and show good experimental results in identifying the extent of propeller damage. However, the damage cases considered were quite minor at 4% to 10% mass imbalance. Additionally, because the thrust model is assumed to be very simple, it is unclear how well this method would work in high-speed flight.

Brown et al. [11] have conducted a series of experiments with propellers subjected to various levels of symmetric and asymmetric blade damage. The experiments were conducted both on a test bench with a single motor and on a quadrotor platform. The goal of their work was to determine the effectiveness of various sensors as classifiers for detecting rotor damage. The sensors which were studied included load cells, current sensors, thermocouples, and accelerometers to measure vibrations.

Although the authors made use of the loss of lift as a means of detecting propeller damage, they do not attempt to fit a model for how the lift force is affected by different levels of damage. The main conclusion from the study is that vibrations measured by an accelerometer are most informative for characterizing blade damage. However, they also conclude that temperature, current/power, and lift measurements also offer useful metrics.

Guzman-Rabasa [21] et al. propose an approach for detecting partial or total faults in propulsion units. Partial

faults include loss of motor effectiveness or damage to the propellers. In simple terms, the approach works by checking the residuals of the roll angle and pitch angle as the difference between the estimates of the angles obtained from an H_{∞} observer and the measurements of the angles obtained from the IMU. When the residuals in either pitch or roll cross a certain threshold, a fault is detected. In order to estimate the roll and pitch angles, the authors have modelled the rotational dynamics as a quasi-linear-parameter-varying (qLPV) system based on which the observer is designed. The fault detection approach has only been tested in simulation for partial and complete loss of rotor effectiveness.

Lee et al. [26] have developed a model-based approach for fault classification and diagnoses of UAV faults. The method works by identifying faults based on deviations from a healthy steady-state current-speed-voltage curve of a brushless DC motor. Various fault scenarios are considered such as bearing faults, stator faults, rotor faults and ESC faults. The rotor fault case was a propeller damaged by reducing the length (or span) by 30% symmetrically. The effects of the damage were observed in the speed-voltage and current-voltage plots. The speed for the damaged rotor was higher for a given input voltage because of the lower drag, and the current-voltage curve shifts downwards because of the reduced power draw. The rotor damage case was only tested on a test rig and not on a flying quadrotor.

In addition to the aforementioned model-based propeller damage detection methodologies, several model-free and data-driven approaches have also been researched. Du et al. [14] have used a 1D convolutional neural network to detect blade damage from accelerometer signals, which is a model-free approach. Thus, no dynamic modelling is done of the quadrotor in the damaged state.

Fu et al. [17] propose a data-driven propeller damage detection method which uses a hybrid neural network architecture which combines one-dimensional convolutional neural networks and long short-term memory recurrent neural networks. The inputs include attitude, attitude rates, and commanded motor speeds.

Jiang et al. [25] propose a data-driven approach where wavelet packet decomposition of the accelerometer measurements is used to extract features from flight data collected from a quadrotor with damaged propellers. The extracted features are used to train an artificial neural network which is then experimentally shown to classify blade damage. A similar approach was proposed by Bondyra et al. [9, 8] which investigates additional sources of features such as using Fast Fourier Transforms of IMU signals, and the signal power in different frequency bands, in addition to the wavelet packet decomposition approach. Additionally, they use a support vector machine to classify the damage cases based on feature vectors instead of a neural network. They conclude that the Fast Fourier Transform provides the best compromise between fault detection and damage scale estimation with lower accuracy in fault type classification.

Liu et al. [29] propose a data-driven approach for detecting and classifying asymmetric rotor blade damage which relies on audio signals rather than IMU data. The key advantage of using audio signals is the much higher sampling frequency compared to most onboard IMUs. The authors use a technique called transfer learning to improve the generalization capability of the trained convolutional neural network based model from platform to platform.

The general conclusion from analysing previous work in rotor blade damage detection is that several techniques are model-free, while the model-based techniques rely on very simple models for forces generated by the damaged rotors.

3.2. Fault tolerant control in the presence of blade damage

A literature review of research into fault-tolerant control techniques to deal with actuator faults with a focus on rotor blade damage was conducted. These findings are summarised in this section.

Li et al. [28] have applied sliding mode control (SMC) on a quadrotor drone inflicted with damage to the rotor blades. The type of damage that they consider is symmetric and applied to one of the four two-bladed rotors. The authors have tested both a passive and active sliding mode control scheme and compared the performance of both approaches through real experimental test flights.

The passive SMC approach relies on a dynamic model of the undamaged quadrotor. Actuator faults are dealt with through SMC scheme which accounts for the faults through maximum bounds on the severity of the faults. The active SMC scheme actually incorporates the damage to propellers into the dynamic model. This is done by scaling the actuator input based on by some factor k which lies in the range [0,1]. The authors do not develop a

scheme for estimating the degradation, but instead implement a controller which can improve performance with the assumption that the level of loss of effectiveness is estimated through another fault diagnosis scheme. It is clear however that the model used to account for the damage to the propeller is rather simple, but good enough for the symmetric propeller damage scenario.

Chamseddine et al. [12] have applied a Model Reference Adaptive Control (MRAC) technique to a quadrotor drone with symmetric blade damage. In fact, the quadrotor platform they used was the same one used by Li et al. [28]. The goal of model reference adaptive control is to alter the behaviour of the system to be controlled such that it matches a reference system with specified parameters. The challenge is to estimate the parameters of the control law, without knowledge of the actual system such that the desired behaviour is achieved. The control parameters can be updated using a number of techniques, of which the authors have implemented the MIT rule [23], conventional MRAC [43] and modified MRAC [44].

The MRAC scheme was tested by the authors in three fault scenarios, the most important being one where symmetric physical damage is injected into the propellers mid-flight. It is clear that the MRAC scheme manages to perform well compared to a linear quadratic regulator which was taken as a benchmark. However, again, the control scheme does not take advantage of a known accurate system model in the presence of blade damage but rather updates the control parameters to account for the changed system behaviour.

Guo et al. [20] have developed a control scheme for quadrotors simultaneously subjected to blade damage and ground effect. The authors have used blade element theory to derive a simple relationship between the ratio of thrust generated by a damaged propeller to that of an undamaged propeller for symmetric damage. The thrust generated by the damaged propeller is derived by integrating the lift force of blade elements up to the point at which the blade is broken, rather than integrating over the full radius of the propeller. Through this analysis, the authors conclude that the ratio of thrust force depends on the cube of the ratio of damaged rotor radius to that of the original radius. Through similar analysis, the ratio of undamaged to damaged torque generated is equal to the square of the ratio of the damaged radius to that of the undamaged radius. For example, a 25% reduction in the radius of the rotor results in a 58% lift reduction and a 69% torque reduction. These relations are not used to explicitly design the controller, or experimentally verified, but instead serve as an estimation to show the level of performance loss that the controller is able to compensate for.

This chapter provided an overview of past work done towards detecting propeller blade damage in quadrotors and controlling quadrotors subjected to propeller blade damage. The main gap in knowledge found is that there are no high fidelity models which describe the dynamics of a quadrotor which is afflicted with symmetrically or asymmetrically damaged rotors. The development of such models can enable the design of better control strategies, especially in high-speed flight. In addition, high fidelity models for quadrotors with damaged propellers will also enhance the safety of these aircraft by enabling flight envelope estimation in damaged states, which is discussed in more detail in the next chapter.

4

Safe Flight Envelopes

Dynamic systems are governed by a set of differential equations which describe the evolution of the system states based on the current state, inputs to the system, and disturbances. The quadrotor is an example of such a dynamical system, the modelling for which was discussed in Chapter 2. Dynamic models encode information about the extent of the state space a system can explore given some admissible control inputs and subjected to external disturbances. Explicitly determining the extent of the reachable space is useful because it offers important information regarding what states the system can achieve.

Aircraft such as fixed-wing aeroplanes, helicopters, and quadrotors are all types of dynamical systems which share similarities. The reachable regions in the state spaces of these types of systems are referred to as flight envelopes or dynamics envelopes. Another type of flight envelope also referred to as a Safe Flight Envelope (SFE) is the set of states that can be reached by the aircraft from a given trim condition, and from which the aircraft can return back the trim set within a prescribed time horizon without loss of control [52].

In this chapter, some of the approaches for estimating safe flight envelopes are briefly discussed in Section 4.1 followed by a discussion on database drive flight envelope protection in Section 4.2. The chapter is concluded with a motivation for modelling quadrotor damage cases in order to enable envelope estimation.

4.1. Safe Flight Envelope Estimation Techniques

Several approaches for estimating safe flight envelopes have been developed. Two methods for estimating flight envelopes are discussed here. The first method is the most commonly found in literature and is based on reachability analysis using level set methods. The second method uses Monte Carlo simulations to general safe flight envelopes. Before presenting these methods, a more formal description and definition of a 'Safe Flight Envelope' is presented.

Consider an aircraft, be it a fixed-wing passenger airliner or a quadrotor drone. The dynamics of these systems are represented by a set of first-order ordinary differential equations of the form $\dot{x} = f(x, u)$ where $x \in \mathbb{R}^n$ is the state vector and $u \in \mathbb{R}^m$ is the input vector. Then, the safe flight envelope is defined as the intersection of the forward reachable set, and the backward reachable set. Where the forward reachable set is the set of states $x \in \mathbb{R}^n$ that can be reached from an initial trim set K given admissible control inputs within a specified time horizon, and the backward reachable set is the set of states from which the system can recover to the trim set K given admissible control inputs within a specified time horizon.

One of the more popular methods uses reachability analyses to compute safe flight envelopes via the level set method [33, 16]. The reachable set is obtained as the level set of a function V(x,t) which is found by numerically solving partial differential equations known as the Hamilton-Jacobi-Isaacs (HJI) or Hamilton-Jacobi-Bellmann (HJB) equations. The former is used when disturbances are not modelled in the dynamics system, while the latter equation includes disturbances which in the case of aircraft might be wind gusts or uncertainty in the parameters of the dynamic model.

Recently, a new method for estimating safe flight envelopes through Monte-Carlo simulations has been applied to quadrotors by Sun and de Visser [46]. This approach tries to overcome the 'curse of dimensionality' [36] of the level set method and thus offers a more computationally efficient means of computing safe flight envelopes.

Both the level set method and the monte-carlo method require accurate models of the system in order to accurately estimate the safe flight envelope.

4.2. Database Driven Flight Envelopes

Global dynamics models of an aircraft are required to compute reachable sets. However, in the presence of physical damage, the dynamic model of the system is altered. Estimating flight envelopes online in the event of physical damage presents two major challenges. For one, online identification of a global system model online in the presence of damage is challenging because only small deviations from the local state can be achieved. The second challenge is the computational resources required to compute flight envelopes, which are more limited for micro aerial vehicles than bigger aircraft [56].

Thus, a novel approach to flight envelope estimation using databases was developed by Zhang et al. [56, 57, 59] and applied to a fixed-wing business jet aircraft in simulation. At a high level, the database-driven flight envelope estimation and protection system uses pre-computed databases of safe flight envelopes which are stored onboard the aircraft. When physical damage is sustained, online identified aerodynamic model parameter changes are used to determine the location and extent of the damage through a neural-network based damage classification scheme [56]. Flight envelopes corresponding to the predicted damage case are then retrieved from the database.

The pre-computed damage cases correspond to different levels of damage for various aerodynamic surfaces. For example, damage to the left wing of the aircraft generates different levels of constant rolling moments depending on the level of damage which can be quantified by the rolling moment bias term (C_{l_0}) and a loss of rolling control effectiveness $(C_{l_{\delta_0}})$ in the aerodynamic rolling moment model.

While the database-driven approach has been applied to fixed-wing aircraft in simulation, quadrotor UAVs offer a cheaper platform for real world experiments. Unlike fixed-wing aircraft, quadrotors rely on rotors for generating lift and controllability. Thus, structural damage to rotor blades has a significant negative impact on the flight worthiness of a quadrotor. Quantifying the effects of blade damage by identifying models of a quadrotor through experimental test fights will enable safe flight envelope estimation for quadrotors inflicted with blade damage.

Quadrotor System Identification

System identification essentially is the process of representing a system in a mathematical form which can be used to predict the real observed behaviour of the system reliably and with good accuracy. Aircraft system identification has become a fairly mature field, with several published textbooks that provide a detailed description of the whole process [24, 34].

Quadrotors modelling research has been gaining popularity recently as is apparent through an examination of recent work done in the field [49, 45, 47, 48, 4, 2]. While a large portion of the past literature focuses on obtaining models for undamaged quadrotors, Sun et al. [48] have obtained a model for a quadrotor subject to a total failure in one of the rotors. However, as was concluded in Chapter 3, the effects of physical damage to the rotor blades on the dynamic model of a quadrotor have not been investigated in detail. In Chapter 4, an argument was laid out for the importance of obtaining such models to enable safe flight envelope estimation. In this chapter, approaches for identifying quadrotor models are presented, along with some preliminary insights as to how blade damage is expected to affect the dynamics of a quadrotor.

In past literature, quadrotor model identification has been performed using linear regression applied polynomial model structures [45, 47] as well as deep learning [4]. The polynomial model-based approaches offer the advantage of physically motivated model structures which are more intuitive to reason and understand but may fail to capture important dynamics because of model structures which are restricted to be linear in the model parameters. Artificial neural networks in contrast are black-boxes which offer little insight into the internal works of the model, with the advantage being that they are able to "learn" patterns in data that may not be captured by linear-in-parameters polynomial models. Polynomial modelling is discussed in Section 5.1, followed by a short discussion of neural networks and other advanced modelling techniques and how they can be applied to quadrotor modelling in Section 5.2.

5.1. Polynomial Models

Polynomial models relate a dependent variable to sets of polynomials of independent variables. Given a dataset of the values of the independent variables, and corresponding values of the dependent variable, a regression model given by Equation 5.1 can be formulated. Where $\boldsymbol{y} \in \mathbb{R}^n$ is the vector of observations of the dependent variable, $\boldsymbol{\theta} \in \mathbb{R}^p$ is a vector of parameters which relate the regressors of the independent variables $A = [1 \ \boldsymbol{\xi_1} \ \boldsymbol{\xi_2} \dots \boldsymbol{\xi_p}] \in \mathbb{R}^{N \times p}$ to the dependent variable, and $\epsilon \in \mathbb{R}^n$ is the unmodelled error. The optimal set of parameters $\hat{\boldsymbol{\theta}}$ which minimises the mean squared error of the model residuals $\boldsymbol{\epsilon^2}$ is computed using Equation 5.2, which is the Ordinary Least Squares (OLS) estimator.

$$y = A\theta + \epsilon \tag{5.1}$$

$$\hat{\boldsymbol{\theta}} = \left(A^T A\right)^{-1} A^T \boldsymbol{y} \tag{5.2}$$

For quadrotors and aircraft in general, the model outputs are generally the estimated forces and moments acting on the aircraft body. The regressor matrix A is comprised of state variables such as the angle of attack, angular rates, and body velocities.

Step-wise linear regression

The simple linear regression model described above can be modified by including the determination of the model structure as part of the modelling error minimisation problem. This is done using an algorithm which selects the regressors in the A matrix from a pool of candidate regressors in a step-by-step approach such that the prediction accuracy of the model is improved. Sun et al. [45] have applied this approach for identifying a gray-box aerodynamic quadrotor model. The steps of the algorithm are presented here.

Before applying the step-wise regression algorithm, a set of regressors must be defined. These regressors can be any continuous function of the regressors such as the exponential functions, and log functions. However, a popular choice is to use polynomials [45]. Given a dependent variable y in a set of independent variables x_1, x_2, x_3 , an example of a preliminary model structure is given by Equation 5.3 where $P_1^2(x_1, x_3)$ represents the second-order polynomial functions in x_1 and x_3 . Similarly, the term $P_2(x_1, x_2)x_3$ includes second-order polynomials in x_1 and x_2 which are all multiplied by x_3 .

$$y = P_1^2(x_1, x_3) + P_2(x_1, x_2)x_3$$
(5.3)

With a set of regressors selected, the step-wise regression procedure is as follows [45]:

- The model is initialized with only the constant terms $A = \begin{bmatrix} 1 & 1 & \dots & 1 \end{bmatrix}^T$.
- The algorithmic loop is entered:
 - 1. The model parameters $\hat{\theta}$ are estimated using Equation 5.2, and the model residuals ϵ are computed.
 - 2. The pool of candidate regressors is made orthogonal to the terms in the model. For each regressor ξ_i , the orthogonal regressor λ_i is obtained as

$$\lambda_{i} = \boldsymbol{\xi}_{i} - A \left(A^{T} A \right)^{-1} A^{T} \boldsymbol{y} \tag{5.4}$$

- 3. After all candidate regressors are made orthogonal, the regressor λ_j with the highest correlation to the model residual is found. Then, the corresponding regressor ξ_i is added to the regressor matrix.
- 4. The existing regressors are statistically evaluated using an F test. Given q regressors in the current model, the partial F-ratio for the k_{th} regressor is calculated using Equation 5.5 where s^2 is the variance of the fit error computed using Equation 5.6 for N data points.

$$F_0 = \frac{SS_R(\hat{\boldsymbol{\theta}}_q) - SS_R(\hat{\boldsymbol{\theta}}_{q-k})}{s^2}$$
 (5.5)

$$s^2 = \frac{\epsilon^T \epsilon}{N - q - 1} \tag{5.6}$$

 $SS_R(\hat{\theta}_q)$ is the regression sum of squares for the current model, and $SS_R(\hat{\theta}_{q-k})$ is the same but with regressor ξ_k removed from the model. The SS_R value is computed using Equation 5.7 where \bar{y} is the mean of the observation vector.

$$SS_R = \hat{\boldsymbol{\theta}}^T A^T \boldsymbol{y} - N\bar{\boldsymbol{y}} \tag{5.7}$$

If the regressor with the smallest F_0 value has an F score below a constant threshold F_{out} , then that regressor is removed. The algorithm stops if the regressor removed was the same as that which was added in that loop. Sun et al. [45] use an F_{out} threshold of 4.

• To avoid over-fitting, the Predict Square Error stopping criterion (Equation 5.8) is used. The first term is the mean squared fit error, and the second term penalises model redundancy, where q is the number of regressors. The PSE initially decreases with added regressors, but eventually, over-fitting can occur leading to an increase in the PSE. Thus, the algorithm is stopped when the PSE increases (or is unchanged) at the end of a loop.

$$PSE - \frac{1}{N} \epsilon^T \epsilon + \sigma_{max}^2 \frac{q}{N} \tag{5.8}$$

Quadrotor Polynomial Models

The polynomial models for quadrotors identified by Sun et al. [45] are briefly discussed here, along with some preliminary insights on how these models may be affected for a quadrotor with damaged rotor blades. The models in [45] are not non-dimensionalised, however, Sun et al. [47] later also derived more complex models which were non-dimensionalised. Further work in polynomial quadrotor model identification was also done by van Beers [7], where outdoor flight tests were used to identify models for quadrotors.

For conciseness, only the moment models from [45] are discussed here. The pitching moment (M_y) model with all candidate terms is given by Equation 5.9 where U_q determines the pitching control action based on the rotor speeds. For the rotor configuration shown in Figure 2.1 in Chapter 2, the pitching control input is calculated using Equation 5.10.

$$M_y = \frac{b}{2}kU_q + P_1^3(u, w, q)U_q + P_2^3(u, w, q)\sum \omega_i + P_3^3(u, w, q)$$
(5.9)

$$U_q = (\Omega_1^2 + \Omega_3^2) - (\Omega_2^2 + \Omega_4^2)$$
(5.10)

The above model for the pitching moment implicitly assumed that the actuators are working correctly. For example, if the front left rotor (rotor 3) is damaged, it has reduced thrust and yawing torque capacity. Thus, the pitch up control effectiveness will likely be lower than pitch down because the aft rotors are still able to produce nominal thrust. This is a local effect, which is difficult to capture with polynomial model structures because the regressors apply on the complete domain. However, it is possible that even with this shortcoming, the lumped model is still accurate, even if the parameters lose some of their physical meaning.

Continuing with the same rotor damage example, it is clear that rotor 3 will have to spin faster to compensate for the loss of thrust and yawing torque in hovering flight. Since a quadrotor is an inherently unstable system, it is assumed in the current example that a controller capable of maintaining altitude and attitude has been implemented. Due to this, the pitch control action U_q will have a constant non-zero value even in steady hovering flight. Equivalently the roll and yaw control actions, U_p and U_r respectively, will have non zero values in hovering flight. These constant offsets will be absorbed into the biases for each moment model. This is problematic because if all rotor speeds are low, resulting in the rotors producing insignificant thrust, the moment bias parameters will create non-physical moments on the body which will lead to inaccurate simulation models.

Based on the above discussion, it is evident that failures in rotors lead to local effects which can lead to global models which are not physically motivated. One possible solution for this problem would be to define global models in different flight regimes and interpolate between these models. However, that would be a tedious and in-elegant solution. In the next chapter, more advanced modelling techniques are discussed which may offer better solutions.

5.2. Advanced Modelling Techniques

In addition to polynomial models for quadrotor dynamics, a number of other techniques have been applied to aircraft system identification. These methods offer certain advantages over polynomial models obtained through linear regression. Here, Neural networks and multivariate splines are discussed as tools for quadrotor model identification.

Neural Networks

Deep feedforward networks (DNNs), also referred to as multilayer perceptrons (MLPs), are powerful function approximators, which have been applied to quadrotors for model identification by Bansal et al. [4] and more recently van Beers [7]. These models essentially determine a mapping f from inputs f to known outputs f of the form f of the form f are learned such that the underlying process being modelled is best approximated by f [19].

A DNN, depicted in Figure 5.1 by a simple network, is a collection of layers of neurons. These layers are the input layer, a series of hidden layers, and an output layer. Each hidden layer and the output layer are formed by a prescribed number of neurons, with each neuron having an associated weight, bias and activation function. In Figure 5.1, the weights between layers j and k are represented by a matrix W_{jk} , the bias vector for layer j is b_j , and the activation functions are denoted by $\phi(\cdot)$.

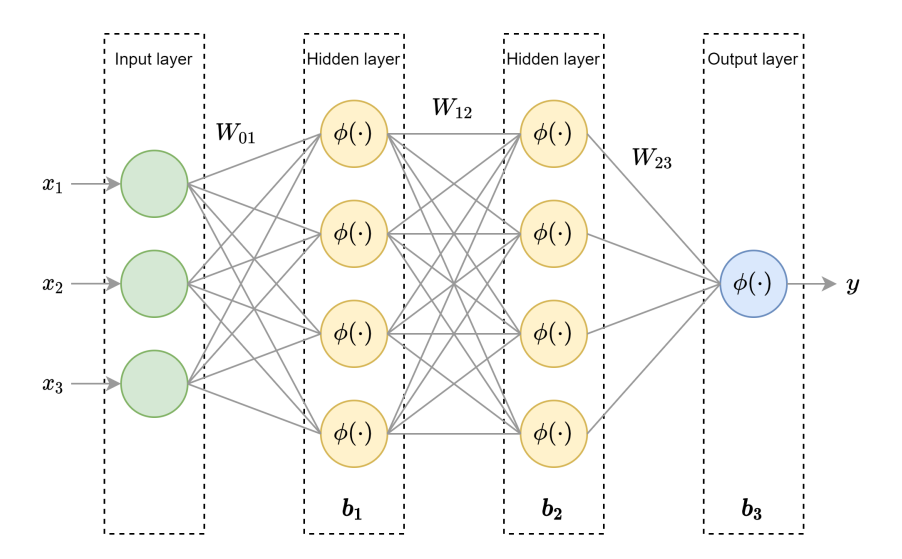


Figure 5.1: Example of a dense (fully-connected) deep neural network with two hidden layers, a 3 element input vector, and a scalar output

The activation functions play the role of adding non-linearities. There are several activation functions which have been researched. However, typically a small family of functions are used for most applications. A common choice of activation is the rectified linear unit (ReLU), $\phi(x) = max(0,x)$ [19] which was also used by Bansal et al. [4] for quadrotor model identification. Radial Bases Functions, $\phi(x) = e^{-x^2}$, have useful properties in modelling local effects. Thus, based on the shortcomings of polynomial models discussed in the previous section, RBF neural networks may offer a better alternative.

In order to train a neural network, a cost function which quantifies the difference between the model outputs and observed outputs of the process is set by the user. Typically, the squared error is chosen [19]. The cost function value is minimised by iteratively updating the weights through a training algorithm. The basic principle of the training process is to utilise information about the gradient of the cost function with respect to the weights of the network and update the weights towards the decreasing gradient in order to decrease the cost function value. Popular learning algorithms include Stochastic Gradient Descent, Momentum, AdaGrad, RMSProp and Adam. The latter three algorithms incorporate an adaptive learning rate [19]. The aforementioned algorithms are also categorised as first-order methods because they only rely on the first derivative of the cost function with respect to the network weights. Second-order techniques, as the name suggests, use information from the second derivative of the cost function with respect to the network weights. The second-order methods are more likely to find global optima and are more aggressive in applying parameter updates, with the disadvantage being that they are more computationally intensive than the first-order methods [19].

Multivariate Spline Models

Simplex B-splines are yet another tool which can be used for fitting models to scattered datasets [54, 53]. Here, model identification of a quadrotor with blade damage using multivariate simplex splines is discussed.

When using simplex splines to fit a model to data, the domain of the input dataset is divided into geometric structures called simplices that span the space in a minimal non-degenerate way [54]. Each of these simplices has a local coordinate system termed Barycentric coordinates, which allow for polynomials defined in a simplex to be expressed in the B-form. The coefficients of the polynomial expressed in the B-form are known as the B-coefficient. The B-coefficients are the "weights" which change the shape of spline functions, and can also be constrained in order to impose continuity conditions between simplices. The optimal B-coefficients can be determined using linear regression methods in order to fit the simplex spline model to a dataset [54].

The main advantages of simplex B-splines in the context of quadrotor model identification are that they have a higher approximation power, and can model local effects better than global polynomial models, as was discussed using the example of pitching moments in Section 5.1. Splines also offer a more intuitive way of understanding how the B-coefficients relate to the underlying physical phenomenon [51]. This is an advantage over the neural networks which act more like black-boxes. One limitation with multivariate splines however is that they require the domain of data to be divided into simplices, which is not always straightforward. Nonetheless, multivariate

5.3. State Estimation 63

simplex B-splines seem to be a better choice than both polynomial models and neural networks for quadrotor model identification in the presence of damaged propellers.

5.3. State Estimation

Before identifying a model from flight test data, it is essential that the model inputs - which include the states of the system - are accurately determined. Several researchers have relied on using external motion tracking systems to provide state estimates [45, 48, 5] while recently outdoor model identification has also been performed by van Beers [7]. For blade damage modelling, system identification test flights will be performed indoors, and thus external motion tracking will be employed for state estimation. The reason for indoor flights is to remove an influences of wind, but also because flying with a damaged drone outdoors in an uncontrolled environment is unsafe.

State estimation with the inclusion of external motion tracking systems can be accomplished with Kalman Filter (KF) [55], or an Extended Kalman Filter (EKF) [41]. The basic principle of the Kalman Filter is to determine the system state by taking a weighted average between the prediction of the state based on a system model, and an observation of the state through sensors such as the IMU, GPS, or in this case, external motion tracking systems. The KF is limited to linear systems, while a quadrotor is an inherently non-linear system. The EKF overcomes this limitation by treating linearising the system around the current state at each state update, and applying the KF at each step [41].



Conclusion and Research Proposal

Quadrotors have gained popularity both commercially and in academic research over the past few decades. Understanding the dynamics and modelling complex aerodynamic behaviour of quadrotors has been an important area of research [38, 22, 32, 45, 48, 47]. With the ever-increasing popularity of quadrotors, research efforts have focused on improving quadrotor safety. For example, control of quadrotors in off-nominal flight conditions such as partial loss of actuator effectiveness [15, 12, 28, 42] and complete rotor failures has been explored [35, 49, 50].

One of the key research areas concerned with improving the safety of aircraft is in safe flight envelope estimation and protection [31, 58, 46]. Safe flight envelopes provide explicit knowledge of the region of the state space of an aircraft in which it is safe to operate. Structural damage changes the flight envelope, risking an event in which the flight envelope is exited, leading to potential loss of control. Estimating flight envelopes in the presence of physical damage requires knowledge of the system dynamics in the damaged state.

Dynamic modelling of quadrotor UAVs inflicted with structural damage has not been researched extensively. While Sun et al. [48] did identify a model for a drone with a complete failure of one of the four rotors, dynamic modelling of a quadrotor with damage to the rotor blades has not been found in the literature. Instead, most of the research effort is either in the detection and diagnosis of blade damage [18, 11, 21, 26], or fault-tolerant control in the presence of blade damage [28, 12, 20]. While asymmetric blade damage detection has been explored, fault tolerant control strategies have only been tested on quadrotors with symmetric blade damage.

Apart from blade damage, structural damage to the main body which houses the electronic components, or loose actuator mounting arms are also possible scenarios. However, given that the rotors are the primary lifting and control devices on a quadrotor, and one of the most physically exposed components in popular quadrotor designs, rotor damage is a more critical failure scenario which requires investigation.

In order to model the effects of blade damage on the dynamics of a quadrotor, system identification test flights will be conducted for data gathering. Test flights will be performed with varying levels of asymmetric damage done on one, or two rotors simultaneously. The reason for not considering more than two damaged rotors is because scenarios where a collision results in three or more damaged propellers is determined to be relatively unlikely to single or dual rotor damage.

One research limitation is that with a large amount of asymmetric blade damage, the vibrations can become severe enough to the point that the inertial measurement unit saturates, or that frame resonance created by the vibrations results in the quadrotor being unable to fly. These limitations, however, answer questions regarding the limits of operability of a drone with asymmetric blade damage. An additional limitation would be that the default flight controllers on the test drones, which use PID based control laws, might not be able to control the damaged quadrotor even if other limitations do not apply. In this case, gain tuning might be required. However, preliminary flights conducted on an EMAX Tinyhawk 2 ¹ after asymmetrically damaging one of the four rotor blades on a single propeller show that a lack of thrust is the main limiting factor rather than any of the aforementioned issues.

Several techniques can be used to fit mathematical models to scattered data sets. For quadrotors, linear regression has been used to identify dynamic models from flight test data [45, 47], as well as artificial neural networks [4,

¹URL: https://droneshop.nl/emax-tinyhawk-2-ready-to-fly

7]. Multivariate simplex B-splines [54, 53] seem to provide a better alternative to both the previous techniques because of better modelling of local effects and high approximation power, which are anticipated to be prevalent in damage cases. Thus, it will be useful to investigate splines as a means of creating dynamic models for quadrotors inflicted with blade damage.

Based on the literature study presented in this report, the following research objective and research questions have been formulated:

Research Objective

"To obtain a dynamic model of a quad-rotor drone with asymmetric blade damage on one or two rotors by conducting system identification experiments through tests flights of damaged quadrotors".

Research questions

- 1. What are the effects of asymmetric blade damage on the dynamic model of a quad-rotor drone?
 - (a) What model structure is required to capture the effects of asymmetric blade damage?
 - (b) Which model terms are most effected by asymmetric blade damage?
- 2. Do multivariate simplex B-splines offer a better alternative to polynomial models for identifying the effects of asymmetric blade damage on quadrotors?
 - (a) Which method results in lower aerodynamic force and moment model residuals?
 - (b) What are the variances of the model parameters?
- 3. At what extent of asymmetric blade damage do problems caused by excessive vibrations become insurmountable?
 - (a) What auxiliary IMU (with higher measurement ranges) will have to be appended to allow for flights where the standard IMU on the drone becomes saturated?
 - (b) What resonant frequencies of the quadrotor frame inhibit flight with asymmetrically damaged rotor blades?
- 4. Which flight maneuvers should be performed for system identification of a drone with blade damage?

- [1] M Hadi Amoozgar, Abbas Chamseddine, and Youmin Zhang. "Experimental test of a two-stage Kalman filter for actuator fault detection and diagnosis of an unmanned quadrotor helicopter". In: *Journal of Intelligent & Robotic Systems* 70.1 (2013), pp. 107–117.
- [2] John E. Angarita, Kevin Schroeder, and Jonathan Black. "Quadrotor model generation using system identification techniques". In: *AIAA Modeling and Simulation Technologies Conference*, 2018. 209959. American Institute of Aeronautics and Astronautics Inc, AIAA, 2018. ISBN: 9781624105289. DOI: 10. 2514/6.2018–1917.
- [3] Moses Bangura, Robert Mahony, et al. "Nonlinear dynamic modeling for high performance control of a quadrotor". In: (2012).
- [4] Somil Bansal et al. "Learning quadrotor dynamics using neural network for flight control". In: 2016 IEEE 55th Conference on Decision and Control, CDC 2016. Institute of Electrical and Electronics Engineers Inc., Dec. 2016, pp. 4653–4660. ISBN: 9781509018376. DOI: 10.1109/CDC.2016.7798978.
- [5] Leonard Bauersfeld et al. "Neurobem: Hybrid aerodynamic quadrotor model". In: *arXiv preprint arXiv:2106.08015* (2021).
- [6] Randal W Beard and Timothy W McLain. "Small unmanned aircraft". In: *Small Unmanned Aircraft*. Princeton university press, 2012.
- [7] Jasper van Beers. "Development of a system identification routine, with prediction reliability estimates, suitable for modelling high-speed and aggressive quadrotor flight outdoors". MA thesis. the Netherlands: Delft University of Technology, 2021.
- [8] Adam Bondyra et al. "Development of the Sensory Network for the Vibration-based Fault Detection and Isolation in the Multirotor UAV Propulsion System". In: *ICINCO 2018 Proceedings of the 15th International Conference on Informatics in Control, Automation and Robotics*. Vol. 2. SciTePress, 2018, pp. 102–109. ISBN: 9789897583216. DOI: 10.5220/0006846801020109.
- [9] Adam Bondyra et al. Fault Diagnosis and Condition Monitoring of UAV Rotor using Signal Processing. Tech. rep.
- [10] Pierre-Jean Bristeau et al. "The role of propeller aerodynamics in the model of a quadrotor UAV". In: 2009 European control conference (ECC). IEEE. 2009, pp. 683–688.
- [11] Joseph M Brown et al. "Characterization and prognosis of multirotor failures". In: *Structural Health Monitoring and Damage Detection, Volume 7.* Springer, 2015, pp. 157–173.
- [12] Abbas Chamseddine et al. "Model reference adaptive fault tolerant control of a quadrotor UAV". In: *AIAA Infotech at Aerospace Conference and Exhibit 2011*. American Institute of Aeronautics and Astronautics Inc., 2011. ISBN: 9781600869440. DOI: 10.2514/6.2011–1606.
- [13] Anthony R Cummings et al. "The rise of UAVs". In: *Photogrammetric Engineering & Remote Sensing* 83.4 (2017), pp. 317–325.
- [14] Canyi Du et al. "Unmanned aerial vehicle rotor fault diagnosis based on interval sampling reconstruction of vibration signals and a one-dimensional convolutional neural network deep learning method". In: *Measurement Science and Technology* 33.6 (June 2022). ISSN: 13616501. DOI: 10.1088/1361-6501/ac491e.
- [15] Zachary T. Dydek, Anuradha M. Annaswamy, and Eugene Lavretsky. "Adaptive control of quadrotor UAVS in the presence of actuator uncertainties". In: *AIAA Infotech at Aerospace 2010*. 2010. ISBN: 9781600867439. DOI: 10.2514/6.2010-3416.
- [16] Stanley Osher Ronald Fedkiw and Stanley Osher. "Level set methods and dynamic implicit surfaces". In: *Surfaces* 44.77 (2002), p. 685.
- [17] Jiangmeng Fu et al. "A hybrid CNN-LSTM model based actuator fault diagnosis for six-rotor UAVs". In: 2019 Chinese Control And Decision Conference (CCDC). IEEE. 2019, pp. 410–414.

[18] Behnam Ghalamchi, Zheng Jia, and Mark Wilfried Mueller. "Real-Time Vibration-Based Propeller Fault Diagnosis for Multicopters". In: *IEEE/ASME Transactions on Mechatronics* 25.1 (Feb. 2020), pp. 395–405. ISSN: 1941014X. DOI: 10.1109/TMECH.2019.2947250.

- [19] Ian Goodfellow, Yoshua Bengio, and Aaron Courville. *Deep Learning*. http://www.deeplearningbook.org. MIT Press, 2016.
- [20] Kexin Guo et al. "Safety Control for Quadrotor UAV against Ground Effect and Blade Damage". In: *IEEE Transactions on Industrial Electronics* (2022). ISSN: 15579948. DOI: 10.1109/TIE.2022.3140494.
- [21] Julio Alberto Guzmán-Rabasa et al. "Actuator fault detection and isolation on a quadrotor unmanned aerial vehicle modeled as a linear parameter-varying system". In: *Measurement and Control (United Kingdom)* 52.9-10 (Nov. 2019), pp. 1228–1239. ISSN: 00202940. DOI: 10.1177/0020294018824764.
- [22] Gabriel M. Hoffmann et al. "Quadrotor helicopter flight dynamics and control: Theory and experiment". In: *Collection of Technical Papers AIAA Guidance, Navigation, and Control Conference 2007*. Vol. 2. 2007, pp. 1670–1689. ISBN: 1563479044. DOI: 10.2514/6.2007–6461.
- [23] Petros A Ioannou and Jing Sun. *Robust adaptive control*. Vol. 1. PTR Prentice-Hall Upper Saddle River, NJ, 1996.
- [24] Ravindra V Jategaonkar. *Flight vehicle system identification: a time domain methodology*. American Institute of Aeronautics and Astronautics, 2006.
- [25] YAN Jiang et al. "Fault detection and identification for quadrotor based on airframe vibration signals: a data-driven method". In: 2015 34th chinese control conference (ccc). IEEE. 2015, pp. 6356–6361.
- Jun yong Lee et al. "Fault Classification and Diagnosis of UAV motor Based on Estimated Nonlinear Parameter of Steady-State Model". In: *International Journal of Mechanical Engineering and Robotics Research* 10.1 (Jan. 2021), pp. 22–31. ISSN: 22780149. DOI: 10.18178/IJMERR.10.1.22–31.
- [27] Gordon J Leishman. *Principles of helicopter aerodynamics with CD extra*. Cambridge university press, 2006.
- [28] Tong Li, Youmin Zhang, and Brandon W. Gordon. "Passive and active nonlinear fault-tolerant control of a quadrotor unmanned aerial vehicle based on the sliding mode control technique". In: *Proceedings of the Institution of Mechanical Engineers. Part I: Journal of Systems and Control Engineering* 227.1 (Jan. 2013), pp. 12–23. ISSN: 09596518. DOI: 10.1177/0959651812455293.
- [29] Wansong Liu, Zhu Chen, and Minghui Zheng. "An audio-based fault diagnosis method for quadrotors using convolutional neural network and transfer learning". In: 2020 American Control Conference (ACC). IEEE. 2020, pp. 1367–1372.
- [30] Thomas Lombaerts et al. On-Line Safe Flight Envelope Determination for Impaired Aircraft. Tech. rep.
- [31] Thomas J.J. Lombaerts et al. "Safe maneuvering envelope estimation based on a physical approach". In: *AIAA Guidance, Navigation, and Control (GNC) Conference*. American Institute of Aeronautics and Astronautics Inc., 2013. ISBN: 9781624102240. DOI: 10.2514/6.2013-4618.
- [32] Robert Mahony, Vijay Kumar, and Peter Corke. "Multirotor aerial vehicles: Modeling, estimation, and control of quadrotor". In: *IEEE Robotics and Automation Magazine* 19.3 (2012), pp. 20–32. ISSN: 10709932. DOI: 10.1109/MRA.2012.2206474.
- [33] Ian Mitchell and Claire J Tomlin. "Level set methods for computation in hybrid systems". In: *International workshop on hybrid systems: Computation and control*. Springer. 2000, pp. 310–323.
- [34] Eugene A Morelli and Vladislav Klein. *Aircraft system identification: theory and practice*. Vol. 2. Sunflyte Enterprises Williamsburg, VA, 2016.
- [35] Mark W Mueller and Raffaello D'Andrea. "Stability and control of a quadrocopter despite the complete loss of one, two, or three propellers". In: 2014 IEEE international conference on robotics and automation (ICRA). IEEE. 2014, pp. 45–52.
- [36] H. N. Nabi et al. "Effects of structural failure on the safe flight envelope of aircraft". In: *Journal of Guidance, Control, and Dynamics* 41.6 (2018), pp. 1257–1275. ISSN: 15333884. DOI: 10.2514/1.G003184.
- [37] Paul Pounds. "Construction and Control of a Large Quadrotor Micro Air Vehicle". In: *ANU PhD Thesis* (2007).

[38] Paul Pounds, Robert Mahony, and Peter Corke. "Modelling and control of a quad-rotor robot". In: *Proceedings of the 2006 Australasian Conference on Robotics and Automation*. Australian Robotics and Automation Association (ARAA). 2006, pp. 1–10.

- [39] Caitlin Powers et al. "Influence of aerodynamics and proximity effects in quadrotor flight". In: *Experimental robotics*. Springer. 2013, pp. 289–302.
- [40] Raymond W. Prouty. Helicopter performance, stability, and Control. Krieger Publishing Company, 2002.
- [41] Maria Isabel Ribeiro. "Kalman and extended kalman filters: Concept, derivation and properties". In: *Institute for Systems and Robotics* 43 (2004), p. 46.
- [42] Iman Sadeghzadeh, Ankit Mehta, and Youmin Zhang. "Fault/damage tolerant control of a quadrotor helicopter UAV using model reference adaptive control and gain-scheduled PID". In: AIAA Guidance, Navigation, and Control Conference 2011. American Institute of Aeronautics and Astronautics Inc., 2011. ISBN: 9781600869525. DOI: 10.2514/6.2011-6716.
- [43] Vahram Stepanyan and Krishnakumar Kalmanje. "Input and output performance of M-MRAC in the presence of bounded disturbances". In: *AIAA Guidance, Navigation, and Control Conference*. 2010, p. 7688.
- [44] Vahram Stepanyan and Kalmanje Krishnakumar. "MRAC revisited: guaranteed performance with reference model modification". In: *Proceedings of the 2010 American Control Conference*. IEEE. 2010, pp. 93–98.
- [45] S. Sun, R. J. Schilder, and C. C. De Visser. "Identification of quadrotor aerodynamic model from high speed flight data". In: AIAA Atmospheric Flight Mechanics Conference, 2018. Vol. 0. 209999. American Institute of Aeronautics and Astronautics Inc, AIAA, 2018. ISBN: 9781624105258. DOI: 10.2514/6.2018-0523.
- [46] S. Sun and C. C. de Visser. "Quadrotor safe flight envelope prediction in the high-speed regime: A monte-carlo approach". In: *AIAA Scitech 2019 Forum*. American Institute of Aeronautics and Astronautics Inc, AIAA, 2019. ISBN: 9781624105784. DOI: 10.2514/6.2019-0948.
- [47] Sihao Sun, Coen C. De Visser, and Qiping Chu. "Quadrotor gray-box model identification from high-speed flight data". In: *Journal of Aircraft*. Vol. 56. 2. American Institute of Aeronautics and Astronautics Inc., 2019, pp. 645–661. DOI: 10.2514/1.0035135.
- [48] Sihao Sun and Coen de Visser. "Aerodynamic Model Identification of a Quadrotor Subjected to Rotor Failures in the High-Speed Flight Regime". In: *IEEE Robotics and Automation Letters* 4.4 (July 2019), pp. 3868–3875. DOI: 10.1109/lra.2019.2928758.
- [49] Sihao Sun et al. "High-Speed Flight of Quadrotor Despite Loss of Single Rotor". In: *IEEE Robotics and Automation Letters* 3.4 (Oct. 2018), pp. 3201–3207. ISSN: 23773766. DOI: 10.1109/LRA.2018.2851028.
- [50] Sihao Sun et al. "Incremental nonlinear fault-tolerant control of a quadrotor with complete loss of two opposing rotors". In: *IEEE Transactions on Robotics* 37.1 (2020), pp. 116–130.
- [51] HJ Tol et al. "Multivariate spline-based adaptive control of high-performance aircraft with aerodynamic uncertainties". In: *Journal of Guidance, Control, and Dynamics* 39.4 (2016), pp. 781–800.
- [52] E R Van Oort, Q P Chu, and J A Mulder. *Maneuver Envelope Determination through Reachability Analysis*. Tech. rep.
- [53] C de Visser, J Mulder, and Q Chu. "Global nonlinear aerodynamic model identification with multivariate splines". In: *AIAA atmospheric flight mechanics conference*. 2009, p. 5726.
- [54] Coen C de Visser, QP Chu, and JA Mulder. "A new approach to linear regression with multivariate splines". In: *Automatica* 45.12 (2009), pp. 2903–2909.
- [55] Greg Welch, Gary Bishop, et al. "An introduction to the Kalman filter". In: (1995).
- [56] Y Zhang, CC De Visser, and QP Chu. "Aircraft damage identification and classification for database-driven online flight-envelope prediction". In: *Journal of Guidance, Control, and Dynamics* 41.2 (2018), pp. 449– 460.
- [57] Ye Zhang, Coen C. De Visser, and Q. Ping Chu. "Database building and interpolation for a safe flight envelope prediction system". In: AIAA Information Systems-AIAA Infotech at Aerospace, 2018. 209989. American Institute of Aeronautics and Astronautics Inc, AIAA, Jan. 2018. ISBN: 9781624105272. DOI: 10.2514/6.2018-1635.
- [58] Ye Zhang, Coen C de Visser, and Q Ping Chu. "Online safe flight envelope prediction for damaged aircraft: a database-driven approach". In: *AIAA Modeling and Simulation Technologies Conference*. 2016, p. 1189.

References 69

[59] Ye Zhang et al. "Database-driven safe flight-envelope protection for impaired aircraft". In: *Journal of Aerospace Information Systems* 18.1 (2021), pp. 14–25. ISSN: 23273097. DOI: 10.2514/1.I010846.

[60] Yujiang Zhong et al. "Robust actuator fault detection and diagnosis for a quadrotor UAV with external disturbances". In: *IEEE Access* 6 (2018), pp. 48169–48180.

Part IV Conclusion and Recommendations

Conclusion

The results of the research conducted during this project demonstrated substantial fulfillment of the research objective and provided answers to a majority of the predetermined research inquiries.

It was found that the high-frequency effects caused by damage to the propellers manifest as significant vibrational effects which occur at orders of magnitude higher frequencies than the baseline aerodynamic effects of the quadrotor, allowing for independent modeling of these respective frequency ranges through time-scale separation. The simple composition of these vibrations, comprising of a few dominant sinusoidal components, but complex local non-linear effects in the amplitude variation, meant that a very different model structure was chosen to capture the high-frequency phenomenon compared to the lower-frequency aerodynamic models. A novel approach for modeling the high-frequency phenomenon was developed which employed a two-step process; first, the amplitude-frequency relationships are extracted from the signal, for each dominant harmonic, leading to a scattered dataset, then the amplitude-frequency-damage(level) surfaces are fit using multivariate simplex B-splines. Simplex B-splines offered a much better alternative to polynomial models in describing the high-frequency phenomenon occurring due to blade damage, while also providing an additional advantage in allowing for interpolating the high-frequency dynamics between damage levels used for model identification.

Polynomial models identified through stepwise regression were found to be sufficient in capturing a large part of the low-frequency aerodynamic effects of blade damage. However, these models did not provide a meaningful way to interpolate between damage levels through variations in the model parameters. Based on an analysis of the models, this lack of clear and meaningful parameter variation is thought to be a combination of several factors. Mainly, correlations between dominant model regressors result in sporadic parameter values. Other factors include random changes introduced into the model training data from one damage case to the next because of the inability to manually fly the flight maneuvers in a repeatable and consistent fashion.

In terms of sensor limitation, it was found that accelerometers tend to be the bottleneck rather than gyroscopes by far. The MPU6000 and ICM42605 IMUs have acceleration measurement ranges of ± 16 g, which leads to clipping in the accelerometer caused by high-frequency vibrations at damage levels of around 40% for the quadrotors used for this research. This clipping due to lack of measurement range results in deteriorated attitude estimates. Therefore, conducting system identification experiments with damaged quadrotors proves difficult while flying manually in angle mode. While the attitude estimate is affected severely, the gyroscopes of the aforementioned IMUs (which are also some of the most commonly found IMUs in UAVs), are much more robust to the high-frequency vibrations due to their large measurement range, thus ensuring decent control of angular rates even with PID control algorithms. The use of accelerometers with higher measurement ranges should significantly increase the ability of a quadrotor to survive severe asymmetric damage to the blades because of better attitude control authority. Due to poor accelerometer performance in the presence of blade damage, the aerodynamic forces had to be measured using an external motion capture system, which also inhibits possibilities for purely on-board model identification.

In terms of flight maneuvers flown to identify the aerodynamic and high-frequency models, very different approaches were taken. Since the aerodynamic forces and moments depend on a larger number of states than the high-frequency models, carefully planned flight maneuvers are required that sufficiently excite the aerodynamic forces and moments in all body axes. The high-frequency behavior is found to largely only depend on the frequency of the damaged propeller, and so simple maneuvers which allow for the full range of rotational frequencies of the damaged propeller to be covered are found to be sufficient in capturing the dominant effects.

Lastly, the results of modeling quadrotor behavior in the presence of blade damage also lead to important insights with respect to the detection and diagnosis of these types of faults. The primary result is that while the high-frequency effects captured by the IMU offer a good source of diagnostic information, the high sensitivity of this sensor with respect to the structural frame and its resonant modes makes it a poor choice for a diagnosis method that gives reproducible predictions on different quadrotors of the same make. However, the high sensitivity of this information source also provides the benefits of being able to differentiate between locations of damage on the same quadrotor.

Recommendations

Separate models for quadrotors afflicted with asymmetric blade damage were identified for the low-frequency and high-frequency dynamics. Therefore, the recommendations are also made separately for each model type. First, the low-frequency aerodynamic models are discussed, followed by the high-frequency models. Finally, some insights derived from this research for applications to blade damage diagnosis are discussed.

One of the main limitations of the polynomial aerodynamic models is that they do not seem to show simple, or even physically meaningful patterns in the model parameters as a function of the level of blade damage. Some suggestions that can improve this would be to:

- Perform automated test flights, rather than the manually flown flights in the presented research, to gather data with less variation in terms of coverage of the state space from one damage case to the next
- Relying on external attitude measurements through a motion capture system will allow higher levels of damage to be flown, since the limitation of poor on-board attitude estimates (in the presence of asymmetric blade damage) can be bypassed.
- More coupling between the different forces and moments should be targeted through carefully designed automated test flights, which can improve the coverage of the aerodynamic models.

While the automation of the data collection flights can help with the identification of better models, the problem still remains that the polynomial models may not show clear patterns in the parameters as a function of blade damage because of noise, which the parameters can be highly sensitive to. Another approach to simulate damage cases for which flight data is not recorded would be to take a weighted average between the models at damage levels for which data-driven models are constructed. How exactly two models should be weighted together is therefore an open question, and worth exploring.

While the base assumption of simple sinusoidal components of the high-frequency forces and moments generated by asymmetric blade damage is largely valid, there were some cases where this did not hold. Particularly, at very high frequencies above 400 Hz, the yaw rate signal includes additional low-frequency components which are quite dominant yet sporadic. This phenomenon only occurred on the Beetle quadrotor, however, and not the Geyser. The cause of this should be further investigated.

The high-frequency models only consider the amplitude of the sinusoidal components and not the phase information. Without measurements of motor (angular) position, the absolute phase is impossible to determine for each IMU signal. However, relative phases can be identified for part of the IMU signals as was demonstrated in the paper. Extracting the phase information accurately, however, may require a more involved spectral analysis step.

• The relationships between the relative phases of IMU signals with damage cases should be investigated.

Only damage to a single propeller was considered when constructing the high-frequency models. If linear super-position is assumed to be true, then the IMU signal generated in the presence of dual damage can be simulated by simply adding the sinusoidal components generated by the model for the individual damage locations. However, some considerations have to be made about the relative phase of the two propellers, such as assuming uniform relative phase distribution.

• The super-position assumption should be validated through test flights of quadrotors with damage to two propellers simultaneously.

Damage to more than one propeller also creates challenges in terms of the spectral analysis step. As mentioned in the paper, the short time windows required to capture the non-stationarity of the signal result in lower frequency resolutions. With a single dominant frequency component (and its harmonics), this is not a problem. However, for a quadrotor with damage to more than one propeller, the frequency distance between the rotational speeds of the propellers will likely be within the frequency resolution for a large part of the recorded flight data.

- Maneuvers should be designed which separate the rotational speeds of multiple damaged propellers while
 maintaining significant contributions from the high-frequency effects created by the propellers simultaneously.
- Throttle punch maneuvers coupled with aggressive roll and pitch inputs can be a good choice.

Finally, the simplex-B spline models use a fairly simple triangulation where the vertices all lie on a rectangular grid. While this captured a vast majority of the data, the extremes at the low and high frequencies may be omitted while training.

- The triangulation for HF models can be improved by considering the convex hull of the training dataset.
- The number of simplices should be kept roughly the same as used in this thesis.

The findings of this research also carry significant implications for the diagnosis of asymmetric blade damage. It was found that the high-frequency behavior is very sensitive to not only the damage level of a propeller but also the location. The frequency-amplitude relationships of the IMU measurements for a specific damage case essentially act as fingerprints that facilitate diagnosis. This suggests that a single IMU offers a reliable means of diagnosing several types of damage scenarios. However, the sensitivity comes at the cost of potentially significant variation in the high-frequency behavior for different makes of identical quadrotors due to small variations introduced from one airframe to the other during manufacturing and assembly.

While the aerodynamic models suggest that, for a large part, there are no clear patterns in the model parameters as a function of the damage case, there are a few regressors terms such as w_{tot}^2 for F_z and the moment bias terms which offer a reliable means of blade damage diagnosis. However, purely relying on the low-frequency phenomenon does not allow for differentiation between symmetric and asymmetric blade damage.

Clearly, the high-frequency and low-frequency effects each offer positives and negatives as a means for blade damage diagnosis. Therefore, the ideal approach is to fuse these sources of information such that a robust framework for blade damage diagnosis of quadrotors can be developed.

• A robust blade damage detection and diagnosis scheme should be developed which takes advantage of the high sensitivity of the IMU to small changes in the extent of impairment, while also incorporating aerodynamic model terms from the low-frequency dynamics to potentially make the diagnosis algorithm less system-specific.

Part V Book of Appendices



Aerodynamic Models

The detailed aerodynamic models for all the damage cases outlined in Part II are presented here. Each force and moment model is tabulated, including the regressors, associated parameter values, and the ratio of parameter standard deviation to value (magnitude). It must be noted that the regressor terms related to motor speeds use ERPM rather than RPM. Therefore, simulated rotor RPM values should be divided by 16.67 (the scaling factor in this case) before making predictions with models which contain regressor terms as functions of rotor speeds.

Table A.1: Aerodynamic models for damage case: Healthy at mean airspeed $0 \ ms^{-1}$

(a) F	x
	-

Regressor	Θ	$s(\hat{\Theta})/ \hat{\Theta} $
bias	-5.2840E-02	0.0279
u	-4.8255E-01	0.0022
$\sin(\theta)\omega_{tot}$	-1.7794E-02	0.0041
$\sin(\theta)\omega_{tot}^2$	2.0081E-05	0.0075
$\omega_{tot}q$	-1.1894E-04	0.0136
R^2	0.989	

Regressor	$\hat{\Theta}$	$s(\hat{\Theta})/ \hat{\Theta} $
bias	-6.2371E-04	2.1338
v	-3.6274E-01	0.0026
$\sin(\phi)\omega_{tot}$	1.7597E-02	0.0044
$\sin(\phi)\omega_{tot}^2$	-2.1300E-05	0.0076
$\omega_{tot}p$	9.1245E-05	0.0170
R^2	0.988	

(e) F_z

Regressor	$\hat{\Theta}$	$s(\hat{\Theta})/ \hat{\Theta} $
bias	3.7911E+00	0.0007
w	-8.3394E-02	0.0200
ω_{tot}^2	-2.1184E-05	0.0005
w^2	2.5056E-02	0.0108
$\omega_{tot}w$	-1.8834E-04	0.0203
\mathbb{R}^2	0.993	

(b) M_x

Regressor	Θ	$s(\hat{\Theta})/ \hat{\Theta} $
bias	2.3400E-03	0.0212
p	1.2376E-02	0.0234
u_p	4.8278E-06	0.0016
$\cos(\phi)v$	-8.1734E-03	0.0059
$\cos(\phi)\mu_y\mu_z$	-4.3094E-02	0.0118
$\cos(\phi)p$	-1.3345E-02	0.0227
R^2	0.973	

(d) M_y

Regressor	$\hat{\Theta}$	$s(\hat{\Theta})/ \hat{\Theta} $
bias	5.3251E-03	0.0138
q	-4.1361E-04	0.0722
u_q	-8.2416E-07	0.1182
$\cos(\hat{\theta})u$	1.0497E-02	0.0079
$\cos(\theta)uw$	2.8424E-03	0.0140
$\cos(\theta)u_q$	4.7723E-06	0.0223
R^2	0.949	

Regressor	$\hat{\Theta}$	$s(\hat{\Theta})/ \hat{\Theta} $
bias	4.2621E-03	0.0494
r	-5.3813E-03	0.0124
u_r	-1.3855E-06	0.0097
$ u_q u_r$	7.8573E-11	0.0477
$ u_r \mu_z$	1.7748E-06	0.0405
r w	-1.8940E-03	0.0658
\mathbb{R}^2	0.633	

Table A.2: Aerodynamic models for damage case: Healthy at mean airspeed 8 $\,ms^{-1}$

Regressor	$\hat{\Theta}$	$s(\hat{\Theta})/ \hat{\Theta} $
bias	4.1891E-01	0.0135
u	2.7703E-02	0.0459
$\omega_{tot}u^2$	-3.2925E-04	0.0021
$\sin(\theta)u$	-5.7966E-01	0.0018
$\omega_{tot}u^3$	2.2799E-05	0.0043
R^2	0.958	

Regressor	$\hat{\Theta}$	$s(\hat{\Theta})/ \hat{\Theta} $
bias	-6.7775E-04	0.0725
p	3.2457E-04	0.2983
u_p	4.7942E-06	0.0014
$\sin(\phi) r ^2$	-2.6920E-02	0.0558
$\omega_{tot} u_q u_r $	-5.6009E-14	0.0558
$p\mu_z$	1.3154E-03	0.0670
R^2	0.985	

(c) F_y

Regressor	$\hat{\Theta}$	$s(\hat{\Theta})/ \hat{\Theta} $
bias	-4.3706E-03	0.2130
v	-1.1009E-01	0.0459
$\sin(\phi)\omega_{tot}$	1.5052E-02	0.0074
$\sin(\phi)\omega_{tot}^2$	-1.8681E-05	0.0136
$\omega_{tot}v$	-6.9738E-04	0.0175
\mathbb{R}^2	0.981	

(d) M_y

Regressor	$\hat{\Theta}$	$s(\hat{\Theta})/ \hat{\Theta} $
bias	5.8012E-02	0.0046
q	-9.9511E-04	0.0228
u_q	5.8881E-06	0.0085
μ_z	6.9877E-02	0.0062
μ_z^2	1.6440E-02	0.0114
$\omega_{tot}u_q$	-5.2100E-09	0.0227
R^2	0.932	
IX	0.932	

Regressor	$\hat{\Theta}$	$s(\hat{\Theta})/ \hat{\Theta} $
bias	2.6828E+00	0.0027
w	-2.1523E-01	0.0083
$\frac{\omega_{tot}^2}{\omega_{tot}w^3}$	-2.0700E-05	0.0014
$\omega_{tot}w^3$	-2.9775E-06	0.0153
$\omega_{tot} u ^2w$	5.4770E-06	0.0197
R^2	0.983	

Table A.3: Aerodynamic models for damage case: 10F at mean airspeed 0 ms^{-1}

(a) F_x

Regressor	$\hat{\Theta}$	$s(\hat{\Theta})/ \hat{\Theta} $
bias	5.8051E-03	0.1837
u	-5.0600E-01	0.0022
$\sin(\theta)\omega_{tot}$	-1.7662E-02	0.0046
$\sin(\theta)\omega_{tot}^2$	2.0074E-05	0.0085
$\omega_{tot}q$	-9.7117E-05	0.0109
\mathbb{R}^2	0.986	

Regressor	$\hat{\Theta}$	$s(\hat{\Theta})/ \hat{\Theta} $
bias	5.4986E-03	0.1664
v	-3.4424E-01	0.0019
$\sin(\phi)\omega_{tot}$	1.6022E-02	0.0035
$\sin(\phi)\omega_{tot}^2$	-1.7601E-05	0.0066
$\omega_{tot}p$	8.5009E-05	0.0105
\mathbb{R}^2	0.992	

(e) F_z

Regressor	$\hat{\Theta}$	$s(\hat{\Theta})/ \hat{\Theta} $
bias	3.8767E+00	0.0006
w	-2.7959E-01	0.0045
$\omega_{tot}^2 \\ \omega_{tot} w^2$	-2.0689E-05	0.0005
$\omega_{tot} w^2$	4.2096E-05	0.0157
μ_z	1.2212E-01	0.0174
\mathbb{R}^2	0.994	

(b) M_x

Regressor	$\hat{\Theta}$	$s(\hat{\Theta})/ \hat{\Theta} $
bias	-5.3007E-04	0.0685
p	-3.7570E-04	0.0367
u_p	4.8329E-06	0.0011
$\cos(\phi)v$	-8.6548E-03	0.0055
$\cos(\phi)\mu_y\mu_z$	-3.4623E-02	0.0205
$\sin(\phi)\omega_{tot}^2$	2.0624E-08	0.0293
\mathbb{R}^2	0.986	

(d) M_y

Regressor	$\hat{\Theta}$	$s(\hat{\Theta})/ \hat{\Theta} $
bias	-3.6714E-03	0.0099
q	-5.7185E-04	0.0261
u_q	-8.3674E-07	0.0581
$\cos(\hat{\theta})\mu_x$	4.3002E-02	0.0053
$\cos(\theta)\mu_x\mu_z$	6.6486E-02	0.0095
$\cos(\theta)u_q$	4.7011E-06	0.0112
\mathbb{R}^2	0.981	

Regressor	$\hat{\Theta}$	$s(\hat{\Theta})/ \hat{\Theta} $
bias	-5.6364E-06	27.8675
r	-4.1067E-03	0.0154
u_r	-1.1379E-06	0.0107
$ u_r v w$	1.1457E-06	0.0548
$\omega_{tot} q r$	-1.1748E-05	0.0579
$\omega_{tot} u_p u_r$	1.3765E-13	0.0742
R^2	0.609	

Table A.4: Aerodynamic models for damage case: 10F at mean airspeed 8 ms^{-1}

(a)	F_x

Regressor	$\hat{\Theta}$	$s(\hat{\Theta})/ \hat{\Theta} $
bias	1.4163E+00	0.0064
u	-2.4975E-01	0.0075
$\sin(\theta)\mu_x$	-2.3026E+00	0.0027
$\sin(\theta)\mu_x^2$	3.3035E-01	0.0038
$\omega_{tot}u$	-6.9338E-04	0.0044
R^2	0.936	

Regressor	$\hat{\Theta}$	$s(\hat{\Theta})/ \hat{\Theta} $
bias	2.1451E-04	0.2827
p	-4.4635E-04	0.0367
u_p	4.5663E-06	0.0014
$\cos(\phi) u vw$	-4.3573E-05	0.0514
$ u_r u ^2w$	1.0475E-09	0.0512
r v	1.6569E-03	0.0822
\mathbb{R}^2	0.986	

(c) F_y

Regressor	$\hat{\Theta}$	$s(\hat{\Theta})/ \hat{\Theta} $
bias	-6.0000E-03	0.2195
v	-4.0528E-01	0.0036
$\sin(\phi)\omega_{tot}$	7.2566E-03	0.0040
pw^3	-1.6826E-04	0.0302
$\sin(\phi)w^3$	2.6199E-03	0.0314
\mathbb{R}^2	0.978	

(d) M_y

Regressor	$\hat{\Theta}$	$s(\hat{\Theta})/ \hat{\Theta} $
bias	4.4476E-02	0.0047
q	-1.0918E-03	0.0199
u_q	5.3871E-06	0.0085
w	1.5626E-02	0.0052
w^2	8.6332E-04	0.0095
$\omega_{tot}u_q$	-4.3155E-09	0.0242
\mathbb{R}^2	0.921	

Regressor	$\hat{\Theta}$	$s(\hat{\Theta})/ \hat{\Theta} $
bias	2.5594E+00	0.0039
w	-2.0009E-01	0.0108
$\frac{\omega_{tot}^2}{\omega_{tot}w^3}$	-2.0762E-05	0.0011
$\omega_{tot}w^3$	-3.2476E-06	0.0187
$ q \mu_x $	5.2650E-02	0.0348
\mathbb{R}^2	0.972	

Table A.5: Aerodynamic models for damage case: 10BL at mean airspeed 0 ms^{-1}

(a) F_x
()

Regressor	$\hat{\Theta}$	$s(\hat{\Theta})/ \hat{\Theta} $
bias	-5.3349E-02	0.0259
u	2.2131E-01	0.0289
$\sin(\theta)\omega_{tot}$	-1.5288E-02	0.0042
$\omega_{tot}u$	-1.6551E-03	0.0084
$\sin(\theta)\omega_{tot}^2$	1.4604E-05	0.0090
R^2	0.975	

Regressor	$\hat{\Theta}$	$s(\hat{\Theta})/ \hat{\Theta} $
bias	1.8029E-02	0.0484
v	-3.5578E-01	0.0018
$\sin(\phi)\omega_{tot}$	1.6244E-02	0.0034
$\sin(\phi)\omega_{tot}^2$	-1.8086E-05	0.0062
$\omega_{tot}p$	8.0566E-05	0.0102
\mathbb{R}^2	0.992	

(e) F_z

Regressor	$\hat{\Theta}$	$s(\hat{\Theta})/ \hat{\Theta} $
bias	3.8538E+00	0.0006
w	-1.9939E-01	0.0039
ω_{tot}^2	-2.1112E-05	0.0005
$\omega_{tot} w^2$	8.0780E-05	0.0091
$\omega_{tot} u w^2$	-1.5549E-04	0.0140
\mathbb{R}^2	0.994	

(b) M_x

Regressor	$\hat{\Theta}$	$s(\hat{\Theta})/ \hat{\Theta} $
bias	-5.1669E-03	0.0075
p	8.4409E-03	0.0433
u_p	4.8090E-06	0.0010
$\cos(\phi)v$	-7.5977E-03	0.0098
$\cos(\phi)\mu_y\mu_z$	-5.0412E-02	0.0204
$\cos(\phi)p$	-9.0516E-03	0.0415
\mathbb{R}^2	0.984	

(d) M_y

Regressor	$\hat{\Theta}$	$s(\hat{\Theta})/ \hat{\Theta} $
bias	7.3851E-03	0.0076
q	-2.0396E-04	0.0925
u_q	8.0771E-06	0.0073
$u_q u^2$	-4.6008E-08	0.0156
$\omega_{tot}u_q$	-1.0274E-08	0.0130
$\omega_{tot}u$	7.1622E-06	0.0150
R^2	0.973	

Regressor	$\hat{\Theta}$	$s(\hat{\Theta})/ \hat{\Theta} $
bias	1.8112E-03	0.1029
r	-3.9613E-03	0.0164
u_r	-1.0710E-06	0.0067
q r	-3.4237E-02	0.0390
$\omega_{tot} q r$	7.2692E-05	0.0445
$\omega_{tot} u_q ^2$	-3.0134E-13	0.0617
R^2	0.616	

Table A.6: Aerodynamic models for damage case: 10BL at mean airspeed 8 ms^{-1}

Regressor	$\hat{\Theta}$	$s(\hat{\Theta})/ \hat{\Theta} $
bias	1.7433E+00	0.0028
u	-5.3247E-02	0.0197
$\sin(\theta)\mu_x$	3.9734E-01	0.0081
$\omega_{tot}u$	-1.3718E-03	0.0015
$\sin(\theta)u$	-6.2371E-01	0.0018
R^2	0.975	

Regressor	$\hat{\Theta}$	$s(\hat{\Theta})/ \hat{\Theta} $
bias	-5.1081E-03	0.0104
p	-1.3673E-03	0.0123
u_p	4.6812E-06	0.0015
$\sin(\dot{\phi})p^2$	-3.3762E-04	0.0595
$\sin(\phi)v^3$	2.6162E-04	0.0563
$ r vw^2$	1.5286E-04	0.0622
R^2	0.987	

(c) F_y

Regressor	$\hat{\Theta}$	$s(\hat{\Theta})/ \hat{\Theta} $
bias	-7.1312E-03	0.3166
v	-5.4263E-02	0.2721
$\sin(\phi)\omega_{tot}$	1.7539E-02	0.0120
$\sin(\phi)\omega_{tot}^2$	-2.4643E-05	0.0195
$\omega_{tot}v$	-8.3024E-04	0.0404
R^2	0.963	

(d) M_y

Regressor	$\hat{\Theta}$	$s(\hat{\Theta})/ \hat{\Theta} $
bias	4.2804E-02	0.0084
q	-8.2350E-04	0.0497
u_q	6.1768E-06	0.0156
μ_z	3.3279E-02	0.0088
$\sin(\theta)u_q$	-1.1262E-06	0.0198
$\omega_{tot}u_q$	-7.2931E-09	0.0306
R^2	0.809	

(e) F_z

Regressor	Θ	$s(\hat{\Theta})/ \hat{\Theta} $
bias	2.7489E+00	0.0029
w	-1.4105E-01	0.0120
$\omega_{tot}^2 \ \omega_{tot} w^3$	-2.1064E-05	0.0009
$\omega_{tot}w^3$	-3.8583E-06	0.0122
$ q \mu_x $	5.0520E-02	0.0286
R^2	0.980	

Table A.7: Aerodynamic models for damage case: 10FL at mean airspeed 0 ms^{-1}

Regressor	$\hat{\Theta}$	$s(\hat{\Theta})/ \hat{\Theta} $
bias	-4.3101E-02	0.0234
u	-1.0294E+00	0.0054
$\sin(\theta)\omega_{tot}$	-1.6855E-02	0.0036
$\sin(\theta)\omega_{tot}^2$	1.7453E-05	0.0070
μ_x	2.0301E+00	0.0123
\mathbb{R}^2	0.987	

Regressor	$\hat{\Theta}$	$s(\hat{\Theta})/ \hat{\Theta} $
bias	5.4969E-03	0.2351
v	-3.7947E-01	0.0026
$\sin(\phi)\omega_{tot}$	1.6772E-02	0.0038
$\sin(\phi)\omega_{tot}^2$	-1.9045E-05	0.0067
$\omega_{tot}p$	6.6510E-05	0.0197
\mathbb{R}^2	0.984	

(e) F_z

Regressor	$\hat{\Theta}$	$s(\hat{\Theta})/ \hat{\Theta} $
bias	3.8506E+00	0.0009
w	-2.0701E-01	0.0053
ω_{tot}^2	-2.0512E-05	0.0007
$\omega_{tot} r $	-5.0442E-04	0.0105
$\omega_{tot} v $	-6.8292E-04	0.0138
\mathbb{R}^2	0.984	

(b) M_x

Regressor	$\hat{\Theta}$	$s(\hat{\Theta})/ \hat{\Theta} $
bias	-5.2516E-03	0.0098
p	-1.5500E-04	0.1281
u_p	7.8342E-06	0.0092
$\cos(\phi)v$	-7.6658E-03	0.0075
$\cos(\phi)vw$	-1.6439E-03	0.0171
$\omega_{tot}u_p$	-6.7936E-09	0.0241
\mathbb{R}^2	0.976	

(d) M_y

Regressor	$\hat{\Theta}$	$s(\hat{\Theta})/ \hat{\Theta} $
bias	1.4196E-03	0.0390
q	-4.7155E-04	0.0430
u_q	-2.3070E-07	0.3153
$\cos(\hat{\theta})u$	9.6599E-03	0.0059
$\sin(\theta)u^2$	2.1429E-03	0.0135
$\cos(\theta)u_q$	4.0564E-06	0.0191
\mathbb{R}^2	0.974	

Regressor	$\hat{\Theta}$	$s(\hat{\Theta})/ \hat{\Theta} $
bias	-1.8034E-02	0.0700
r	-1.4973E-02	0.0283
u_r	-2.3956E-06	0.0265
$\cos(\theta)\omega_{tot}$	5.4174E-05	0.0588
$\omega_{tot}r$	2.5705E-05	0.0431
$\omega_{tot}u_r$	3.3325E-09	0.0468
R^2	0.677	

Table A.8: Aerodynamic models for damage case: 10FL at mean airspeed 8 ms^{-1}

Regr	essor	$\hat{\Theta}$	$s(\hat{\Theta})/ \hat{\Theta} $
bi	as	1.9705E+00	0.0025
i	u	-1.1535E-01	0.0065
ω_t	$_{ot}u$	-1.3026E-03	0.0010
sin($(\theta)u$	-5.9848E-01	0.0014
ω_{tot}	$u_x \mu_z$	4.7076E-04	0.0053
R	\mathcal{L}^2	0.981	

Regressor	$\hat{\Theta}$	$s(\hat{\Theta})/ \hat{\Theta} $
bias	1.9485E-03	0.1382
p	-8.3488E-04	0.0181
u_p	4.7381E-06	0.0014
$\omega_{tot}w$	8.3824E-06	0.0361
$\omega_{tot}w^2$	8.6539E-07	0.0443
$\sin(\phi) u_r $	-6.6441E-07	0.0476
\mathbb{R}^2	0.987	

(c) F_y

Regressor	$\hat{\Theta}$	$s(\hat{\Theta})/ \hat{\Theta} $
bias	2.2963E-02	0.0783
v	-7.4261E-01	0.0106
$\sin(\phi)\omega_{tot}$	6.3700E-03	0.0038
p	-2.5770E-02	0.0214
μ_y	1.1731E+00	0.0268
R^2	0.974	

(d) M_y

Regressor	$\hat{\Theta}$	$s(\hat{\Theta})/ \hat{\Theta} $
bias	5.3857E-02	0.0050
q	-7.7637E-04	0.0312
u_q	5.6490E-06	0.0092
\vec{w}	1.6930E-02	0.0058
$\omega_{tot}w^2$	2.1976E-06	0.0103
$\omega_{tot}u_q$	-4.8118E-09	0.0252
R^2	0.932	

	^	^ ^
Regressor	Θ	$s(\hat{\Theta})/ \hat{\Theta} $
bias	3.1679E+00	0.0035
w	1.1302E-02	0.2914
$\frac{\omega_{tot}^2}{w^2}$	-1.9243E-05	0.0020
	2.8691E-02	0.0121
$\omega_{tot} u $	-2.1267E-04	0.0234
\mathbb{R}^2	0.983	

Table A.9: Aerodynamic models for damage case: 20F at mean airspeed 0 ms^{-1}

(a) F_x	
-----------	--

Regressor	$\hat{\Theta}$	$s(\hat{\Theta})/ \hat{\Theta} $
bias	-2.5914E-02	0.0531
u	-5.6548E-01	0.0025
$\sin(\theta)\omega_{tot}$	-1.8811E-02	0.0044
$\sin(\theta)\omega_{tot}^2$	2.1428E-05	0.0078
$\omega_{tot}q$	-6.6302E-05	0.0176
\mathbb{R}^2	0.983	

Regressor	$\hat{\Theta}$	$s(\hat{\Theta})/ \hat{\Theta} $
bias	8.1806E-03	0.1315
v	-3.9190E-01	0.0019
$\sin(\phi)\omega_{tot}$	1.7888E-02	0.0043
$\sin(\phi)\omega_{tot}^2$	-2.0689E-05	0.0076
$\omega_{tot}p$	5.0957E-05	0.0186
R^2	0.990	

(e) F_z

Regressor	$\hat{\Theta}$	$s(\hat{\Theta})/ \hat{\Theta} $
bias	3.8309E+00	0.0005
w	-1.2551E-01	0.0107
ω_{tot}^2	-1.9938E-05	0.0004
w^2	2.0793E-02	0.0127
$\omega_{tot}w$	-2.3325E-04	0.0131
\mathbb{R}^2	0.996	

(b) M_x

Regressor	Θ	$s(\hat{\Theta})/ \hat{\Theta} $
bias	2.2108E-03	0.0190
p	-4.0386E-04	0.0402
u_p	4.5856E-06	0.0011
$\cos(\phi)v$	-8.2738E-03	0.0059
$\sin(\phi) u_r ^2$	1.2757E-10	0.0136
$\cos(\phi)vw$	-1.6843E-03	0.0138
\mathbb{R}^2	0.975	

(d) M_y

Regressor	$\hat{\Theta}$	$s(\hat{\Theta})/ \hat{\Theta} $
bias	-7.3048E-03	0.0064
q	-7.1125E-04	0.0245
u_q	-4.4100E-07	0.1339
$\cos(\hat{\theta})\mu_x$	4.7114E-02	0.0060
$\cos(\theta)\mu_x\mu_z$	6.6608E-02	0.0115
$\cos(\theta)u_q$	4.1361E-06	0.0153
R^2	0.974	

Regressor	$\hat{\Theta}$	$s(\hat{\Theta})/ \hat{\Theta} $
bias	1.8493E-03	0.1279
r	-4.1779E-03	0.0246
u_r	-1.0077E-06	0.0100
q r	-5.5144E-03	0.0609
$ u_p ^2$	-1.7766E-09	0.0664
$\omega_{tot} u_p ^2$	3.9571E-12	0.0726
R^2	0.528	

Table A.10: Aerodynamic models for damage case: 20F at mean airspeed 8 ms^{-1}

Regressor	$\hat{\Theta}$	$s(\hat{\Theta})/ \hat{\Theta} $
bias	-8.9793E-02	0.0811
u	-6.2315E-02	0.0399
$\sin(\theta)\mu_x$	-2.6162E+00	0.0025
$\sin(\theta)\mu_x^2$	3.9255E-01	0.0035
$\omega_{tot}u^2$	-9.4330E-05	0.0053
R^2	0.932	

Regressor	$\hat{\Theta}$	$s(\hat{\Theta})/ \hat{\Theta} $
bias	1.2574E-03	0.0388
p	-3.7525E-04	0.0414
u_p	4.4870E-06	0.0015
$\sin(\hat{\phi}) r $	-1.5515E-02	0.0393
$\cos(\phi)v^2w$	-7.2201E-05	0.0540
$p u ^2v$	5.0244E-06	0.0675
\mathbb{R}^2	0.985	

(c) F_y

Regressor	$\hat{\Theta}$	$s(\hat{\Theta})/ \hat{\Theta} $
bias	-7.3422E-03	0.2789
v	2.2464E-01	0.0754
$\sin(\phi)\omega_{tot}$	1.8561E-02	0.0102
$\sin(\phi)\omega_{tot}^2$	-2.6891E-05	0.0154
$\omega_{tot}v$	-1.3888E-03	0.0267
R^2	0.981	

(d) M_y

Regressor	$\hat{\Theta}$	$s(\hat{\Theta})/ \hat{\Theta} $
bias	3.9870E-02	0.0051
q	-1.0328E-03	0.0212
u_q	5.2357E-06	0.0093
\dot{w}	1.6213E-02	0.0052
w^2	9.1824E-04	0.0096
$\omega_{tot}u_q$	-3.9667E-09	0.0286
R^2	0.935	

Regressor	Θ	$s(\hat{\Theta})/ \hat{\Theta} $
bias	2.5886E+00	0.0031
w	-2.1329E-01	0.0093
$\frac{\omega_{tot}^2}{\omega_{tot}w^3}$	-1.9510E-05	0.0013
$\omega_{tot}w^3$	-4.8042E-06	0.0167
$\omega_{tot} u w^2$	-4.8707E-06	0.0339
R^2	0.982	

Table A.11: Aerodynamic models for damage case: 20BL at mean airspeed 0 $\,ms^{-1}$

(a) F_x
()

Regressor	Θ	$s(\hat{\Theta})/ \hat{\Theta} $
bias	-5.7676E-02	0.0250
u	-5.0306E-01	0.0028
$\sin(\theta)\omega_{tot}$	-1.8180E-02	0.0052
$\sin(\theta)\omega_{tot}^2$	2.0894E-05	0.0094
$\omega_{tot}q$	-9.3142E-05	0.0134
\mathbb{R}^2	0.984	

Regressor	$\hat{\Theta}$	$s(\hat{\Theta})/ \hat{\Theta} $
bias	4.3229E-03	0.1933
v	-3.5666E-01	0.0016
$\sin(\phi)\omega_{tot}$	1.5854E-02	0.0034
$\sin(\phi)\omega_{tot}^2$	-1.7149E-05	0.0064
$\omega_{tot}p$	8.0540E-05	0.0097
\mathbb{R}^2	0.994	

(e) F_z

Regressor	$\hat{\Theta}$	$s(\hat{\Theta})/ \hat{\Theta} $
bias	3.7807E+00	0.0005
w	-1.3415E-01	0.0111
$w_{tot}^2 \ w^2$	-2.0319E-05	0.0004
w^2	2.8880E-02	0.0100
$\omega_{tot}w$	-1.4669E-04	0.0231
R^2	0.996	

(b) M_x

Regressor	$\hat{\Theta}$	$s(\hat{\Theta})/ \hat{\Theta} $
bias	-8.3267E-03	0.0062
p	-3.0979E-04	0.0664
u_p	1.3188E-06	0.0632
$\cos(\phi)v$	-8.6884E-03	0.0070
$\sin(\phi)\mu_y^2$	3.5621E-02	0.0152
$\cos(\phi)u_p$	3.6830E-06	0.0246
R^2	0.957	

(d) M_y

Regressor	$\hat{\Theta}$	$s(\hat{\Theta})/ \hat{\Theta} $
bias	1.1011E-02	0.0052
q	-3.6034E-04	0.0590
u_q	7.9313E-08	0.9542
$\cos(\hat{\theta})\mu_x$	3.9729E-02	0.0097
$\cos(\theta)\mu_x\mu_z$	5.9145E-02	0.0165
$\cos(\theta)u_q$	3.7179E-06	0.0218
\mathbb{R}^2	0.967	

Regressor	$\hat{\Theta}$	$s(\hat{\Theta})/ \hat{\Theta} $
bias	-2.8593E-03	0.1209
r	-4.1450E-03	0.0298
u_r	-1.0085E-06	0.0168
$\sin(\phi) u ^2w$	-1.4980E-01	0.1181
$ r u w^2$	4.6629E-03	0.1069
$ u_q \mu_z^2$	-1.4876E-05	0.1653
\mathbb{R}^2	0.301	

Table A.12: Aerodynamic models for damage case: 20BL at mean airspeed 8 ms^{-1}

Regressor	$\hat{\Theta}$	$s(\hat{\Theta})/ \hat{\Theta} $
bias	9.3989E-01	0.0089
u	-1.9534E-01	0.0083
$\sin(\theta)\mu_x$	-2.3494E+00	0.0023
$\sin(\theta)\mu_x^2$	3.2766E-01	0.0030
$\omega_{tot}u$	-6.4001E-04	0.0041
R^2	0.938	

Regressor	$\hat{\Theta}$	$s(\hat{\Theta})/ \hat{\Theta} $
bias	-1.3530E-02	0.0160
p	5.1561E-03	0.0746
u_p	4.5737E-06	0.0015
$ \mu_x \mu_z$	-3.4403E-03	0.0406
$ r \mu_y\mu_z$	-1.3597E-02	0.0545
$\cos(\phi)p$	-6.8396E-03	0.0580
R^2	0.984	

(c) F_y

Regressor	$\hat{\Theta}$	$s(\hat{\Theta})/ \hat{\Theta} $
bias	4.6123E-03	0.3253
v	-7.6568E-01	0.0171
$\sin(\phi)\omega_{tot}$	1.4681E-02	0.0118
$\sin(\phi)\omega_{tot}^2$	-1.8130E-05	0.0220
μ_y	1.4669E+00	0.0371
R^2	0.990	

(d) M_y

Regressor	$\hat{\Theta}$	$s(\hat{\Theta})/ \hat{\Theta} $
bias	4.6093E-02	0.0032
q	-8.2098E-04	0.0216
u_q	5.9523E-06	0.0060
μ_z	3.5053E-02	0.0034
$u_q \mu_z^2$	4.5360E-07	0.0114
$\omega_{tot}u_q$	-6.8312E-09	0.0118
\mathbb{R}^2	0.959	

(e) F_z

Regressor	Θ	$s(\hat{\Theta})/ \hat{\Theta} $
bias	3.0977E+00	0.0029
w	-5.6413E-03	0.4798
$\frac{\omega_{tot}^2}{w^3}$	-2.0101E-05	0.0007
w^3	-3.4772E-03	0.0099
$ u_q u ^2 v $	-6.9636E-07	0.0223
\mathbb{R}^2	0.981	

Table A.13: Aerodynamic models for damage case: 20BR at mean airspeed 0 ms^{-1}

(a)	F_x
()	

Regressor	$\hat{\Theta}$	$s(\hat{\Theta})/ \hat{\Theta} $
bias	-3.0818E-02	0.0319
u	-5.2949E-01	0.0016
$\sin(\theta)\omega_{tot}$	-1.6721E-02	0.0040
$\sin(\theta)\omega_{tot}^2$	1.7660E-05	0.0079
$\omega_{tot}q$	-9.5031E-05	0.0098
R^2	0.992	

Regressor	Θ	$s(\hat{\Theta})/ \hat{\Theta} $
bias	8.1839E-04	1.2933
v	-3.7291E-01	0.0020
$\sin(\phi)\omega_{tot}$	1.7129E-02	0.0042
$\sin(\phi)\omega_{tot}^2$	-1.9584E-05	0.0076
$\omega_{tot}p$	6.8866E-05	0.0139
R^2	0.990	

(e) F_z

Regressor	$\hat{\Theta}$	$s(\hat{\Theta})/ \hat{\Theta} $
bias	3.7930E+00	0.0006
w	-1.1734E-01	0.0139
ω_{tot}^2	-2.0533E-05	0.0005
w^2	2.5118E-02	0.0121
$\omega_{tot}w$	-2.3021E-04	0.0164
R^2	0.996	

(b) M_x

Regressor	Θ	$s(\hat{\Theta})/ \hat{\Theta} $
bias	9.5475E-03	0.0069
p	-3.0326E-04	0.0517
u_p	4.7963E-06	0.0010
$\cos(\phi)v$	-8.5011E-03	0.0054
$\cos(\phi)\mu_y\mu_z$	-4.5458E-02	0.0109
$\omega_{tot} u_r $	1.3720E-09	0.0193
\mathbb{R}^2	0.980	

(d) M_y

Regressor	Θ	$s(\hat{\Theta})/ \hat{\Theta} $
bias	1.0924E-02	0.0055
q	-4.9829E-04	0.0428
u_q	4.0164E-07	0.1764
$\cos(\theta)\mu_x$	3.9706E-02	0.0072
$\sin(\theta)\mu_x^2$	4.7821E-02	0.0133
$\cos(\theta)u_q$	3.3869E-06	0.0224
\mathbb{R}^2	0.962	

Regressor	$\hat{\Theta}$	$s(\hat{\Theta})/ \hat{\Theta} $
bias	2.6640E-03	0.0662
r	-3.1648E-03	0.0233
u_r	-1.2810E-06	0.0136
p r	-9.4130E-02	0.0385
$\omega_{tot} p r$	2.1171E-04	0.0414
$\omega_{tot} u_q u_r$	1.6624E-13	0.0571
\mathbb{R}^2	0.469	

Table A.14: Aerodynamic models for damage case: 20BR at mean airspeed 8 ms^{-1}

	Regressor	$\hat{\Theta}$	$s(\hat{\Theta})/ \hat{\Theta} $
	bias	8.5359E-01	0.0111
	u	-1.8802E-01	0.0104
	$\sin(\theta)\mu_x$	-2.5961E+00	0.0027
	$\sin(\theta)\mu_x^2$	4.0914E-01	0.0038
	$\omega_{tot}u$	-6.6837E-04	0.0048
_	\mathbb{R}^2	0.953	

Regressor	$\hat{\Theta}$	$s(\hat{\Theta})/ \hat{\Theta} $
bias	-1.5930E-03	0.3352
p	-1.6566E-03	0.0181
u_p	3.9117E-06	0.0132
$\omega_{tot} u_q ^2$	7.6146E-14	0.0338
$\cos(\phi)\omega_{tot}^2$	5.9023E-08	0.0494
$u_p \mu_x \mu_z$	-5.7292E-07	0.0657
R^2	0.962	

(c) F_y

Regressor	Θ	$s(\hat{\Theta})/ \hat{\Theta} $
bias	-1.4216E-02	0.0776
v	-3.9761E-01	0.0040
$\sin(\phi)\omega_{tot}$	1.1457E-02	0.0103
$\sin(\phi)\omega_{tot}^2$	-1.0726E-05	0.0247
p	-1.3164E-02	0.0308
R^2	0.991	

(d) M_y

Regressor	$\hat{\Theta}$	$s(\hat{\Theta})/ \hat{\Theta} $
bias	4.5909E-02	0.0107
q	-8.9625E-04	0.0548
u_q	6.3281E-06	0.0212
μ_z	3.3589E-02	0.0119
$u_q \mu_x \mu_z$	-3.8354E-07	0.0289
$\omega_{tot}u_q$	-7.7672E-09	0.0396
\mathbb{R}^2	0.827	

Regressor	Θ	$s(\hat{\Theta})/ \hat{\Theta} $
	2.02005.00	. ,,,,,
bias	2.8309E+00	0.0045
w	-3.2735E-03	1.5840
$w_{tot}^2 \ w^2$	-2.0296E-05	0.0008
w^2	2.9265E-02	0.0177
$\omega_{tot} q ^2$	4.5068E-04	0.0293
\mathbb{R}^2	0.982	

Table A.15: Aerodynamic models for damage case: 20FL at mean airspeed 0 ms^{-1}

(a)	F_x
()	

Regressor	$\hat{\Theta}$	$s(\hat{\Theta})/ \hat{\Theta} $
bias	-4.2001E-02	0.0323
u	-5.1115E-01	0.0022
$\sin(\theta)\omega_{tot}$	-1.9296E-02	0.0042
$\sin(\theta)\omega_{tot}^2$	2.3214E-05	0.0071
q	-4.1471E-02	0.0128
R^2	0.986	

Regressor	Θ	$s(\hat{\Theta})/ \hat{\Theta} $
bias	-7.8623E-03	0.1307
v	-3.5599E-01	0.0020
$\sin(\phi)\omega_{tot}$	1.6755E-02	0.0038
$\sin(\phi)\omega_{tot}^2$	-1.9007E-05	0.0068
$\omega_{tot}p$	8.6542E-05	0.0128
\mathbb{R}^2	0.993	

(e) F_z

Regressor	$\hat{\Theta}$	$s(\hat{\Theta})/ \hat{\Theta} $
bias	3.8413E+00	0.0005
w	-1.8896E-01	0.0049
ω_{tot}^2	-2.0679E-05	0.0004
$\omega_{tot} w^2$	6.3003E-05	0.0105
$\omega_{tot} u w$	-3.7099E-04	0.0158
\mathbb{R}^2	0.995	

(b) M_x

	^	^ ^
Regressor	$\hat{\Theta}$	$s(\hat{\Theta})/ \hat{\Theta} $
bias	-8.0181E-03	0.0051
p	-1.1451E-04	0.1406
u_p	4.7574E-06	0.0010
$\cos(\phi)v$	5.3412E-04	0.3873
$\cos(\phi)\mu_y\mu_z$	-5.3563E-02	0.0095
$\omega_{tot}v$	-1.6928E-05	0.0209
R^2	0.979	

(d) M_y

Regressor	$\hat{\Theta}$	$s(\hat{\Theta})/ \hat{\Theta} $
bias	-1.2118E-03	0.0360
q	-6.2134E-04	0.0263
u_q	-4.2449E-07	0.1188
$\cos(\hat{\theta})\mu_x$	4.7382E-02	0.0050
$\cos(\theta)\mu_x\mu_z$	5.6939E-02	0.0101
$\cos(\theta)u_q$	4.2585E-06	0.0128
\mathbb{R}^2	0.980	

Regressor	$\hat{\Theta}$	$s(\hat{\Theta})/ \hat{\Theta} $
bias	-3.1655E-02	0.0821
r	-3.5580E-03	0.0219
u_r	-1.0125E-06	0.0088
p r	-7.8002E-03	0.0543
$\cos(\theta)\omega_{tot}$	9.6140E-05	0.0655
$ u_q $	-1.6217E-06	0.0843
R^2	0.556	

Table A.16: Aerodynamic models for damage case: 20FL at mean airspeed 8 ms^{-1}

Regressor	$\hat{\Theta}$	$s(\hat{\Theta})/ \hat{\Theta} $
bias	-3.5017E-01	0.0267
u	5.2048E-02	0.0512
$\sin(\theta)\mu_x$	-2.3587E+00	0.0027
$\sin(\theta)\mu_x^2$	3.5796E-01	0.0035
$\omega_{tot}u^2$	-1.1508E-04	0.0043
R^2	0.945	

Regressor	$\hat{\Theta}$	$s(\hat{\Theta})/ \hat{\Theta} $
bias	-1.2494E-03	0.2607
p	-7.5617E-04	0.0183
u_p	4.7089E-06	0.0014
$\sin(\phi) u_q $	-9.4497E-07	0.0409
$\cos(\phi)\omega_{tot}^2$	-4.5451E-08	0.0409
$\cos(\phi) u_q u_r $	-1.7197E-11	0.0541
\mathbb{R}^2	0.989	

(c) F_y

Regressor	$\hat{\Theta}$	$s(\hat{\Theta})/ \hat{\Theta} $
bias	1.2176E-02	0.2160
v	-3.6882E-01	0.0063
$\sin(\phi)\omega_{tot}$	1.1773E-02	0.0262
$\omega_{tot}v^2w$	8.4278E-06	0.0475
$\sin(\phi)\omega_{tot}^2$	-1.1296E-05	0.0625
\mathbb{R}^2	0.963	

(d) M_y

Regressor	Ĥ	$s(\hat{\Theta})/ \hat{\Theta} $
Regressor		3(0)/ 0
bias	4.0599E-02	0.0147
q	-1.3145E-03	0.0242
u_q	3.7031E-06	0.0028
\overline{w}	1.7845E-02	0.0089
w^2	1.1570E-03	0.0151
$\cos(\theta)\omega_{tot}^2$	6.8048E-08	0.0397
R^2	0.902	

(e) F_z

Regressor	$\hat{\Theta}$	$s(\hat{\Theta})/ \hat{\Theta} $
bias	2.6993E+00	0.0034
w	-1.6314E-01	0.0126
$\omega_{tot}^2 \\ \omega_{tot} w^3$	-2.0837E-05	0.0010
$\omega_{tot}w^3$	-3.3619E-06	0.0166
p q	8.5650E-01	0.0300
\mathbb{R}^2	0.976	

Table A.17: Aerodynamic models for damage case: 30F at mean airspeed 0 ms^{-1}

Regressor	Θ	$s(\hat{\Theta})/ \hat{\Theta} $
bias	-2.3512E-02	0.0420
u	-5.2190E-01	0.0015
$\sin(\theta)\omega_{tot}$	-1.7869E-02	0.0034
$\sin(\theta)\omega_{tot}^2$	1.9489E-05	0.0063
$\omega_{tot}q$	-6.0540E-05	0.0150
R^2	0.993	

Regressor	$\hat{\Theta}$	$s(\hat{\Theta})/ \hat{\Theta} $
bias	2.8392E-02	0.0242
v	-3.6037E-01	0.0018
$\sin(\phi)\omega_{tot}$	1.8074E-02	0.0029
$\sin(\phi)\omega_{tot}^2$	-2.1277E-05	0.0051
$\omega_{tot}p$	6.1962E-05	0.0105
R^2	0.994	

(e) F_z

Regressor	$\hat{\Theta}$	$s(\hat{\Theta})/ \hat{\Theta} $
bias	3.8019E+00	0.0006
w	-1.5736E-01	0.0140
ω_{tot}^2	-1.9273E-05	0.0005
$\omega_{tot} w^2$	3.7656E-05	0.0270
$\omega_{tot}w$	-1.2567E-04	0.0404
\mathbb{R}^2	0.996	

(b) M_x

Regressor	Θ	$s(\hat{\Theta})/ \hat{\Theta} $
bias	6.5207E-04	0.0700
p	-2.8328E-04	0.0610
u_p	4.6235E-06	0.0014
μ_y	-3.0441E-02	0.0154
$\cos(\phi)u_p u_r $	-5.3975E-11	0.0186
$ u_r \mu_y$	1.4310E-06	0.0327
R^2	0.979	

(d) M_y

Regressor	$\hat{\Theta}$	$s(\hat{\Theta})/ \hat{\Theta} $
bias	-1.0992E-02	0.0055
q	-7.3241E-04	0.0300
u_q	7.2606E-07	0.1326
$\cos(\hat{\theta})u$	1.0057E-02	0.0090
$\cos(\theta)\mu_x\mu_z$	7.3262E-02	0.0213
$\cos(\theta)u_q$	2.8047E-06	0.0363
\mathbb{R}^2	0.967	

Regressor	$\hat{\Theta}$	$s(\hat{\Theta})/ \hat{\Theta} $
bias	1.2492E-03	0.1684
r	-5.3660E-03	0.0175
u_r	-1.0189E-06	0.0109
$ u_r \mu_z$	1.9518E-06	0.0679
$ u_r u w$	-8.0554E-07	0.0720
$ q \mu_z^2$	-2.9772E-01	0.0907
R^2	0.530	

Table A.18: Aerodynamic models for damage case: 30F at mean airspeed 8 ms^{-1}

Regressor	$\hat{\Theta}$	$s(\hat{\Theta})/ \hat{\Theta} $
bias	2.1617E+00	0.0038
u	-4.2100E-01	0.0042
$\sin(\theta)\mu_x$	-2.3743E+00	0.0027
$\mu_x\mu_z$	2.8746E-01	0.0043
$\omega_{tot}u$	-5.3506E-04	0.0059
R^2	0.939	

Regressor	$\hat{\Theta}$	$s(\hat{\Theta})/ \hat{\Theta} $
bias	-2.0383E-03	0.1776
p	-1.0710E-04	0.2156
u_p	4.3790E-06	0.0019
$\cos(\phi)\omega_{tot}^2$ $\omega_{tot} u_q ^2$	2.8384E-08	0.0633
$\omega_{tot} u_q ^2$	4.1427E-14	0.0571
$ u_q $	-3.6553E-07	0.0801
\mathbb{R}^2	0.955	

(c) F_y

Regressor	$\hat{\Theta}$	$s(\hat{\Theta})/ \hat{\Theta} $
bias	-1.6191E-02	0.0634
v	-1.1805E-01	0.0429
$\sin(\phi)\omega_{tot}$	1.5455E-02	0.0073
$\sin(\phi)\omega_{tot}^2$	-1.9112E-05	0.0128
$\omega_{tot}v$	-5.6904E-04	0.0202
\mathbb{R}^2	0.989	

(d) M_y

Regressor	$\hat{\Theta}$	$s(\hat{\Theta})/ \hat{\Theta} $
bias	4.2469E-02	0.0147
q	-8.8516E-04	0.0614
u_q	3.5308E-06	0.0053
\overline{w}	2.0493E-02	0.0153
w^2	1.8992E-03	0.0332
$\omega_{tot}w^3$	1.4971E-07	0.0685
R^2	0.766	

Regressor	$\hat{\Theta}$	$s(\hat{\Theta})/ \hat{\Theta} $
bias	3.1441E+00	0.0031
w	6.5460E-02	0.0650
$\frac{\omega_{tot}^2}{w^2}$	-1.9059E-05	0.0008
w^2	3.2176E-02	0.0145
$ q \mu_x $	6.5475E-02	0.0247
\mathbb{R}^2	0.979	

Table A.19: Aerodynamic models for damage case: 30BL at mean airspeed 0 ms^{-1}

Regressor	Θ	$s(\hat{\Theta})/ \hat{\Theta} $
bias	-4.8475E-02	0.0184
u	-4.7458E-01	0.0015
$\sin(\theta)\omega_{tot}$	-1.7530E-02	0.0029
$\sin(\theta)\omega_{tot}^2$	1.9271E-05	0.0054
$\omega_{tot}q$	-7.8074E-05	0.0115
\mathbb{R}^2	0.994	

Regressor	$\hat{\Theta}$	$s(\hat{\Theta})/ \hat{\Theta} $
bias	-1.1730E-02	0.0746
v	-3.2346E-01	0.0023
$\sin(\phi)\omega_{tot}$	1.5387E-02	0.0042
$\sin(\phi)\omega_{tot}^2$	-1.6087E-05	0.0082
$\omega_{tot}p$	6.2459E-05	0.0121
R^2	0.995	

(e) F_z

Regressor	$\hat{\Theta}$	$s(\hat{\Theta})/ \hat{\Theta} $
bias	3.8117E+00	0.0006
w	-1.6484E-01	0.0080
ω_{tot}^2	-2.0044E-05	0.0005
$\omega_{tot} w^2$	5.4455E-05	0.0176
$ u_p w$	-1.0484E-05	0.0336
\mathbb{R}^2	0.996	

(b) M_x

Regressor	$\hat{\Theta}$	$s(\hat{\Theta})/ \hat{\Theta} $
bias	-1.4662E-02	0.0045
p	-3.9905E-04	0.0600
u_p	1.1515E-06	0.0814
$\cos(\phi)v$	-9.6182E-03	0.0082
$\cos(\phi)vw$	-2.3083E-03	0.0237
$\cos(\phi)u_p$	3.7108E-06	0.0270
\mathbb{R}^2	0.963	

(d) M_y

Regressor	$\hat{\Theta}$	$s(\hat{\Theta})/ \hat{\Theta} $
bias	2.5354E-03	0.1274
q	-4.1992E-04	0.0536
u_q	3.5479E-06	0.0015
$\cos(\hat{\theta})\mu_x$	3.4595E-02	0.0122
$\cos(\theta)\omega_{tot}^2$	6.3261E-08	0.0271
$\cos(\theta)\mu_x\mu_z$	5.6141E-02	0.0418
R^2	0.976	

Regressor	$\hat{\Theta}$	$s(\hat{\Theta})/ \hat{\Theta} $
bias	-6.9523E-06	56.7323
r	-6.5440E-03	0.0214
u_r	-1.2961E-06	0.0183
$ r v ^{3}$	1.7014E-02	0.0634
$ u_q \mu_y $	-1.2580E-05	0.0722
$ u_q u_r$	3.1589E-11	0.1165
R^2	0.441	

Table A.20: Aerodynamic models for damage case: 30BL at mean airspeed 8 ms^{-1}

Regressor	$\hat{\Theta}$	$s(\hat{\Theta})/ \hat{\Theta} $
bias	9.2277E-01	0.0128
u	-2.2301E-01	0.0100
$\sin(\theta)\mu_x$	-2.5772E+00	0.0028
$\sin(\theta)\mu_x^2$	3.7797E-01	0.0039
$\omega_{tot}u$	-6.0129E-04	0.0054
R^2	0.919	

Regressor	$\hat{\Theta}$	$s(\hat{\Theta})/ \hat{\Theta} $
bias	-1.0710E-02	0.0104
p	-3.1234E-03	0.0222
u_p	4.9557E-06	0.0040
$u_{tot}u_p u_q $	-1.1493E-13	0.0260
$\cos(\phi)p r $	6.2112E-03	0.0357
$\sin(\phi)p^2$	-8.3420E-04	0.0599
R^2	0.942	

(c) F_y

Regressor	Θ	$s(\hat{\Theta})/ \hat{\Theta} $
bias	1.0219E-02	0.1658
v	-4.2830E-01	0.0049
$\sin(\phi)\omega_{tot}$	7.0132E-03	0.0035
v^2w	4.1382E-03	0.0430
pw^3	8.5866E-05	0.0505
\mathbb{R}^2	0.985	

(d) M_y

Regressor	Θ	$s(\hat{\Theta})/ \hat{\Theta} $
Regressor		3(0)/ 0
bias	4.6176E-02	0.0093
q	-6.8984E-04	0.0636
u_q	6.2517E-06	0.0169
μ_z	3.3163E-02	0.0111
$\sin(\theta)u_q$	-9.1991E-07	0.0253
$\omega_{tot}u_q$	-7.3741E-09	0.0343
\mathbb{R}^2	0.788	

Regressor	$\hat{\Theta}$	$s(\hat{\Theta})/ \hat{\Theta} $
bias	3.3414E+00	0.0035
w	1.1423E-02	0.2933
$w_{tot}^2 \ w^3$	-2.0058E-05	0.0008
w^3	-3.2214E-03	0.0126
$ u_q u ^3$	-6.4372E-08	0.0308
R^2	0.981	

Table A.21: Aerodynamic models for damage case: 30FL at mean airspeed 0 ms^{-1}

(a)	F_x
(a)	1 x

Regressor	Θ	$s(\hat{\Theta})/ \hat{\Theta} $
bias	-2.4303E-02	0.0382
u	-5.4479E-01	0.0014
$\sin(\theta)\omega_{tot}$	-1.8211E-02	0.0036
$\sin(\theta)\omega_{tot}^2$	2.0287E-05	0.0068
q	-3.0386E-02	0.0123
\mathbb{R}^2	0.993	

Regressor	$\hat{\Theta}$	$s(\hat{\Theta})/ \hat{\Theta} $
bias	-5.6862E-03	0.1207
v	-3.6736E-01	0.0016
$\sin(\phi)\omega_{tot}$	1.7813E-02	0.0026
$\sin(\phi)\omega_{tot}^2$	-2.0840E-05	0.0046
$\omega_{tot}p$	5.8162E-05	0.0102
\mathbb{R}^2	0.995	

(e) F_z

Regressor	$\hat{\Theta}$	$s(\hat{\Theta})/ \hat{\Theta} $
bias	3.5520E+00	0.0015
w	-2.2757E-01	0.0036
$\frac{\omega_{tot}^2}{w^2}$	-2.1968E-05	0.0020
w^2	2.1750E-02	0.0162
ω_{tot}	1.4707E-03	0.0221
\mathbb{R}^2	0.995	

(b) M_x

Regressor	$\hat{\Theta}$	$s(\hat{\Theta})/ \hat{\Theta} $
bias	-1.2058E-02	0.0044
p	-2.1916E-04	0.0862
u_p	7.1058E-06	0.0108
$\cos(\phi)v$	-7.4670E-03	0.0085
$\cos(\phi)vw$	-1.9074E-03	0.0240
$\omega_{tot}u_p$	-5.3596E-09	0.0319
\mathbb{R}^2	0.969	

(d) M_y

Regressor	$\hat{\Theta}$	$s(\hat{\Theta})/ \hat{\Theta} $
bias	-4.4822E-03	0.0126
q	-5.1702E-04	0.0404
u_q	-1.3599E-06	0.0537
$\cos(\theta)u$	9.6407E-03	0.0070
$\cos(\theta)\mu_x\mu_z$	6.5248E-02	0.0130
$\cos(\theta)u_q$	5.1964E-06	0.0150
R^2	0.963	

Regressor	$\hat{\Theta}$	$s(\hat{\Theta})/ \hat{\Theta} $
bias	3.0130E-03	0.0568
r	-3.7507E-03	0.0236
u_r	-2.1171E-06	0.0490
$\omega_{tot}u_r$	2.7906E-09	0.0893
p r	-5.1072E-03	0.0718
$\sin(\theta) v ^3$	-1.2981E-01	0.0724
R^2	0.551	

Table A.22: Aerodynamic models for damage case: 30FL at mean airspeed 8 ms^{-1}

Regressor	$\hat{\Theta}$	$s(\hat{\Theta})/ \hat{\Theta} $
bias	2.1589E+00	0.0056
u	-9.8980E-01	0.0028
$\sin(\theta)\mu_x$	-3.1104E+00	0.0022
$\sin(\theta)\mu_x^2$	7.0000E-01	0.0034
$\omega_{tot}\mu_x^2$	1.8715E-03	0.0048
R^2	0.934	

Regressor	$\hat{\Theta}$	$s(\hat{\Theta})/ \hat{\Theta} $
bias	-1.2786E-03	0.3103
p	9.0449E-04	0.1097
u_p	4.7056E-06	0.0013
$\cos(\phi)\omega_{tot}^2$	-6.0610E-08	0.0372
$ u_q u_r $	-3.0409E-11	0.0465
$p\mu_z$	1.4254E-03	0.0656
\mathbb{R}^2	0.981	

(c) F_y

Regressor	$\hat{\Theta}$	$s(\hat{\Theta})/ \hat{\Theta} $
bias	3.8994E-04	3.3558
v	-3.8799E-01	0.0034
$\sin(\phi)\omega_{tot}$	7.2710E-03	0.0031
$\sin(\phi)w^3$	2.3416E-03	0.0327
$\omega_{tot}p$	-2.1011E-05	0.0472
\mathbb{R}^2	0.987	

(d) M_y

$s(\hat{\Theta})/ \hat{\Theta} $
0.0582
3 0.0230
0.0024
0.0131
0.0096
0.0160

Regressor	$\hat{\Theta}$	$s(\hat{\Theta})/ \hat{\Theta} $
bias	2.8002E+00	0.0033
w	-1.3815E-01	0.0147
$\begin{array}{c} \omega_{tot}^2 \\ \omega_{tot} w^3 \end{array}$	-2.0607E-05	0.0010
$\omega_{tot}w^3$	-4.1055E-06	0.0154
$ q \mu_x $	7.8919E-02	0.0261
\mathbb{R}^2	0.979	